

NASA TECHNICAL  
MEMORANDUM



NASA TM X-3309

NASA TM X-3309

(NASA-TM-X-3309) EXPERIMENTAL AERODYNAMIC  
CHARACTERISTICS FOR SLENDER BODIES WITH THIN  
WINGS AT ANGLES OF ATTACK FROM 0 DEG TO 58  
DEG AND MACH NUMBERS FROM 0.6 TO 2.0 (NASA)  
127 p HC \$6.00

N76-15080

Unclass

CSCL 01A B1/C2 08606



EXPERIMENTAL AERODYNAMIC CHARACTERISTICS  
FOR SLENDER BODIES WITH THIN WINGS  
AT ANGLES OF ATTACK FROM 0° TO 58°  
AND MACH NUMBERS FROM 0.6 TO 2.0

*Leland H. Jorgensen and Michael H. Howell*

*Ames Research Center*

*Moffett Field, Calif. 94035*



NATIONAL AERONAUTICS AND SPACE ADMINISTRATION • WASHINGTON, D. C. • JANUARY 1976

1. Report No. NASA TM X-3309	2. Government Accession No.	3. Recipient's Catalog No.	
4. Title and Subtitle EXPERIMENTAL AERODYNAMIC CHARACTERISTICS FOR SLENDER BODIES WITH THIN WINGS AT ANGLES OF ATTACK FROM 0° TO 58° AND MACH NUMBERS FROM 0.6 TO 2.0		5. Report Date January 1976	
		6. Performing Organization Code	
7. Author(s) Leland H. Jorgensen and Michael H. Howell		8. Performing Organization Report No. A-6150	
9. Performing Organization Name and Address Ames Research Center and ARO Inc. Moffett Field, Calif. 94035		10. Work Unit No. 505-06-81	
		11. Contract or Grant No.	
12. Sponsoring Agency Name and Address National Aeronautics and Space Administration Washington, D.C. 20546		13. Type of Report and Period Covered Technical Memorandum	
		14. Sponsoring Agency Code	
15. Supplementary Notes			
16. Abstract  <p>An experimental investigation was conducted in the Ames 6-by-6-Foot Wind Tunnel to measure the static aerodynamic characteristics for bodies of circular and elliptic cross section with various thin flat-plate wings. Three wings had aspect ratios of 4 and taper ratios of about 0.025, and 0.5. Two additional wings, which had taper ratios near 0.25 and aspect ratios of about 3 and 5, were also tested in combination with the bodies. All wings had about the same planform area. The elliptic body, with an <math>a/b = 2</math> cross section, had the same length and axial distribution of cross sectional area as the circular body. The circular body had a cylindrical aftersection of fineness ratio 7, and it was tested with the wings and tangent ogive noses that had fineness ratios of 2.5, 3.0, 3.5, and 5.0. In addition, an ogive nose with a rounded tip and an ogive nose with two different nose stake arrangements were used.</p> <p>Eighteen configuration combinations were tested at Mach numbers of 0.6, 0.9, 1.2, 1.5, and 2.0 at angles of attack from 0° to 58°. The Reynolds numbers, based on body base diameter, were about <math>4.3 \times 10^5</math> at the subsonic Mach numbers and about <math>3.8 \times 10^5</math> at the supersonic Mach numbers.</p> <p>The data demonstrate that taper ratio and aspect ratio had only small effect on the aerodynamic characteristics, especially at the higher angles of attack. Undesirable side forces and yawing moments, which developed at angles of attack greater than about 25°, were generally no greater than those for the bodies tested alone. As for the bodies alone, the side forces and yawing moments increased as the nose fineness ratio increased and/or as the subsonic Mach number decreased.</p>			
17. Key Words (Suggested by Author(s))  High angle of attack aerodynamics Body-wing aerodynamics		18. Distribution Statement  Unlimited  STAR Category -- 02	
19. Security Classif. (of this report)  Unclassified	20. Security Classif. (of this page)  Unclassified	21. No. of Pages  126	22. Price*  \$5.75

## NOMENCLATURE

All forces and moments except  $C_L$  and  $C_D$  are referred to the body axis coordinate system.

$A_T$	reference area = body base area = 34.26 cm <sup>2</sup> (5.31 in. <sup>2</sup> )
$A_w$	exposed wing planform area (2 panels)
$R$	aspect ratio for wing extended into center of body $B_1$
$R_e$	aspect ratio for two exposed wing panels if they are removed from the body and joined together
$a, b$	semimajor and semiminor axes of elliptic cross section
$C_A$	axial-force coefficient, $C_{A_{bal}} - C_{A_{base}}$
$C_{A_{bal}}$	balance axial-force coefficient, $\frac{F_A}{qA_T}$
$C_{A_{base}}$	base-pressure force coefficient, $\frac{(p - p_{base})}{q}$
$C_D$	drag coefficient, $\frac{\text{drag}}{qA_T}$
$C_L$	lift coefficient, $\frac{\text{lift}}{qA_T}$
$C_m$	pitching-moment coefficient about balance center, 4d from body base, $\frac{\text{pitching moment}}{q A_T X}$
$C_N$	normal-force coefficient, $\frac{F_N}{qA_T}$
$C_n$	yawing-moment coefficient about balance center, 4d from body base, $\frac{\text{yawing moment}}{qA_T X}$
$C_Y$	side-force coefficient, $\frac{F_Y}{qA_T}$
$c_r, c_t$	wing root and tip chords
$d$	body base diameter = 6.60 cm (2.60 in.)
$F_A, F_N, F_Y$	axial, normal, and side force, respectively
$L/D$	lift-to-drag ratio
$\ell$	body length
$\ell_N$	nose length

<b>M</b>	free-stream Mach number
<b>p</b>	free-stream static pressure
<b>P<sub>base</sub></b>	base pressure
<b>q</b>	free-stream dynamic pressure
<b>Re</b>	Reynolds number based on d
<b>r</b>	body base radius = 3.30 cm (1.30 in.)
<b>s</b>	wing semispan from body centerline
<b>X</b>	reference length = d = 6.60 cm (2.60 in.)
$\frac{x_{acN}}{d}$	distance (in diameters) from body base to aerodynamic force center in normal-force plane, $\left( \frac{C_m}{C_N} + \frac{x_m}{X} \right)$
<b>x<sub>m</sub></b>	distance from body base to balance moment reference = 4d = 26.42 cm (10.40 in.)
<b>α</b>	angle of attack, deg
<b>ε</b>	wing semiapex angle, deg
<b>φ</b>	angle of bank about body longitudinal axis, deg

#### Configuration Code

Because the data are computer plotted, both the conventional symbol and the plot symbol are given.

Symbol	Plot Symbol	Component
<b>B<sub>1</sub></b>	<b>B1</b>	basic circular body (tangent ogive nose of fineness ratio 3 with cylinder aftersection of fineness ratio 7)
<b>B<sub>2</sub></b>	<b>B2</b>	body with elliptic cross section of constant $\frac{a}{b} = 2$
<b>φ=0°</b>	<b>PHI=0</b>	body banked 0° about longitudinal axis (see fig. 1(a))
<b>φ=90°</b>	<b>PHI=90</b>	body banked 90° about longitudinal axis (see fig. 1(a))

Symbol	Plot Symbol	Component	Fineness Ratio
$C_1$	C1	circular cylinder	7
$N_1$	N1	tangent ogive nose	3
$N_2$	N2	tangent ogive nose	3.5
$N_3$	N3	tangent ogive nose	5
$N_4$	N4	tangent ogive nose with rounded tip	3
$N_5$	N5	tangent ogive nose with tip strakes	3
$N_6$	N6	tangent ogive nose with side strakes	3
$N_7$	N7	tangent ogive nose	2.5
$W_1$	W1	wing of $AR \approx 4$ , $c_t/c_T = 0$	
$W_2$	W2	wing of $AR \approx 4$ , $c_t/c_T = 0.276$	
$W_3$	W3	wing of $AR \approx 4$ , $c_t/c_T = 0.533$	
$W_4$	W4	wing of $AR \approx 5$ , $c_t/c_T = 0.273$	
$W_5$	W5	wing of $AR \approx 3$ , $c_t/c_T = 0.280$	
G	G	transition strip around nose $N_1$ (0.249-cm-diameter glass spheres, 0.159-cm wide, and 3.81 cm aft of nose apex)	

# **EXPERIMENTAL AERODYNAMIC CHARACTERISTICS FOR SLENDER BODIES**

**WITH THIN WINGS AT ANGLES OF ATTACK FROM 0° TO 58°**

**AND MACH NUMBERS FROM 0.6 TO 2.0**

**Leland H. Jorgensen and Michael H. Howell\***

**Ames Research Center**

## **SUMMARY**

An experimental investigation was conducted in the Ames 6-by-6-Foot Wind Tunnel to measure the static aerodynamic characteristics for bodies of circular and elliptic cross section with various thin flat-plate wings. Three wings had aspect ratios of 4 and taper ratios of about 0, 0.25, and 0.5. Two additional wings, which had taper ratios near 0.25 and aspect ratios of about 3 and 5, were also tested in combination with the bodies. All wings had about the same planform area. The elliptic body, with an  $a/b = 2$  cross section, had the same length and axial distribution of cross sectional area as the circular body. The circular body had a cylindrical aftersection of fineness ratio 7, and it was tested with the wings and tangent ogive noses that had fineness ratios of 2.5, 3.0, 3.5, and 5.0. In addition, an ogive nose with a rounded tip and an ogive nose with two different nose strake arrangements were used.

Eighteen configuration combinations were tested at Mach numbers of 0.6, 0.9, 1.2, 1.5, and 2.0 at angles of attack from 0° to 58°. The Reynolds numbers, based on body base diameter, were about  $4.3 \times 10^5$  at the subsonic Mach numbers and about  $3.8 \times 10^5$  at the supersonic Mach numbers.

The data demonstrate that taper ratio and aspect ratio had only small effect on the aerodynamic characteristics, especially at the higher angles of attack. Undesirable side forces and yawing moments, which developed at angles of attack greater than about 25°, were generally no greater than those for the bodies tested alone. As for the bodies alone, the side forces and yawing moments increased as the nose fineness ratio increased and/or as the subsonic Mach number decreased.

## **INTRODUCTION**

In the last several years high angle-of-attack aerodynamics has increased in importance because of the demand for greater maneuverability of missiles and aircraft (both manned and remotely piloted). Some recent introductory investigations in this field are reported in references 1 through 11. Most of the research reported in these references has been concerned with bodies and has been directed more toward missile applications than aircraft. The relatively small data base that existed several years ago for bodies alone and with strakes has been considerably enlarged, and work

---

\*Project Engineer, ARO, Inc., Moffett Field, California 94035.



in this area seems to be continuing at a reasonable rate. However, there is still great need to enlarge the relatively small data base for bodies in combination with wings or tails, or both, at subsonic, transonic, and supersonic Mach numbers. This data base, of course, is more applicable to aircraft than missiles.

To help enlarge this data base for basic bodies with wings, an investigation was conducted to measure the force and moment characteristics for bodies of circular and elliptic cross section in combination with thin wings of taper ratios of 0 to 0.5 and aspect ratios of 3 to 5. The bodies used are the same as those studied in references 8 and 10, and there are variations in nose fineness ratio, bluntness, and nose strake arrangement. All models were tested in the Ames 6-by-6-Foot Wind Tunnel at Mach numbers of 0.6, 0.9, 1.2, 1.5, and 2.0 and angles of attack from  $0^\circ$  to  $58^\circ$ .

The purpose of this report is to present and discuss briefly the basic data that show the effects on the aerodynamic characteristics of wing taper ratio, wing aspect ratio, nose fineness ratio, nose bluntness, and nose strake arrangement.

## TEST FACILITY

The experimental investigation was conducted in the Ames 6-by-6-Foot Wind Tunnel – a variable pressure, continuous flow, closed-return type facility. The nozzle ahead of the test section consists of an asymmetric sliding block that permits the Mach number to be continuously varied from 0.6 to 2.3. The test section has a perforated floor and ceiling so that boundary-layer flow can be removed for transonic testing.

## MODELS AND BALANCE

Figure 1 shows the model components that were tested in various model combinations. These components include bodies, noses, and wings.

The basic circular body ( $B_1$ ) depicted in figure 1(a) consisted of a circular-arc tangent ogive of fineness ratio 3 followed by a cylindrical aftersection of fineness ratio 7. Body  $B_2$  (fig. 1(a)) had an elliptic cross section of  $a/b = 2$  and the same length and axial distribution of cross-sectional area as  $B_1$ . Hence, the fineness ratio of  $\ell/d = 10$  for  $B_1$  was also the equivalent fineness ratio for  $B_2$ . These bodies were previously tested, and the results are reported in reference 10. The basic circular aftersection of  $B_1$  (designated as  $C_1$ ) was also tested (ref. 8) with ogive noses of fineness ratio 2.5 to 5 (noses  $N_7$ ,  $N_1$ ,  $N_2$ , and  $N_3$  in fig. 1(b)). The circular aftersection  $C_1$  was also tested (ref. 8) with a blunted nose ( $N_4$ ) and noses with strakes ( $N_5$  and  $N_6$ ).

For the present test the bodies and noses in figures 1(a) and 1(b) were combined with five flat-plate wings (figs. 1(c)-1(e)) that formed two families of wings. One family –  $W_1$ ,  $W_2$ , and  $W_3$  – had an aspect ratio of about 4 and taper ratios ( $c_t/c_r$ ) of 0, 0.276, and 0.533 (fig. 1(c)). The other family –  $W_4$ ,  $W_2$ , and  $W_5$  – had aspect ratios of about 5, 4, and 3, respectively, and the taper ratios were all about 0.28 (fig. 1(d) and 1(e)).

All of the wings were designed to have the same planform area ( $16 d^2$ ) if the wings extended into the body  $B_1$  to the axial centerline. Based on the phantom wing chord at the body centerline, the taper ratios for wings  $W_1$ ,  $W_2$ , and  $W_3$  were 0, 0.25, and 0.50, respectively. They were also 0.25 for  $W_4$  and  $W_5$ . Pertinent planform dimensions of the exposed parts of the wings are given in table 1.

TABLE 1. – PLANFORM DIMENSIONS OF WINGS

Wing	$AR$	$AR_e$	$\epsilon, \text{deg}$	$(s-r)/d$	$c_r/d$	$c_t/d$	$c_t/c_r$	$A_w/d^2$	$A_w/A_T$
$W_1$	4	4	45.00	3.5	3.5	0	0	12.250	15.598
$W_2$	4	3.784	59.03	3.5	2.9	.800	.276	12.950	16.488
$W_3$	4	3.653	71.57	3.5	2.5	1.333	.533	13.412	17.076
$W_4$	5	4.761	64.36	3.972	2.622	.715	.273	13.254	16.876
$W_5$	3	2.810	51.33	2.964	3.295	.924	.280	12.506	15.924

where

$AR$  aspect ratio for wing extended into center of body  $B_1$

$AR_e$  aspect ratio for two exposed wing panels joined together

$d$  diameter of body  $B_1$

$A_w$  exposed wing planform area (2 panels)

$A_T$  reference area = body base area

Figure 2(a) shows the planform views of the 18 configurations that were tested in this study. All of these configurations are identified by the codes shown in figure 1: these codes are used throughout the report.

All model parts were constructed of stainless steel, and all models were sting-mounted (fig. 2(b)) through the base on a six-component, strain-gage "Task" balance. The balance force center was located inside each body at a position 4 base diameters forward of the base.

## TESTS AND DATA REDUCTION

All model configurations shown in figure 2(a) were tested at angles of attack from  $0^\circ$  to about  $58^\circ$  on two model-support setups. One setup (fig. 2(b)) was used to test the models at angles of attack from  $0^\circ$  to about  $27^\circ$ , and the other (similar to fig. 2(b) and shown in ref. 8) was used for angles of attack from  $27^\circ$  to  $58^\circ$ . The models were tested at Mach numbers of 0.6, 0.9, 1.2, 1.5, and 2.0. The Reynolds numbers, based on body diameter  $d$ , were about  $4.3 \times 10^5$  at the subsonic Mach numbers and about  $3.8 \times 10^5$  at the supersonic Mach numbers.



Several runs were made (ref. 8) with a boundary-layer transition strip around the noses of bodies  $N_1 C_1$  and  $N_3 C_1$ . This strip consisted of 0.249-cm-diameter glass spheres, 0.159-cm wide and located 3.81 cm aft of the nose apex. As reported in reference 8, this strip had little or no effect on the aerodynamic characteristics.

Six-component aerodynamic force and moment data were measured at each test condition, and all data were reduced to coefficient form and referred to the body axis coordinate system. The average base pressure from four base pressure tubes (at the sides, top, and bottom of the base) was used to compute the base drag. The base drag was subtracted from the total axial-force balance measurements, so that the data presented are for forces ahead of the body base. Rolling-moment coefficients were generally small and are omitted. Normal-force aerodynamic centers were computed from the normal-force and pitching-moment coefficients and are presented in lieu of the pitching-moment coefficients.

Lift coefficients and values of  $L/D$ , referred to the wind axes, were also computed and are presented. They were computed from the expressions:

$$C_L = C_N \cos \alpha - C_A \sin \alpha \quad (1)$$

$$C_D = C_N \sin \alpha + C_A \cos \alpha \quad (2)$$

and

$$\frac{L}{D} = \frac{C_L}{C_D} \quad (3)$$

The reference area  $A_T$  for all coefficients is the body base area (34.26 cm<sup>2</sup>), and the reference length  $X$  for all moment coefficients is the body base diameter (6.60 cm). The coefficients, of course, can be easily recomputed based on wing area and an appropriate wing chord length, such as the root chord or mean aerodynamic chord. For example, the force coefficients based on exposed wing area can be obtained by dividing the presented values by the appropriate values of  $A_w/A_T$  tabulated in the previous section.

## RESULTS AND DISCUSSION

Experimental results (figs. 3–29) show the effects on the aerodynamic characteristics of wing taper ratio, wing aspect ratio, nose fineness ratio, nose rounding, and nose strake arrangement. Each effect is discussed briefly with the aid of plots of  $C_N$ ,  $x_{acN}/d$ ,  $C_Y$ ,  $C_Y/C_N$ ,  $C_n$ ,  $C_L$ , and  $L/D$  versus  $\alpha$  for  $\alpha = 0^\circ$  to  $60^\circ$ . Plots of  $C_A$  versus  $\alpha$  are also presented but are not discussed. Because the models were sting-supported from the rear, it is likely that the  $C_A$  data include effects of support interference. Any support effects are also included in the  $C_L$  and  $L/D$  data (obtained from  $C_N$  and  $C_A$  by eqs. (1)–(3)) but to a much smaller extent. Any effects of tunnel-blockage interference are unknown and are ignored.

### Effect of Wing Taper Ratio

Data that show the effect of wing taper ratio on the aerodynamic characteristics for the winged circular body ( $B_1$  with  $W_1$ ,  $W_2$ , and  $W_3$ ) are presented in figures 3 through 7. Similar data for the winged elliptic body ( $B_2$  with  $W_1$ ,  $W_2$ , and  $W_3$ ) are presented in figures 8 through 12. Body-alone data (from refs. 8 and 10) for  $B_1 = N_1$ ,  $C_1$  and  $B_2$  are shown for comparison.

For the change in taper ratio from 0 to about 0.5 ( $W_1$  to  $W_3$ ), there are generally only small effects on the aerodynamic characteristics. This is especially true for  $C_N$  and  $C_L$  at the subsonic Mach numbers ( $M = 0.6$  and  $0.9$ ) and high angles of attack (greater than about  $\alpha = 15^\circ$ ). At the supersonic Mach numbers and high angles of attack, there is generally more variation in the  $C_N$  and  $C_L$  data, the coefficients being highest for the wing with the highest taper ratio ( $W_3$ ,  $c_t/c_r = 0.5$ ). Wing  $W_3$ , however, has greater exposed wing area than the wing with no taper ratio ( $W_1$ ). For example,  $A_w/A_T = 17.076$  for  $W_3$  as compared with  $A_w/A_T = 15.598$  for  $W_1$ . If the  $C_N$  and  $C_L$  data were based on  $A_w$  instead of  $A_T$ , the differences at high  $\alpha$  would be much less. Throughout the Mach number range, most the the variations between the configurations in  $C_N$  and  $C_L$  at low angles of attack probably can be attributed to flow separation effects from the wings.

It is interesting to note that the side-force coefficients ( $C_Y$ ) for the winged bodies are generally no greater and sometimes smaller than for the bodies alone.<sup>1</sup> As discussed previously (i.e., refs. 8 and 10), the undesirable side-force and yawing-moment coefficients that develop for the bodies alone at subsonic Mach numbers decrease with increase in subsonic Mach number and disappear with increase in Mach number into the supersonic flow regime. The same finding can be observed for the bodies with wings. However, for the winged bodies the relative influence of  $C_Y$  to  $C_N$  is much smaller. In fact, the ratio ( $C_Y/C_N$ ) appears to be negligible for the winged circular and elliptic bodies throughout the Mach number and angle of attack ranges studied.

### Effect of Wing Aspect Ratio

Data are presented in figures 13 through 17 that show the effect of wing aspect ratio on the aerodynamic characteristics for the winged circular body ( $B_1$  with  $W_5$ ,  $W_2$ , and  $W_4$  of  $AR = 3$ ,  $4$ , and  $5$ , respectively). Similar data for the winged elliptic body ( $B_2$  with  $W_5$ ,  $W_2$ , and  $W_4$ ) are presented in figures 18 through 22. Body-alone data (from refs. 8 and 10) are also shown for comparison.

As for the case of taper ratio, there are no large effects of aspect ratio on the aerodynamic characteristics, especially the longitudinal characteristics. The undesirable side forces and yawing moments, which appear at the high angles of attack, are no larger and sometimes smaller than those shown for the bodies alone.

---

<sup>1</sup>The signs of the side-force coefficients are sometimes different from run to run and from test of body alone to body with wing. It is believed that the signs result from the random asymmetric flow separation and vortex flow from the nose (observed from oil-flow tests).

### Effect of Nose Fineness Ratio

In figures 23 through 27, data are presented that show the effect on the aerodynamic characteristics of changing the nose fineness ratio from  $\ell_n/d = 2.5$  ( $N_7$ ) to  $\ell_n/d = 5$  ( $N_3$ ) for the circular cylinder ( $C_1$ ) with  $W_2$  (aspect ratio 4).

As might be expected, there is little or no effect of nose fineness ratio on the longitudinal characteristics. However, there is a strong effect of nose fineness ratio on the characteristics of  $C_Y$  and  $C_n$  versus  $\alpha$  for the winged body at  $\alpha$  greater than about  $25^\circ$  and  $M = 0.6$  and  $0.9$ . For example, in figures 23 and 24 it can be seen that the largest values of  $C_Y$  and  $C_n$  develop with the noses that have fineness ratios of 3.5 ( $N_2$ ) and 5 ( $N_3$ ). These effects are similar to those reported in reference 8 for the circular body alone but with the same noses. It thus can be concluded that the undesirable side-force and yawing-moment characteristics originate with, or are caused by, the body nose, and high fineness-ratio noses are the least desirable.

### Effects of Nose Rounding and Strakes

Data are presented in figures 28 and 29 that show the effects of nose rounding and strakes on wing-body aerodynamic characteristics for  $M = 0.6$  and  $2.0$ . Results are compared for the circular cylinder  $C_1$  and wing  $W_2$  with the basic nose  $N_1$  (fineness-ratio 3), the rounded nose  $N_4$ , the nose with tip strakes  $N_5$ , and the nose with strakes extending over its length  $N_6$ .

There are no significant effects from either nose rounding or strakes on any of the characteristics shown in figures 28 and 29 (compare results for  $N_4 C_1 W_2$  with those for  $N_1 C_1 W_2$ ). However, all of the configurations compared in figures 28 and 29 have fineness ratios of about 3 ( $N_6$  is slightly greater than 3). A different conclusion concerning the effect of bluntness is obtained if the results for the configuration ( $N_4 C_1 W_2$ ) with the blunt nose are compared with those (figs. 23 and 24) for the configuration ( $N_2 C_1 W_2$ ) with the sharp fineness-ratio 3.5 nose. As previously discussed, undesirable side forces and yawing moments appeared with  $N_2 C_1 W_2$  at  $M = 0.6$  and  $0.9$  (see figs. 23 and 24). However, with the nose apex of  $N_2 C_1 W_2$  blunted to give a fineness ratio of 3 (configuration  $N_4 C_1 W_2$ ), the side forces and yawing moments essentially disappeared.

There is a small increase in  $C_N$  and  $C_L$  at high  $\alpha$  and  $M = 0.6$  resulting from the use of  $N_6$ , the nose with the side strakes extending over the nose length (see fig. 28). This increase in  $C_N$  and  $C_L$  disappears at supersonic speeds (see fig. 29 for  $M = 2.0$ ).

### CONCLUSIONS

1. Generally, changing the taper ratio from 0 to 0.5 had only small effects on the aerodynamic characteristics.
2. As was true for taper ratio, changing the aspect ratio from 3 to 5 resulted in no large effects on the aerodynamic characteristics.

3. Undesirable side forces and yawing moments for the winged bodies were generally no greater and sometimes smaller than for the bodies alone. As for the bodies alone, the side forces and yawing moments developed at subsonic Mach number for angles of attack above about  $25^\circ$ . Also, as for the bodies alone, the side forces and yawing moments increased with increase in nose fineness ratio. Fineness ratios greater than 3 produced the largest side forces.

4. Nose-tip rounding of a fineness ratio 3.5 ogive nose reduced the undesirable side forces and yawing moments, but nose strakes on a fineness-ratio 3 nose produced little change in the characteristics. Strakes were not tested on the higher fineness ratio noses that produced large side forces.

Ames Research Center

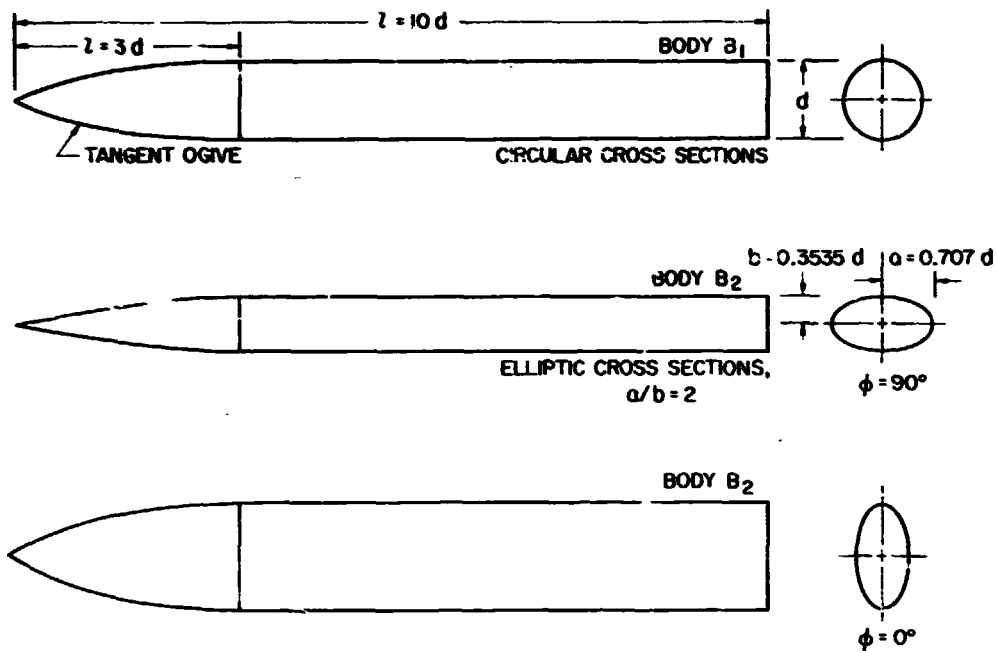
National Aeronautics and Space Administration

Moffett Field, Calif. 94035, June 20, 1975

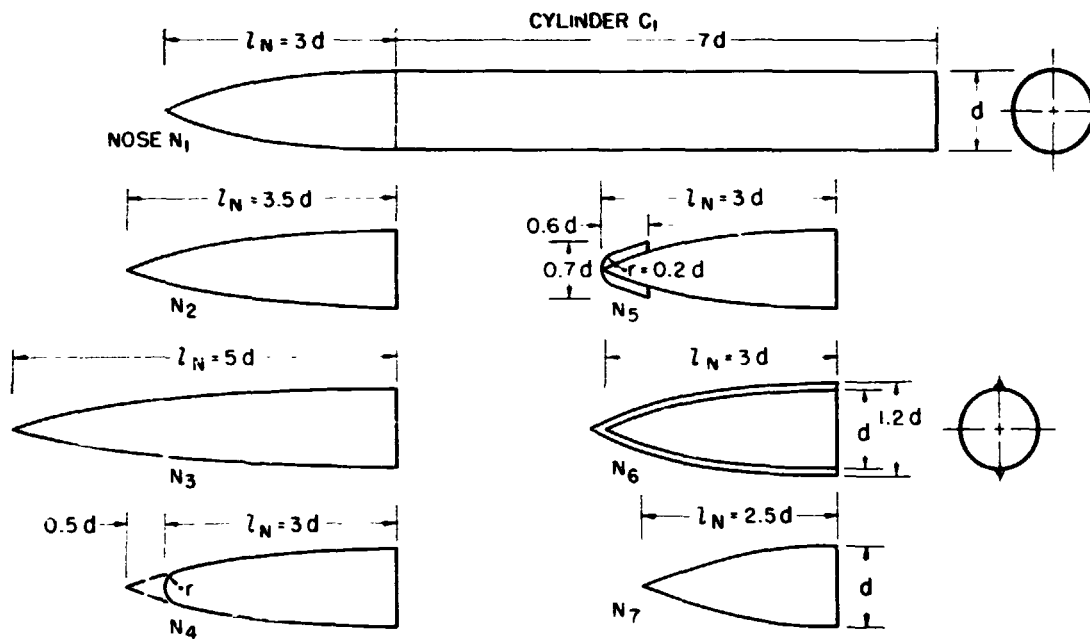
## REFERENCES

1. Pick, George S.: Side Forces on Ogive-Cylinder Bodies at High Angles of Attack in Transonic Flow. *J. Spacecraft and Rockets*, vol. 9 no. 6, pp. 389-390, June 1972.
2. Clark, William H.; Peoples, John R.; and Briggs, M. Michael: Occurrence and Inhibition of Large Yawing Moments During High Incidence Flight of Slender Missile Configurations. *AIAA Paper 72-968*, Sept. 1972.
3. Coe, Paul L., Jr.; Chambers, Joseph R.; and Letko, William: Asymmetric Lateral-Directional Characteristics of Pointed Bodies of Revolution at High Angles of Attack. *NASA TN D-7095*, 1972.
4. Jorgensen, Leland H.: Prediction of Static Aerodynamic Characteristics for Space-Shuttle-Like and Other Bodies at Angles of Attack From  $0^\circ$  to  $180^\circ$ . *NASA TN D-6996*, 1973.
5. Jorgensen, Leland H.: Estimation of Aerodynamics for Slender Bodies Alone and With Lifting Surfaces at  $\alpha$ 's From  $0^\circ$  to  $90^\circ$ . *AIAA Journal*, vol. 11, no. 3, pp. 409-412, March 1973.
6. Jorgensen, Leland H.: A Method for Estimating Static Aerodynamic Characteristics for Slender Bodies of Circular and Noncircular Cross Section Alone and With Lifting Surfaces at Angles of Attack from  $0^\circ$  to  $90^\circ$ . *NASA TN D-7228*, 1973.
7. Fleeman, E. L.; and Nelson, R. C.: Aerodynamic Forces and Moments on a Slender Body with a Jet Plume for Angles of Attack up to 180 Degrees. *AIAA Paper 74-110*, Jan. 1974.
8. Jorgensen, Leland H.; and Nelson, Edgar R.: Experimental Aerodynamic Characteristics for a Cylindrical Body of Revolution With Various Noses at Angles of Attack From  $0^\circ$  to  $58^\circ$  and Mach Numbers From 0.6 to 2.0. *NASA TM X-3128*, 1974.
9. Keener, Earl R.; and Chapman, Gary T.: Onset of Aerodynamic Side Forces at Zero Sideslip on Symmetric Forebodies at High Angles of Attack. *AIAA Paper 74-770*, Aug. 1974.
10. Jorgensen, Leland H.; and Nelson, Edgar R.: Experimental Aerodynamic Characteristics for Bodies of Elliptic Cross Section at Angles of Attack From  $0^\circ$  to  $58^\circ$  and Mach Numbers From 0.6 to 2.0. *NASA TM X-3129*, 1975.
11. Jorgensen, Leland H.; and Nelson, Edgar R.: Experimental Aerodynamic Characteristics for a Cylindrical Body of Revolution With Side Strakes and Various Noses at Angles of Attack From  $0^\circ$  to  $58^\circ$  and Mach Numbers From 0.6 to 2.0. *NASA TM X-3130*, 1975.

# PLANFORM AND END VIEWS OF BODIES

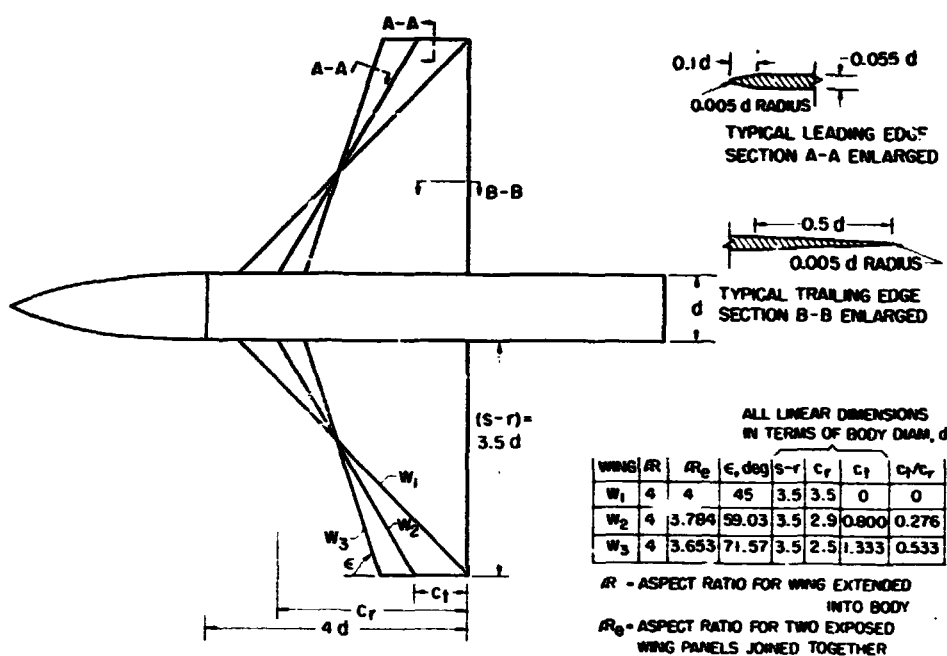


(a) Basic bodies of circular and elliptic cross section.



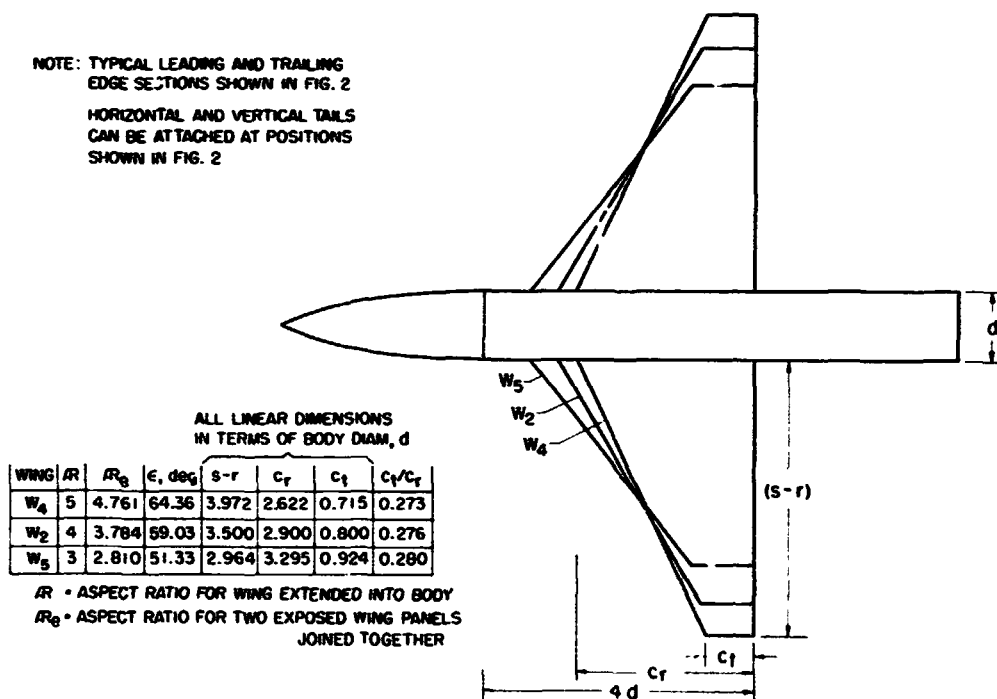
(b) Additional noses for modification of body  $B_1 = N_1 C_1$ .

Figure 1.— Model components;  $d = 5.6$  cm (2.60 in.).



(c) Body B<sub>1</sub> with aspect-ratio 4 wings of various taper ratios.

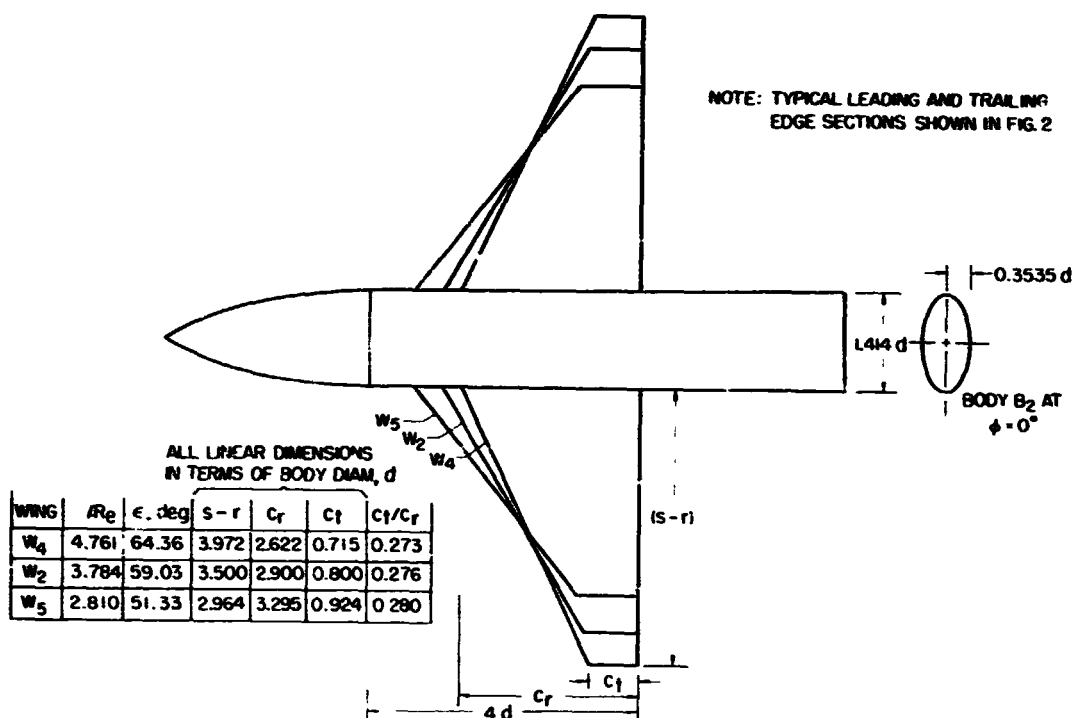
NOTE: TYPICAL LEADING AND TRAILING  
EDGE SECTIONS SHOWN IN FIG. 2  
HORIZONTAL AND VERTICAL TAILS  
CAN BE ATTACHED AT POSITIONS  
SHOWN IN FIG. 2



(d) Body B<sub>1</sub> with wings of aspect ratio 3, 4, and 5.

Figure 1.- Continued.

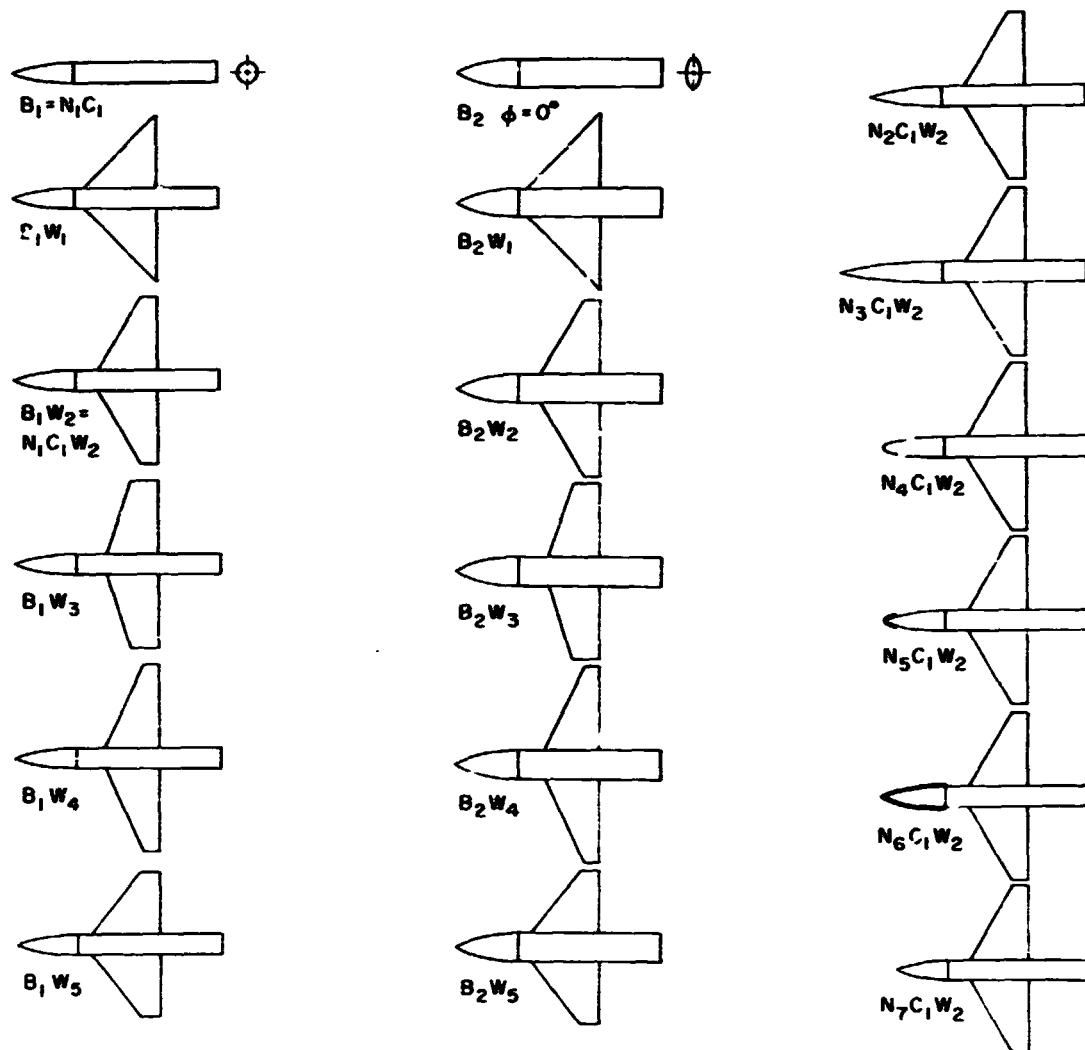




(e) Body  $B_2$  with wings  $W_2$ ,  $W_4$ , and  $W_5$ .

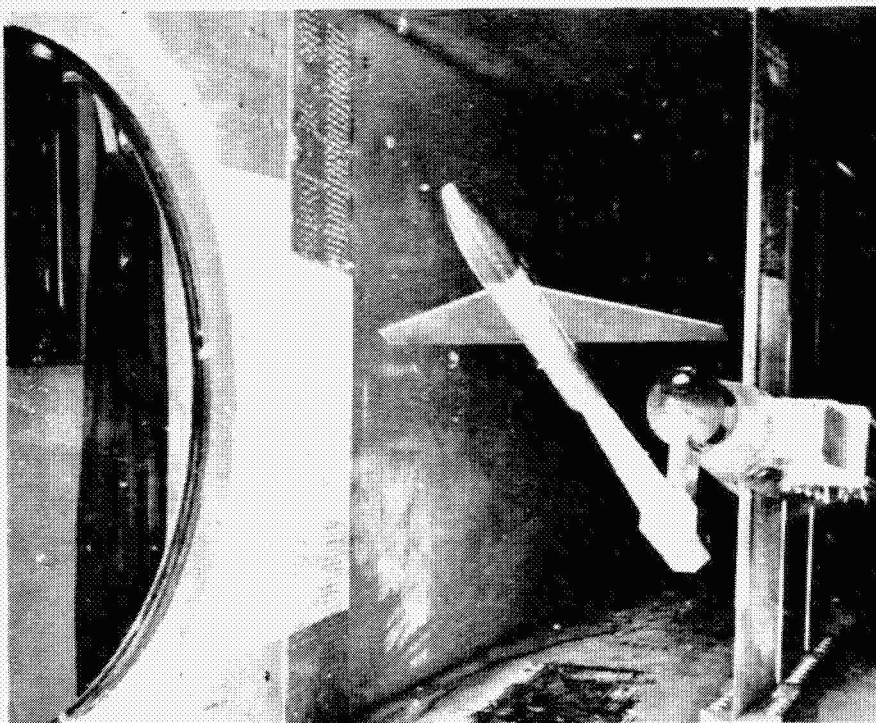
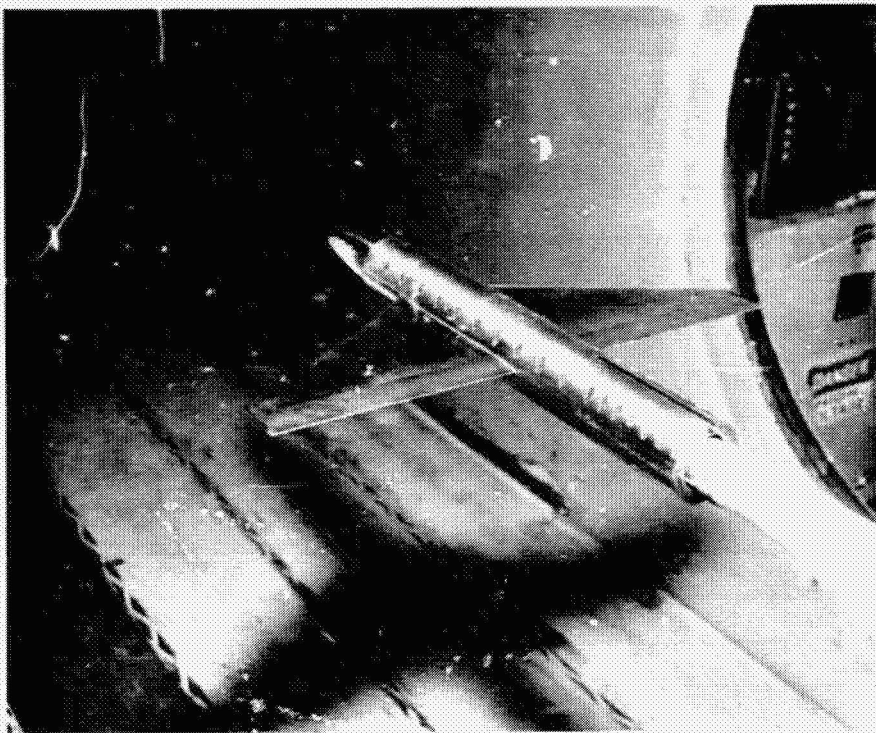
Figure 1.- Concluded.

REPRODUCIBILITY OF THE  
ORIGINAL PAGE IS POOR



(a) Planform views of configurations tested.

Figure 2.— Planform views of configurations tested and typical model-support setup in the Ames 6-by-6-Foot Wind Tunnel.



(b) Typical model-support setup in the Ames 6-by-6-Foot Wind Tunnel.

Figure 2. — Concluded.

REPRODUCIBILITY OF THE  
ORIGINAL PAGE IS POOR

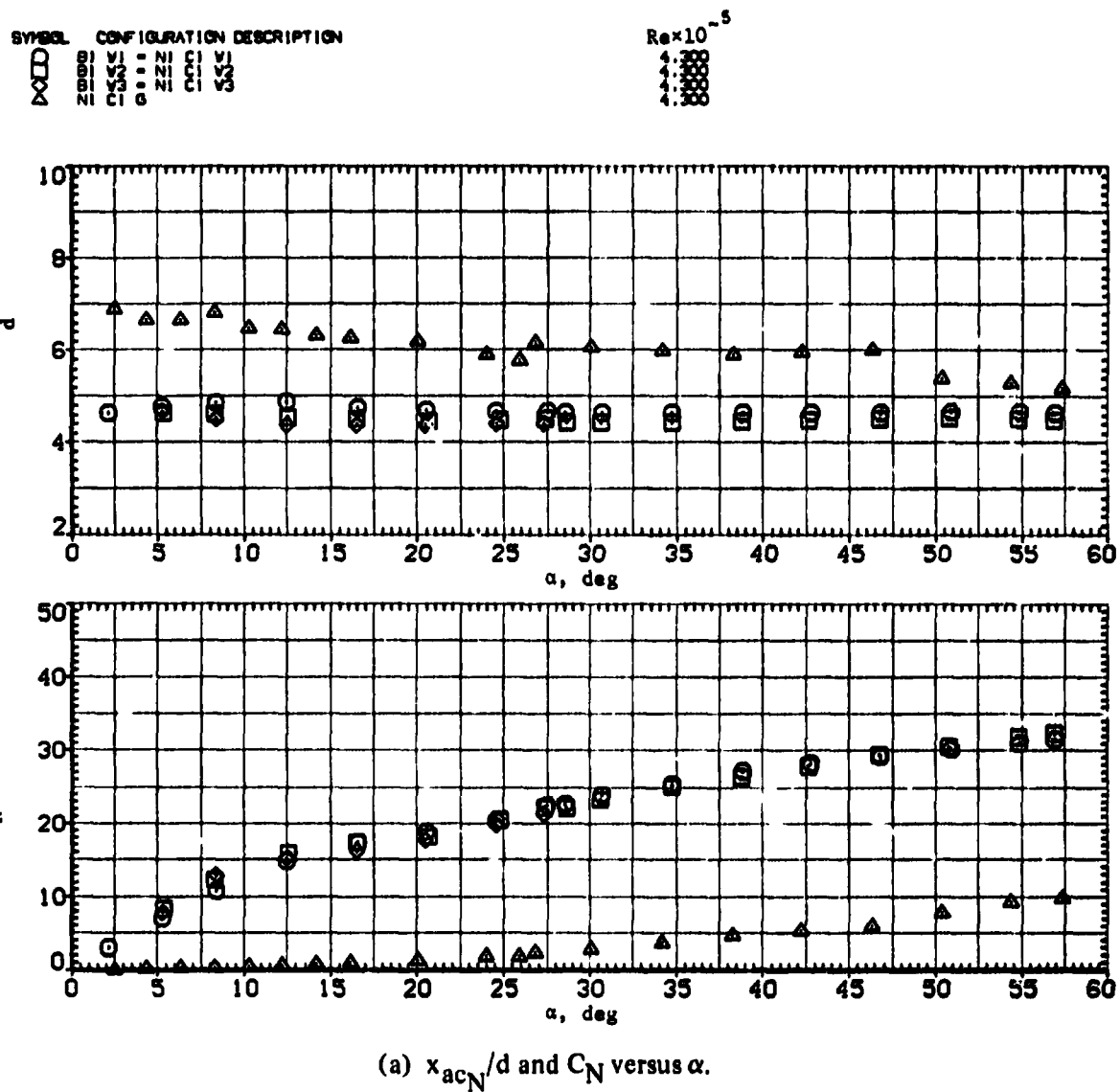


**Figure 3.— Effect of wing taper ratio with circular body;  $M = 0.6$ .**

SYMBOL	CONFIGURATION DESCRIPTION
$\square$	NI C1
$\circ$	NI C1
$\triangle$	NI C1
$\times$	NI C1
$\diamond$	NI C1
$\nabla$	NI C1
$\square$	NI C1
$\circ$	NI C1
$\triangle$	NI C1
$\times$	NI C1
$\diamond$	NI C1
$\nabla$	NI C1

$Re \times 10^{-5}$

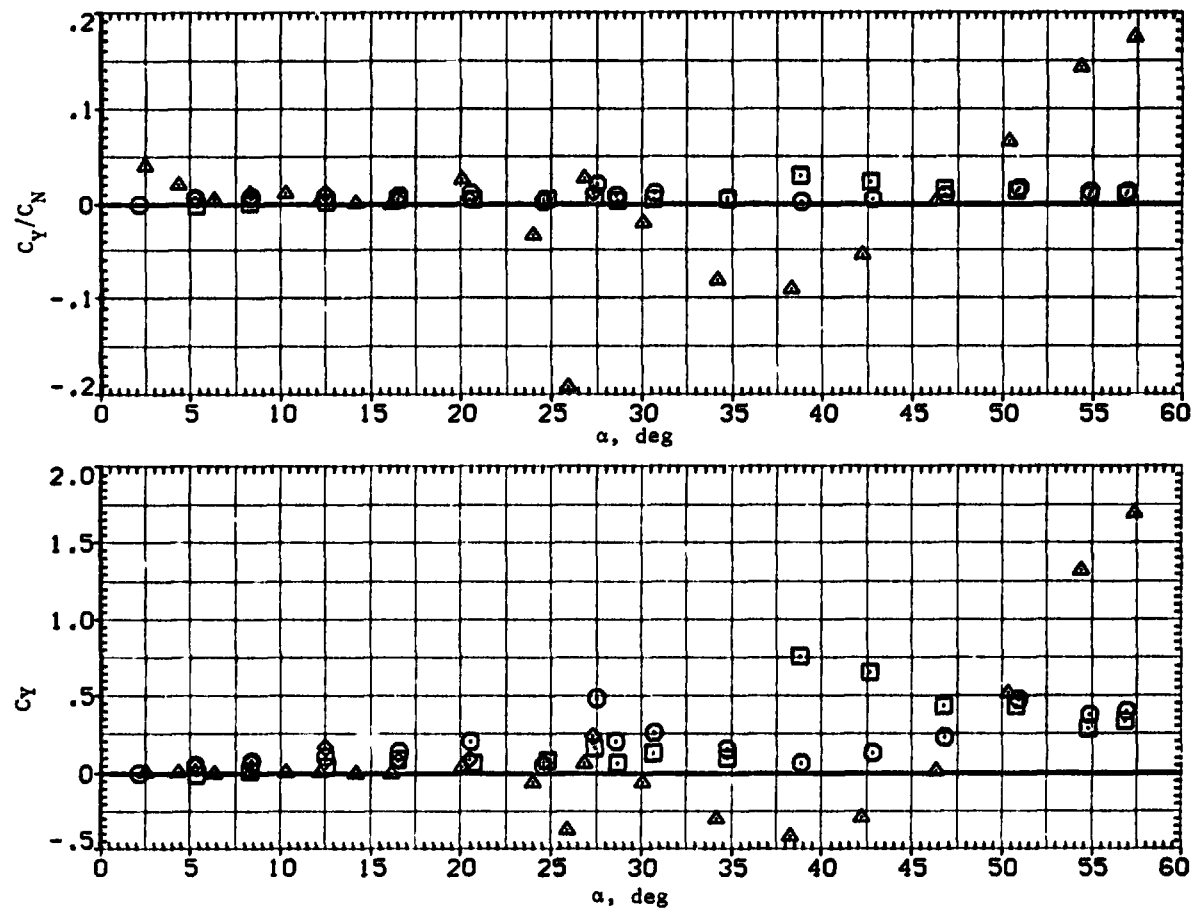
4.388

4.388

4.388

4.388

4.388



(b)  $C_Y/C_N$  and  $C_Y$  versus  $\alpha$ .

Figure 3.— Continued.

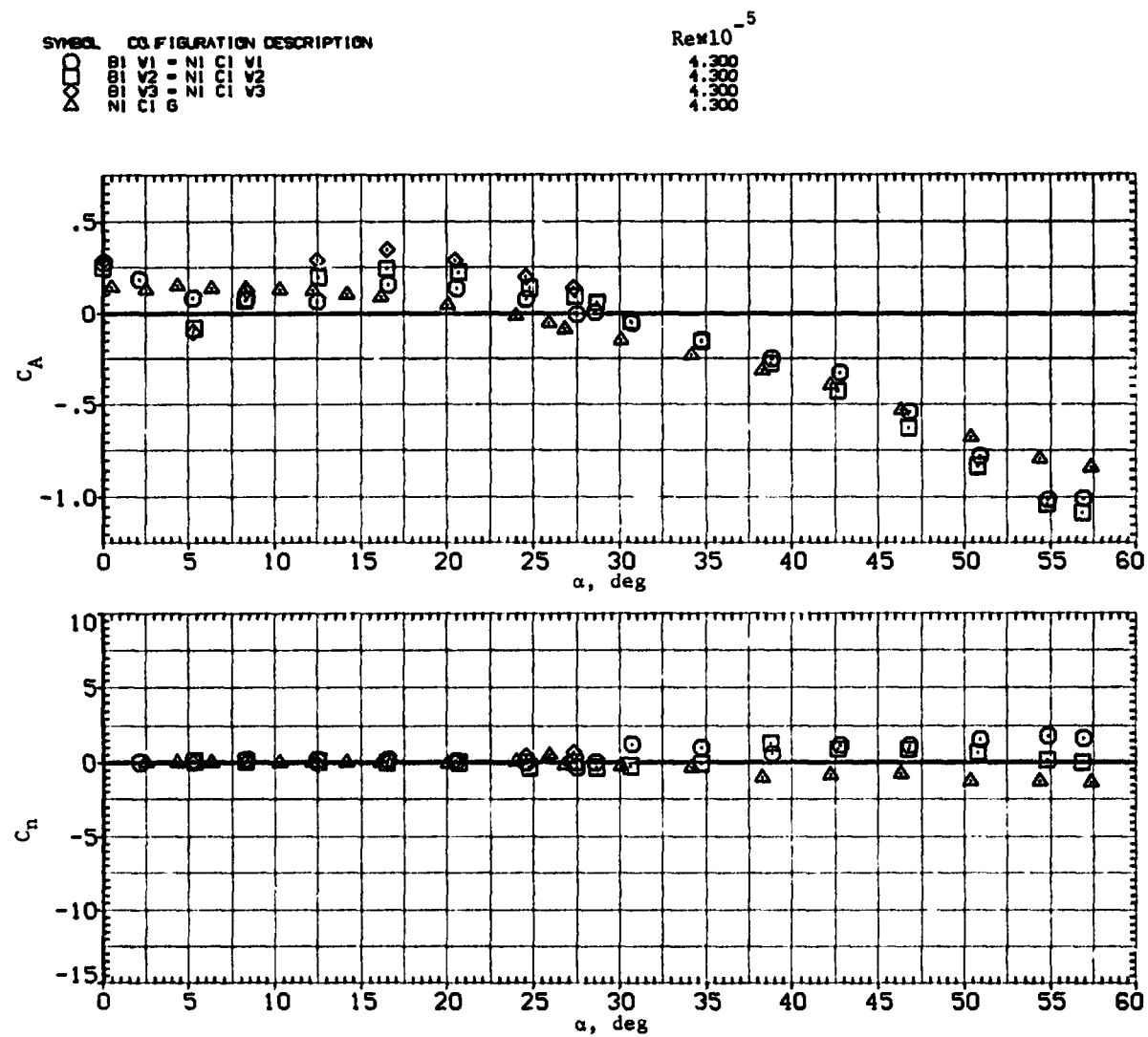
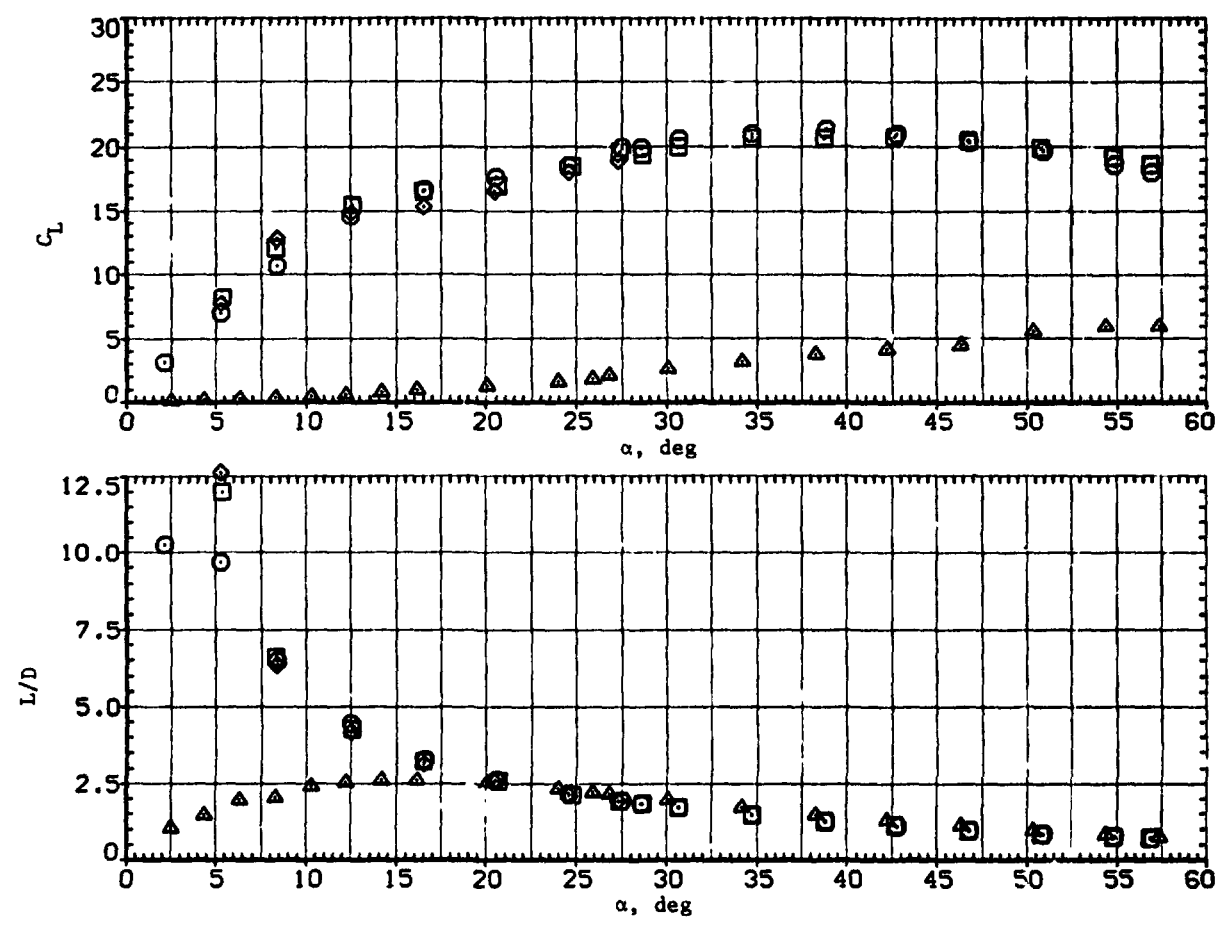
(c)  $C_A$  and  $C_n$  versus  $\alpha$ .

Figure 3.— Continued.

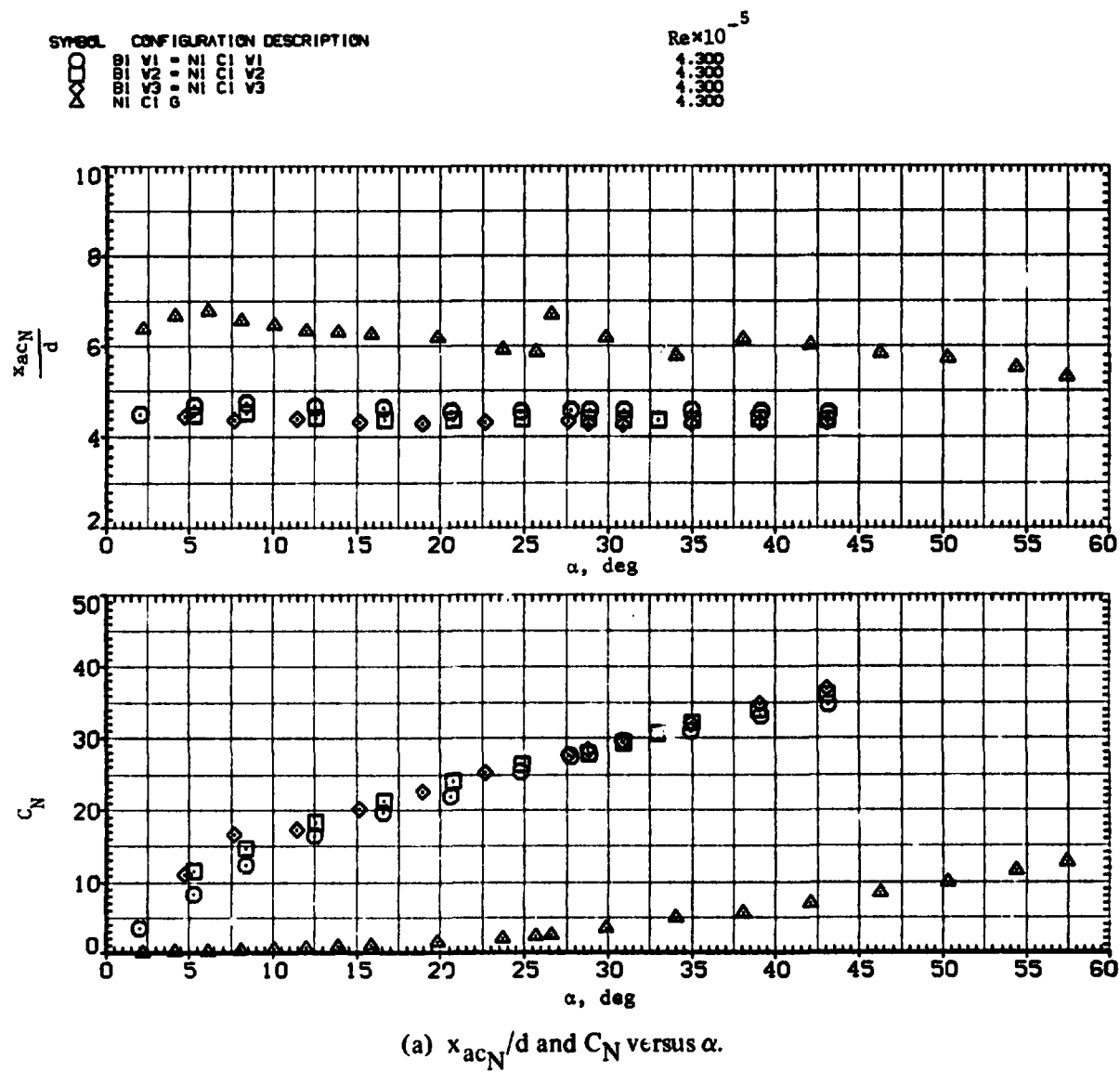
SYMBOL	CONFIGURATION DESCRIPTION	$Re \times 10^{-5}$
$\square$	B1 V1 = NI C1 V1	4.300
$\circ$	B1 V2 = NI C1 V2	4.300
$\triangle$	B1 V3 = NI C1 V3	4.300
$\diamond$	NI C1 G	4.300



(d)  $C_L$  and  $L/D$  versus  $\alpha$ .

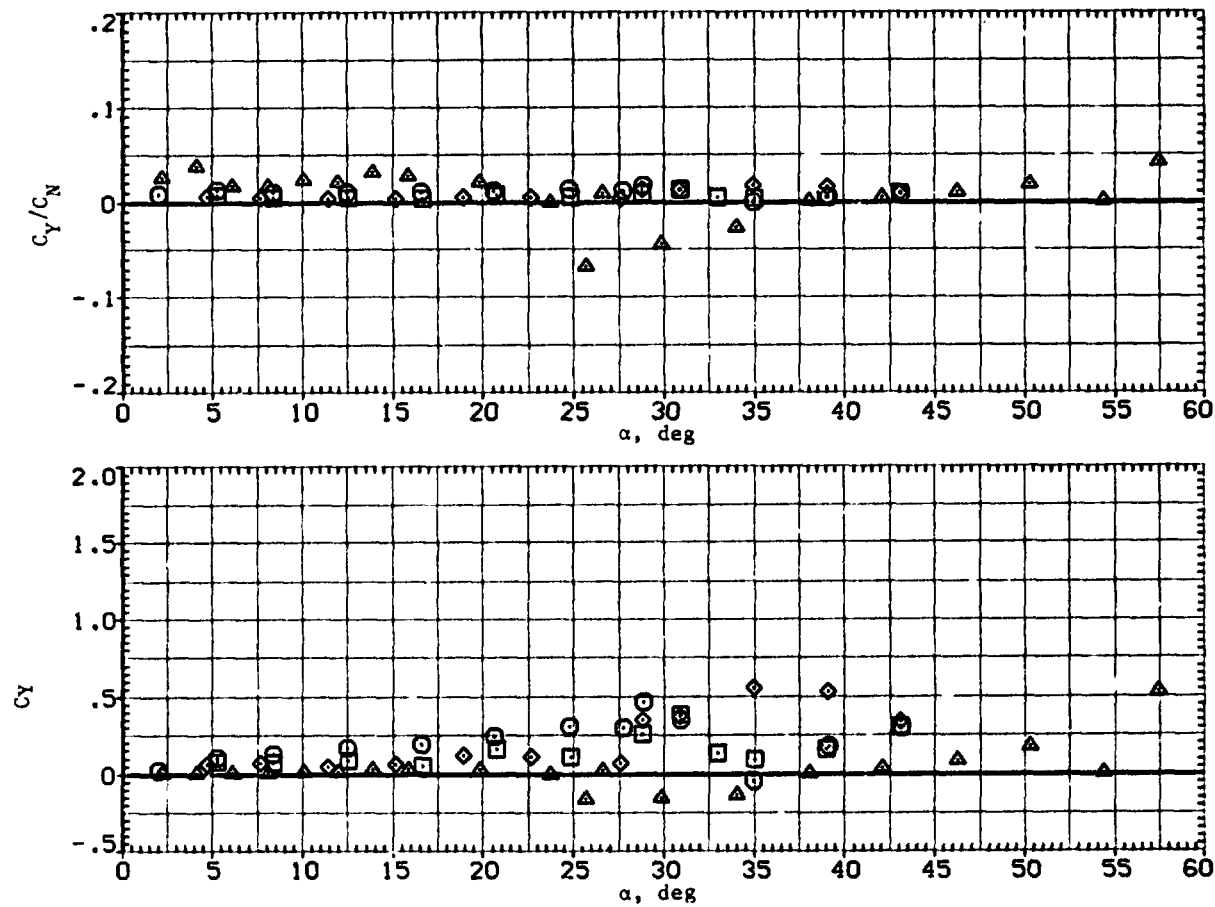
Figure 3.— Concluded.



Figure 4.— Effect of wing taper ratio with circular body;  $M = 0.9$ .

REPRODUCIBILITY OF THE  
ORIGINAL PAGE IS POOR

SYMBOL	CONFIGURATION DESCRIPTION	$Re \times 10^{-3}$
$\square$	BI V1 = NI C1 V1	4.300
$\circ$	BI V2 = NI C1 V2	4.300
$\triangle$	BI V3 = NI C1 V3	4.300
$\diamond$	NI C1 G	4.300



(b)  $C_Y/C_N$  and  $C_Y$  versus  $\alpha$ .

Figure 4.- Continued.

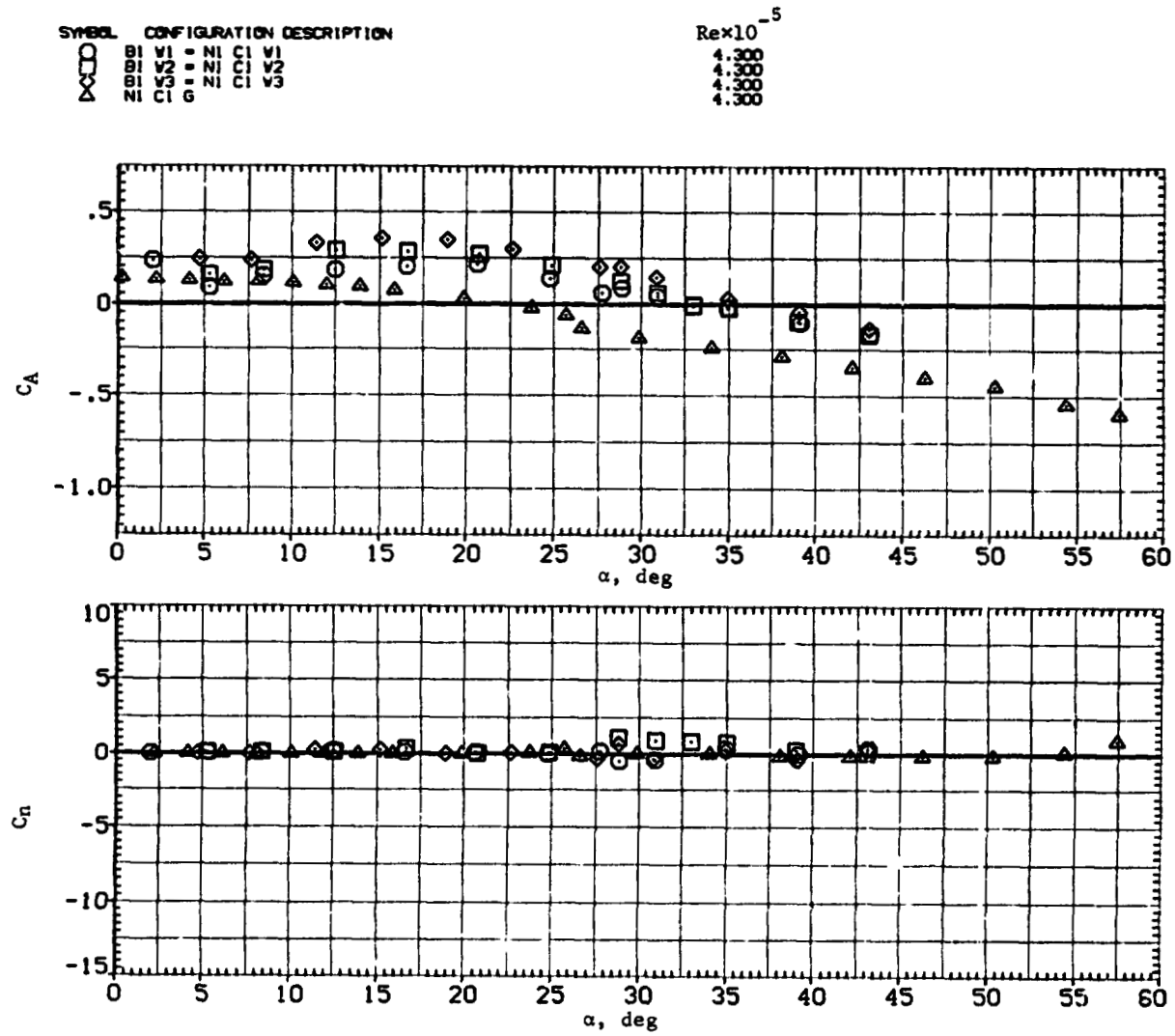
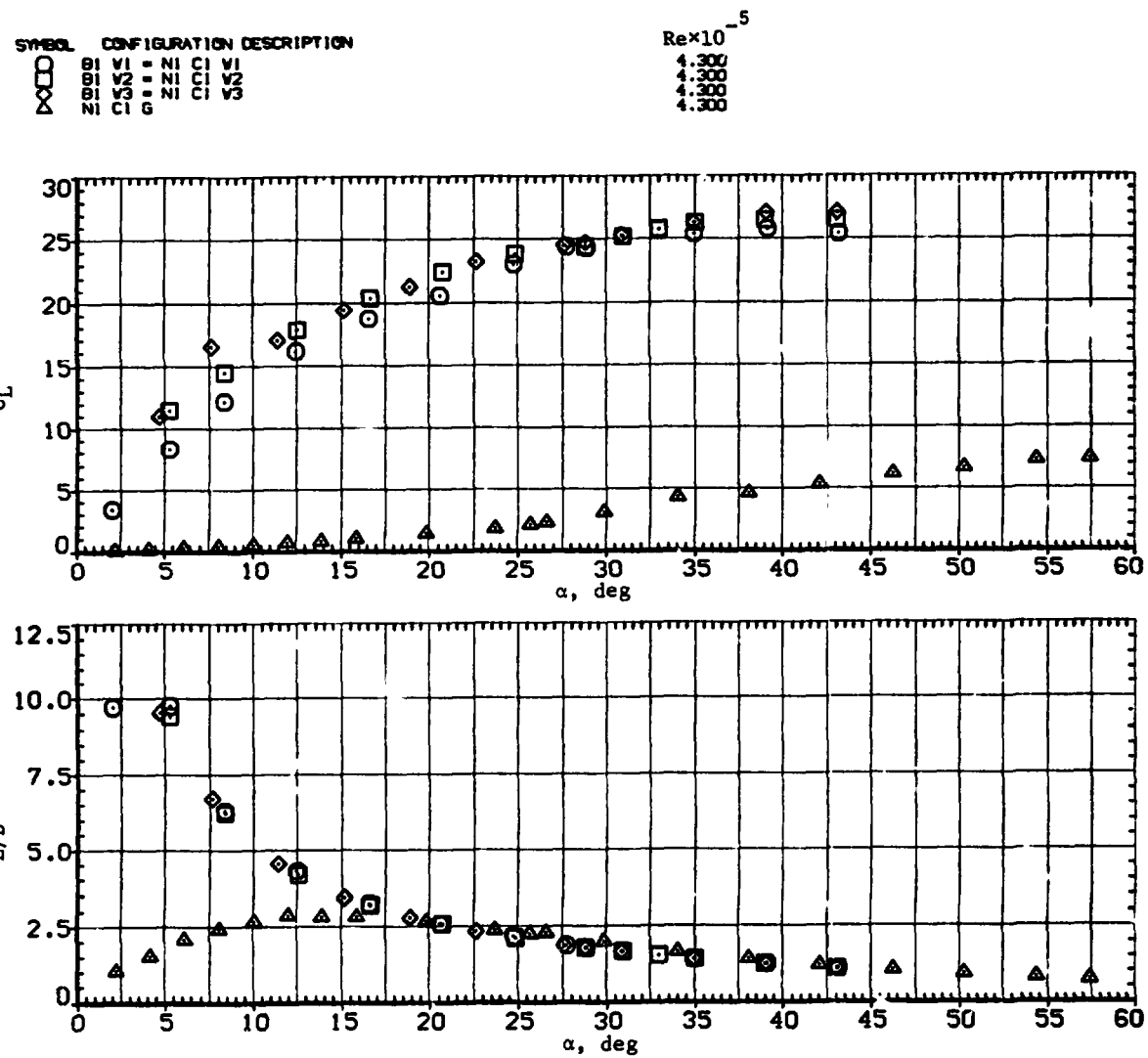
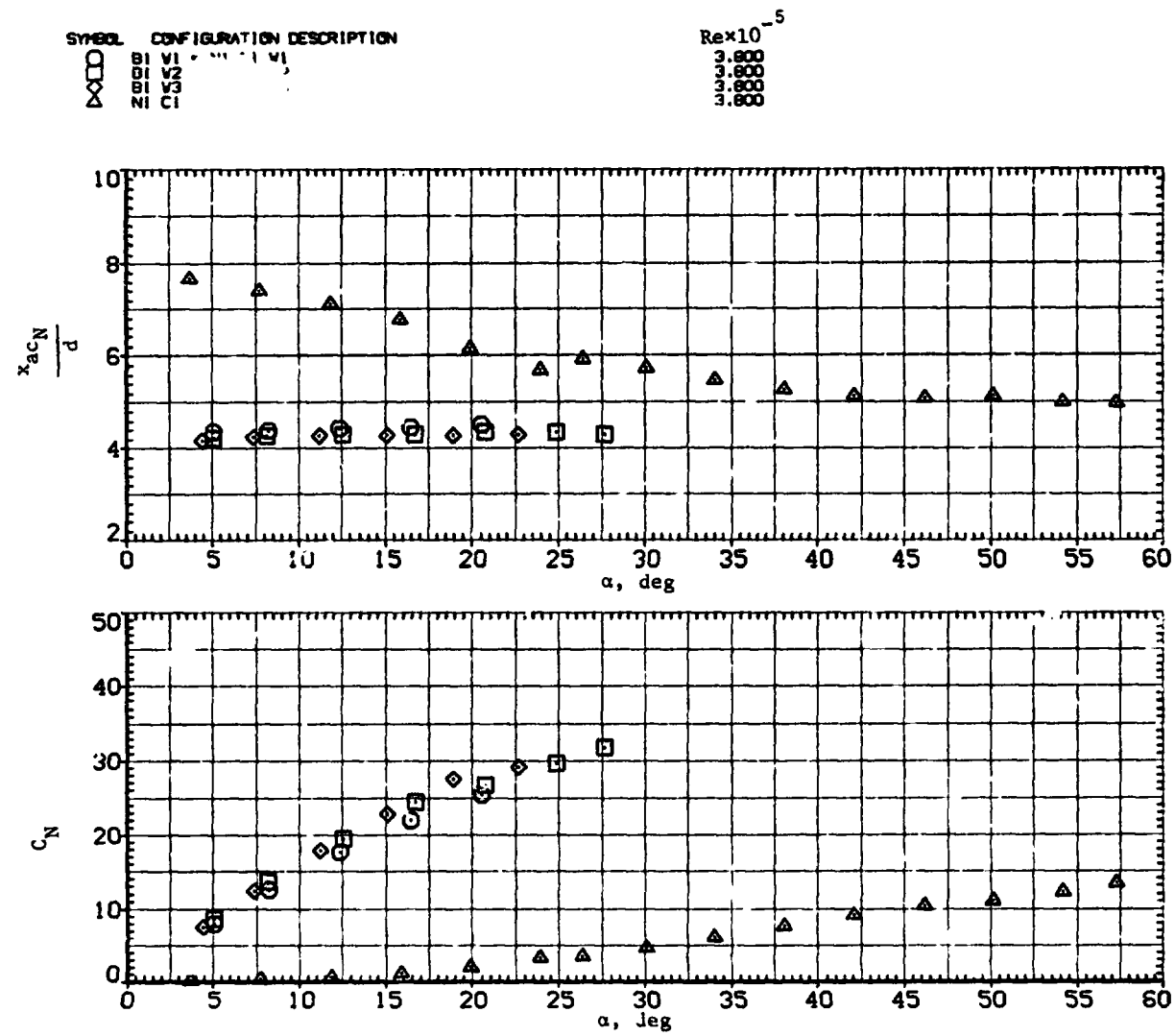
(c)  $C_A$  and  $C_n$  versus  $\alpha$ .

Figure 4.— Continued.



(d)  $C_L$  and  $L/D$  versus  $\alpha$ .

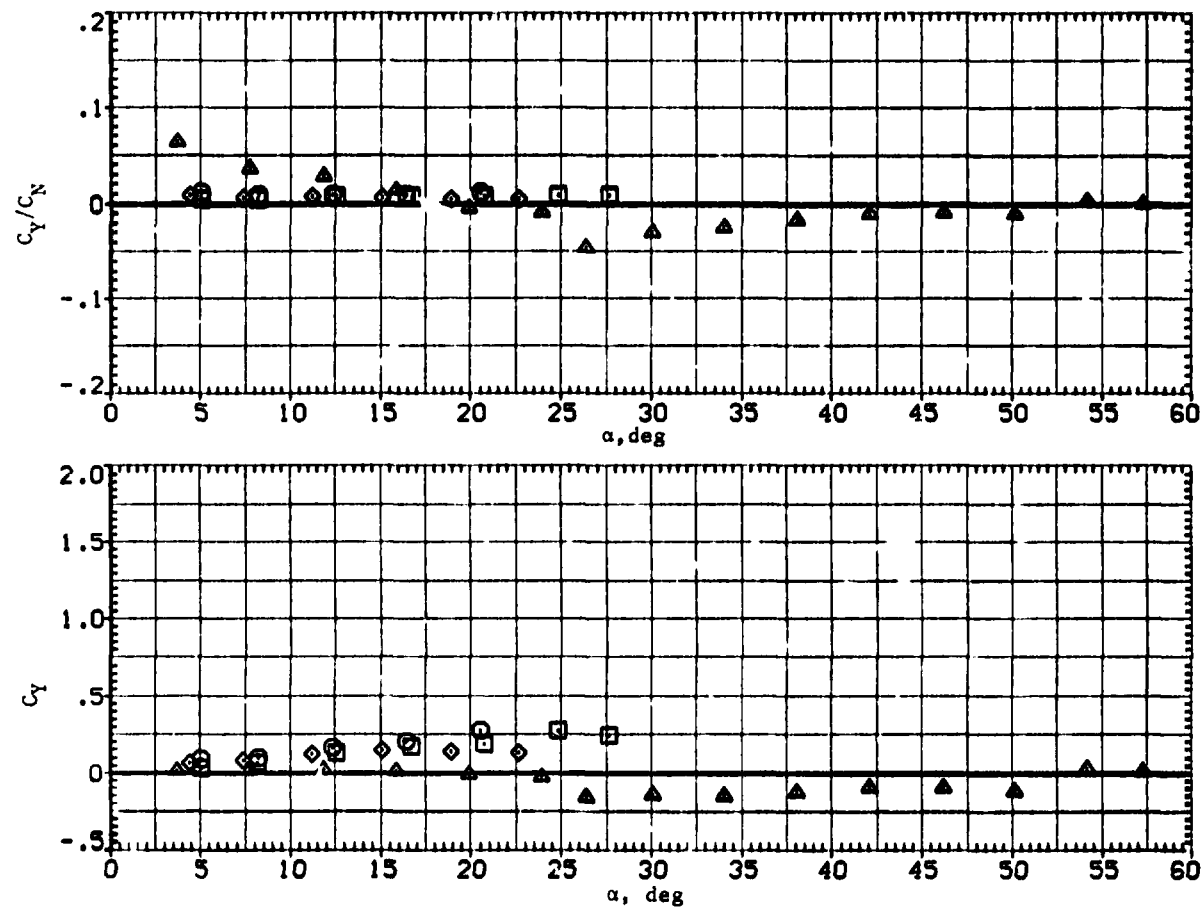
Figure 4.— Concluded.



(a)  $x_{acN}/d$  and  $C_N$  versus  $\alpha$ .

Figure 5.-- Effect of wing taper ratio with circular body;  $M = 1.2$ .

SYMBOL	CONFIGURATION DESCRIPTION	$Re \times 10^{-5}$
$\square$	B1 V1 = ZZ C1 V1	3.888
$\diamond$	B1 V2 = ZZ C1 V2	3.888
$\triangle$	B1 V3 = ZZ C1 V3	3.888
$\square$	B1 V1 = ZZ C1 V1	3.888
$\diamond$	B1 V2 = ZZ C1 V2	3.888
$\triangle$	B1 V3 = ZZ C1 V3	3.888



(b)  $C_Y/C_N$  and  $C_Y$  versus  $\alpha$ .

Figure 5.-- Continued.

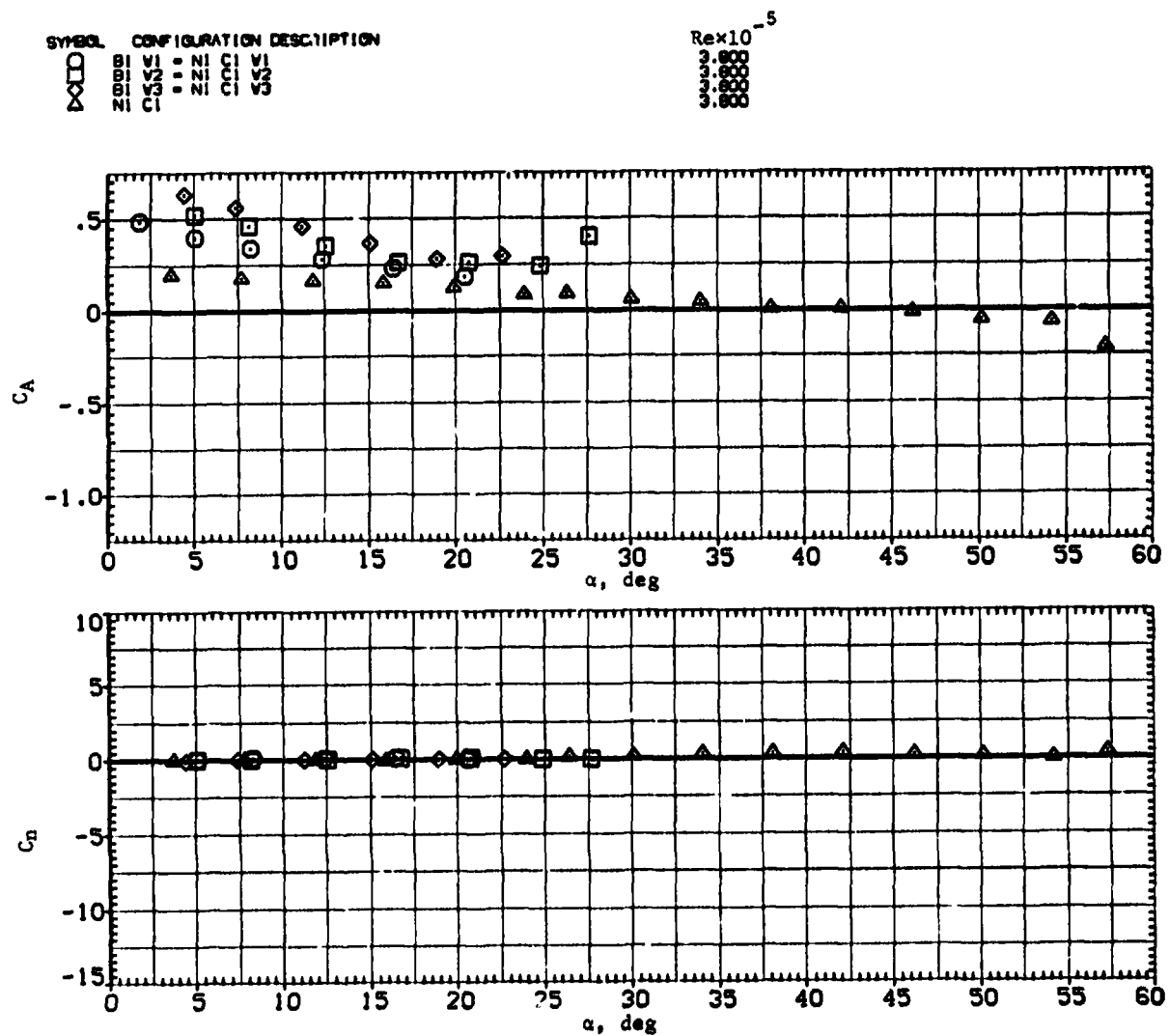
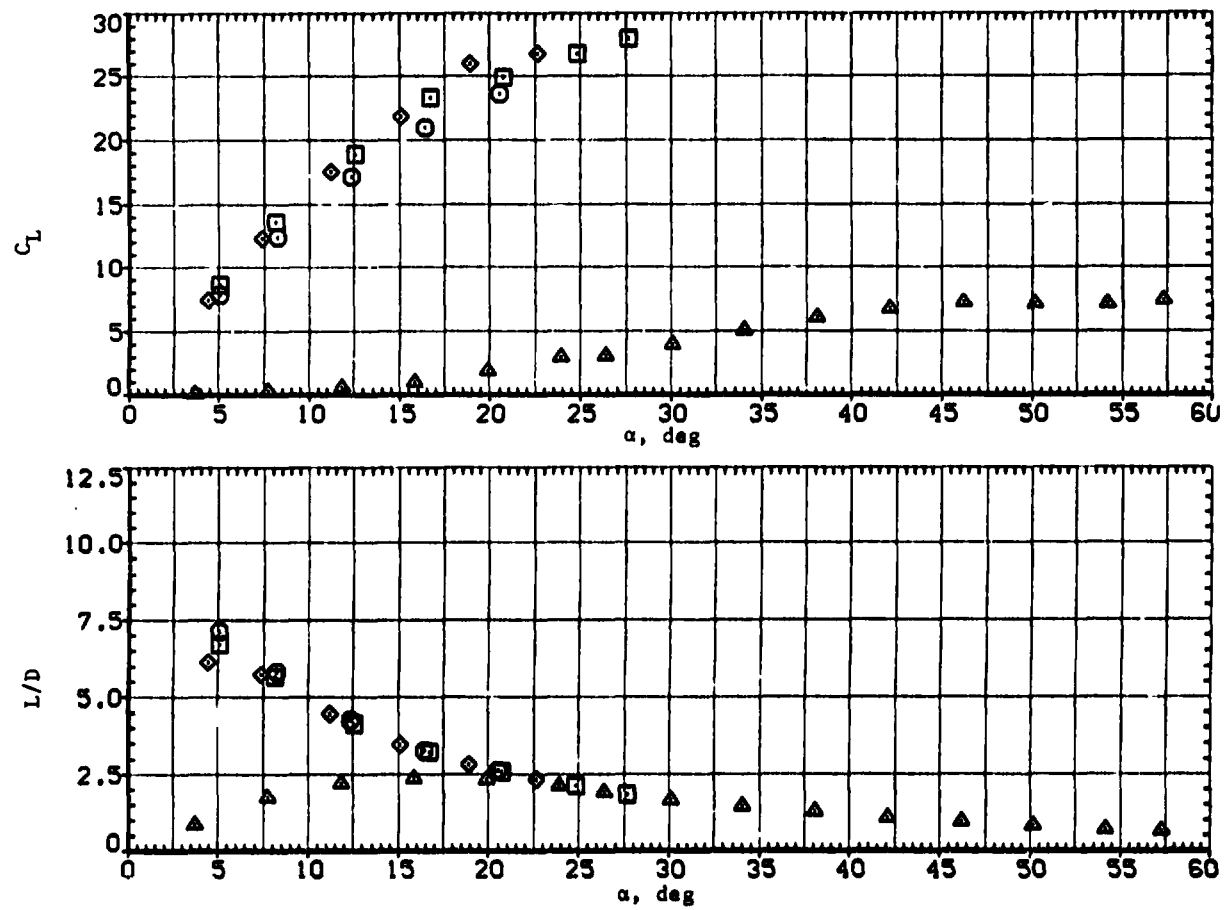
(c)  $C_A$  and  $C_n$  versus  $\alpha$ .

Figure 5. - Continued.

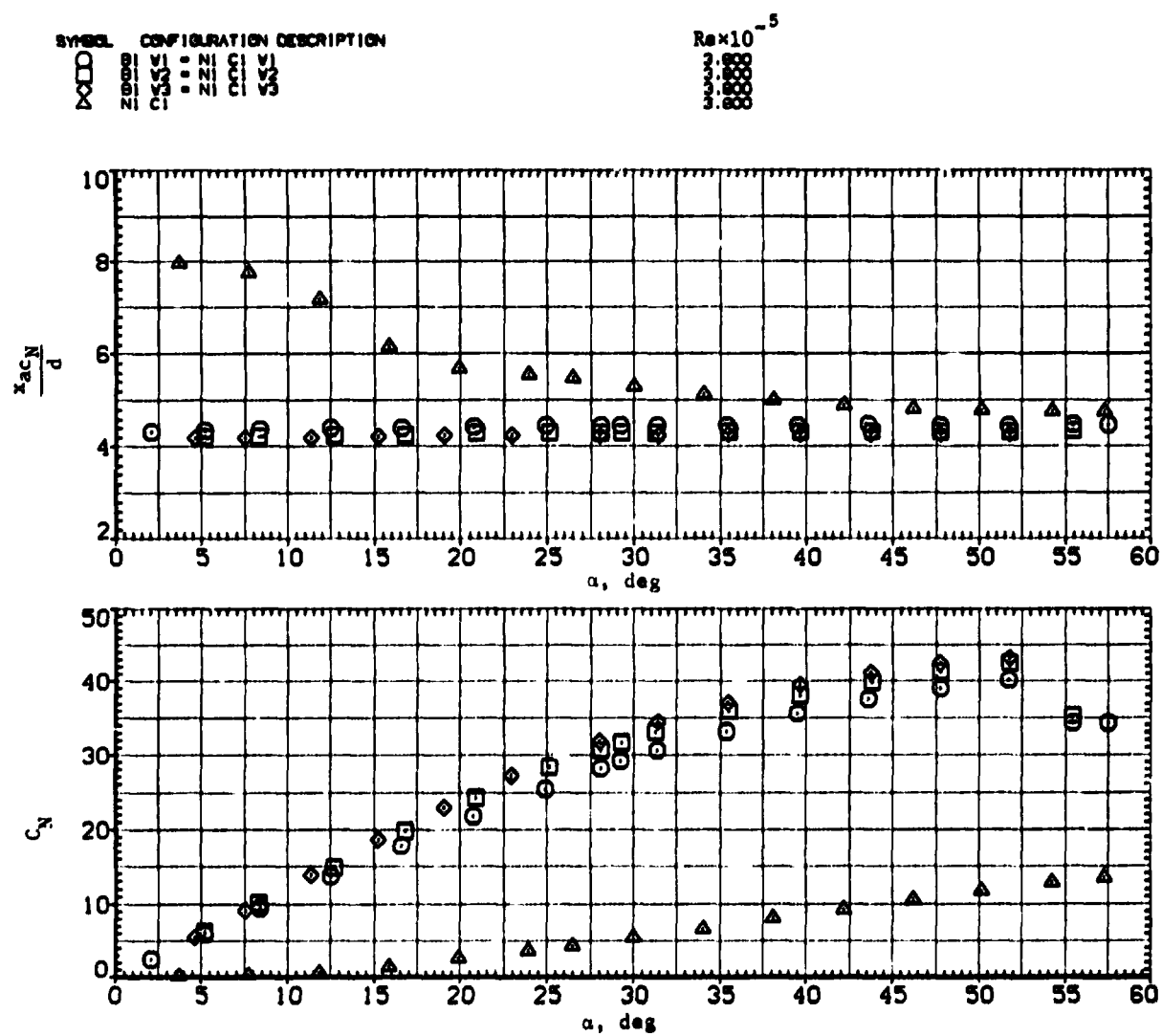


SYMBOL	CONFIGURATION DESCRIPTION	$Re \times 10^{-5}$
$\diamond$	NI	3.0
$\square$	CT	3.0
$\circ$	NI	3.0
$\times$	CT	3.0
$\cdot$	NI	3.0
$\circ$	CT	3.0
$\times$	NI	3.0
$\cdot$	CT	3.0
$\diamond$	NI	3.0
$\square$	CT	3.0
$\circ$	NI	3.0
$\times$	CT	3.0
$\cdot$	NI	3.0
$\circ$	CT	3.0
$\times$	NI	3.0
$\cdot$	CT	3.0



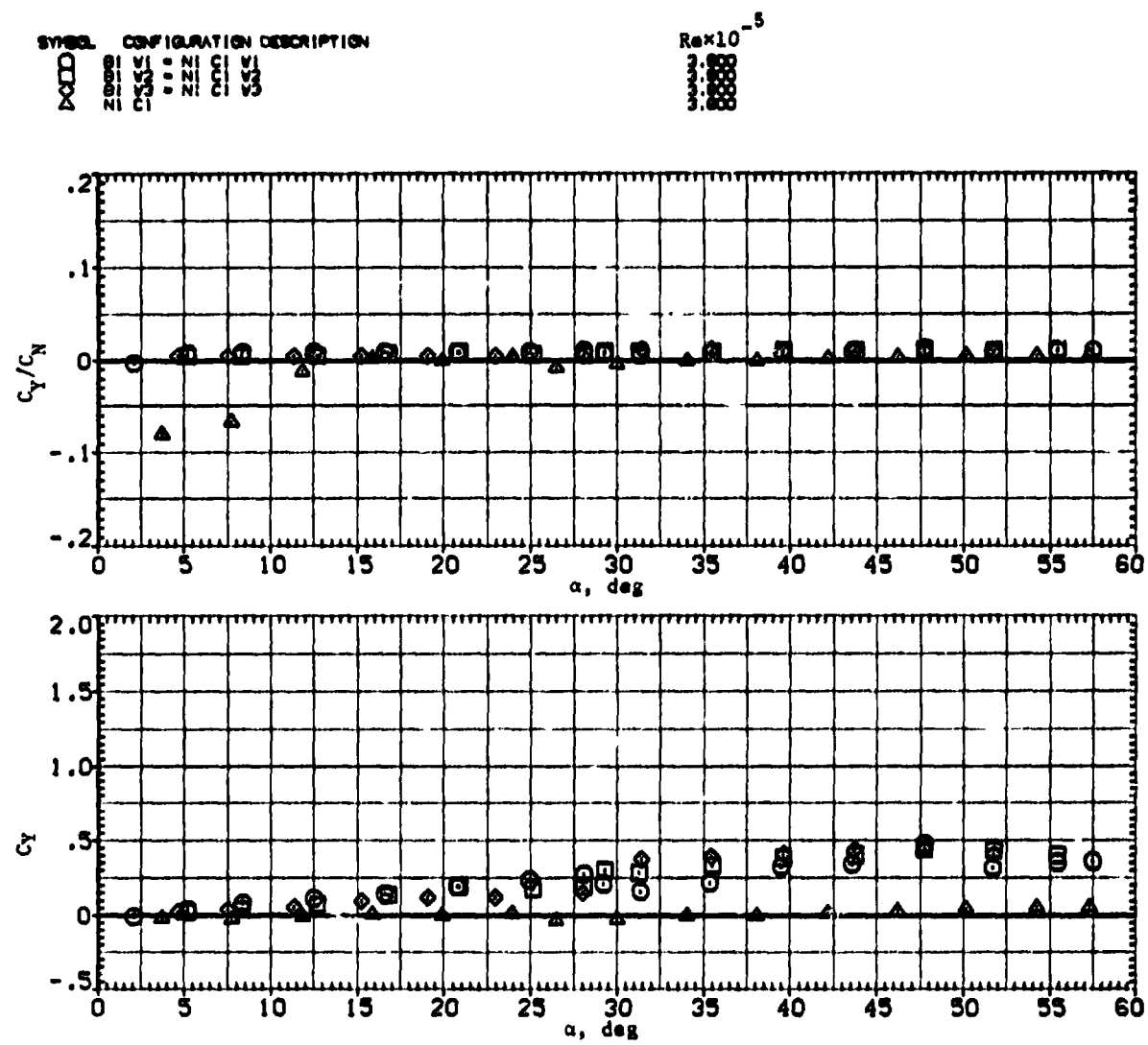
(d)  $C_L$  and  $L/D$  versus  $\alpha$ .

Figure 5.— Concluded.



(a)  $x_{acN}/d$  and  $C_N$  versus  $\alpha$ .

**Figure 6. -- Effect of wing taper ratio with circular body;  $M = 1.5$ .**



(b)  $C_Y/C_N$  and  $C_Y$  versus  $\alpha$ .

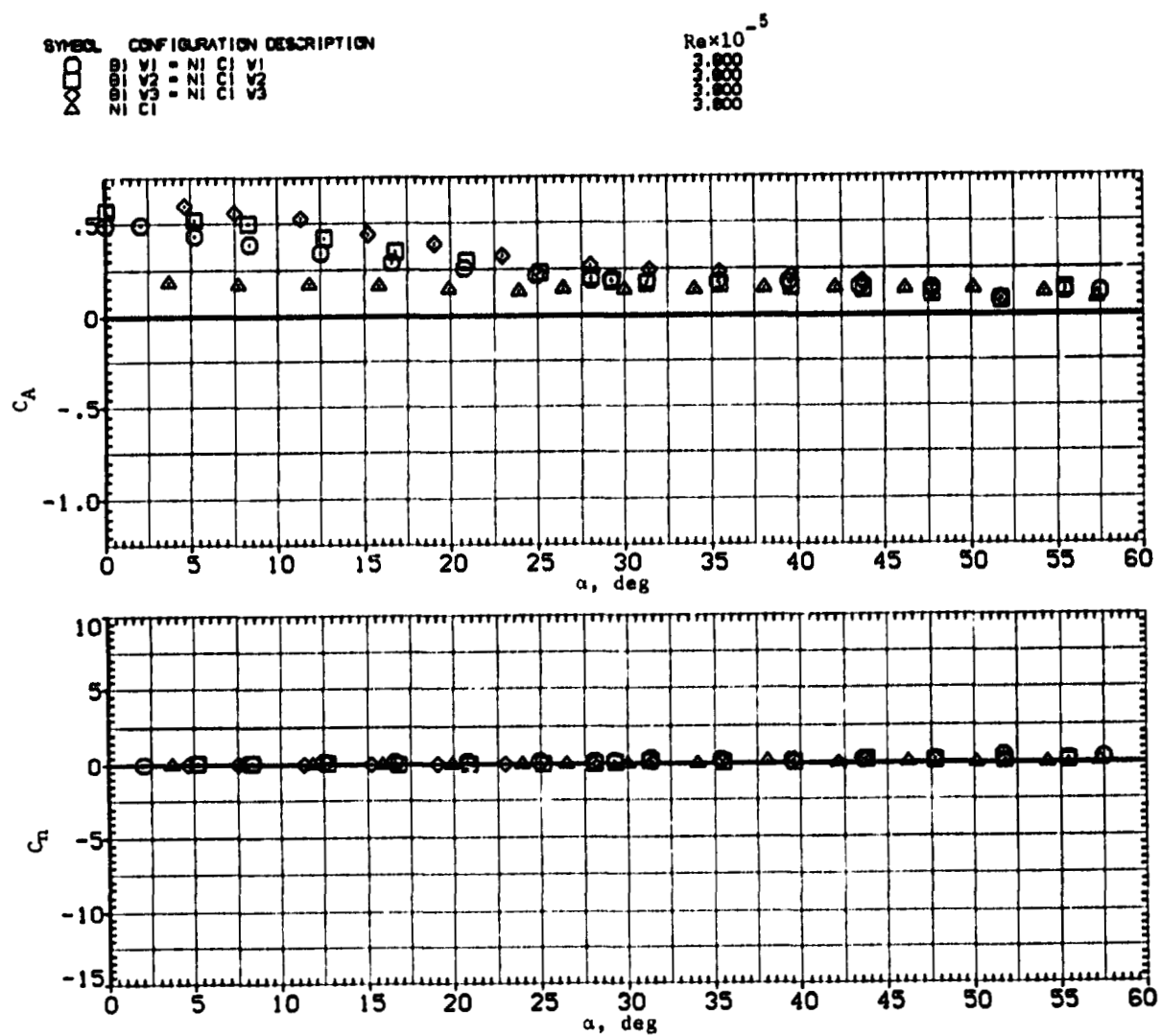
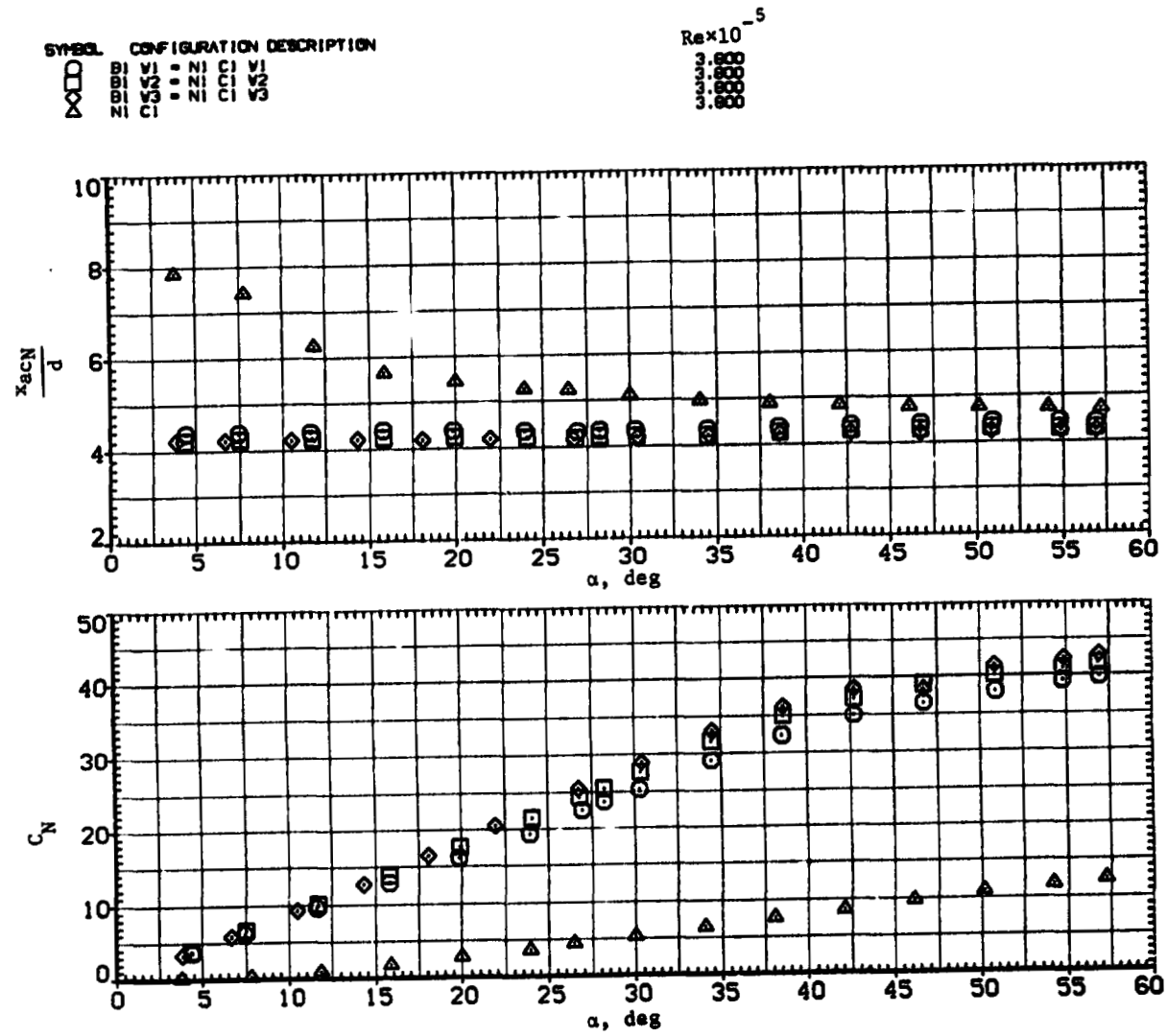
(c)  $C_A$  and  $C_n$  versus  $\alpha$ .

Figure 6. - Continued.

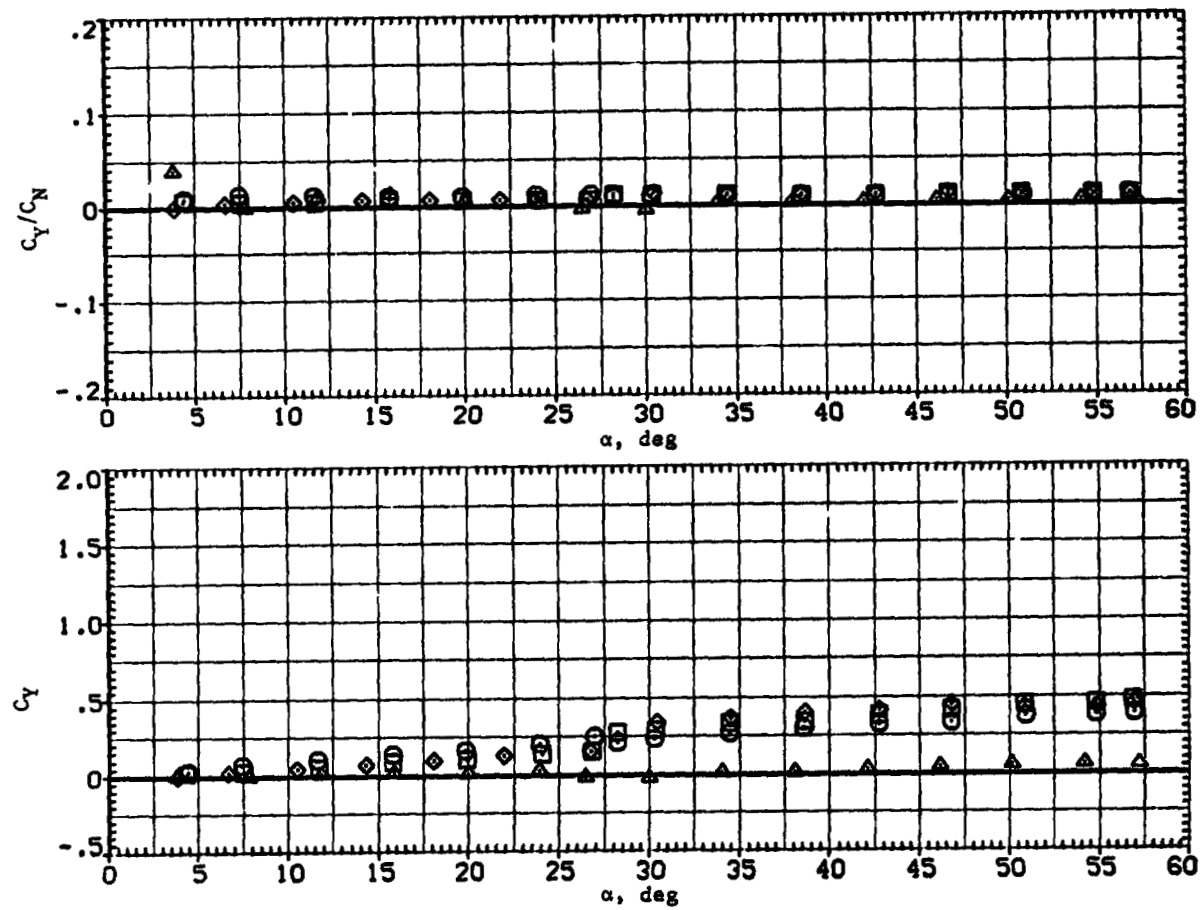




(a)  $x_{acN}/d$  and  $C_N$  versus  $\alpha$ .

Figure 7.— Effect of wing taper ratio with circular body;  $M = 2.0$ .

SYMBOL	CONFIGURATION DESCRIPTION	$Re \times 10^{-5}$
$\square$	BI V1 = NI C1 V1	3.3000
$\diamond$	BI V2 = NI C1 V2	3.3000
$\triangle$	BI V3 = NI C1 V3	3.3000
$\square$	NI C1	3.3000



(b)  $C_Y/C_N$  and  $C_Y$  versus  $\alpha$ .

Figure 7.— Continued.



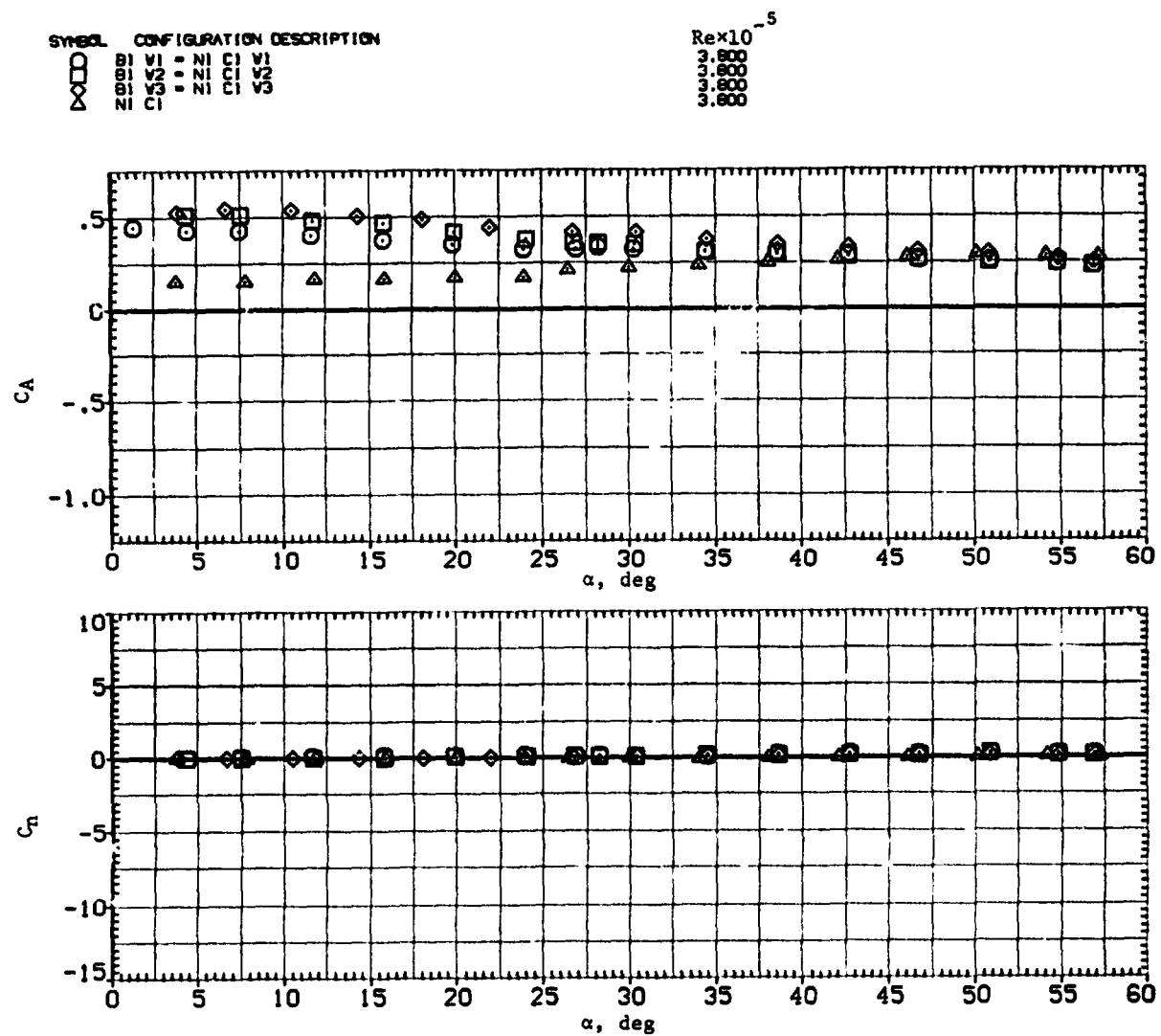
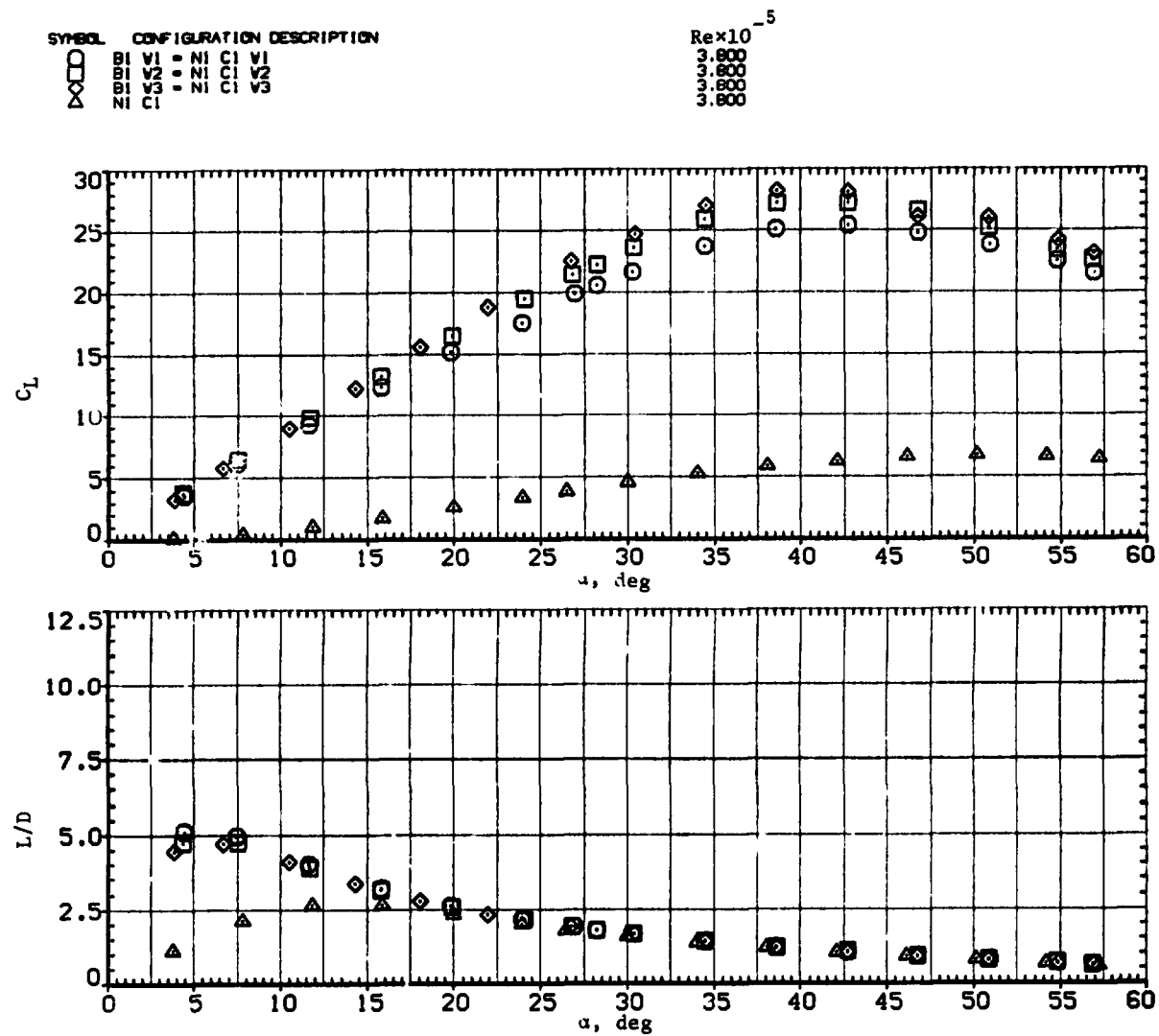
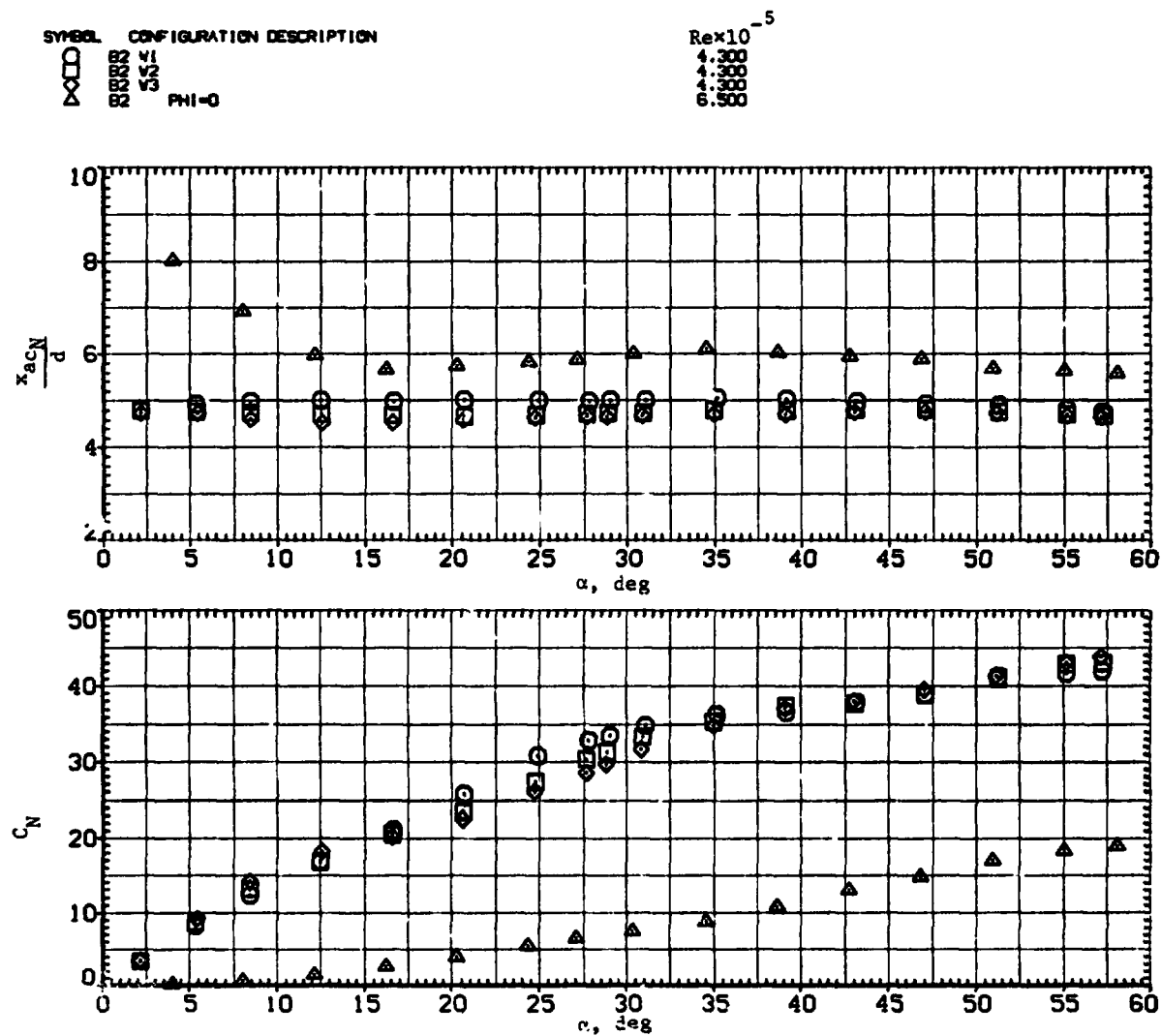
(c)  $C_A$  and  $C_n$  versus  $\alpha$ .

Figure 7. - Continued.



(d)  $C_L$  and  $L/D$  versus  $\alpha$ .

Figure 7.— Concluded.

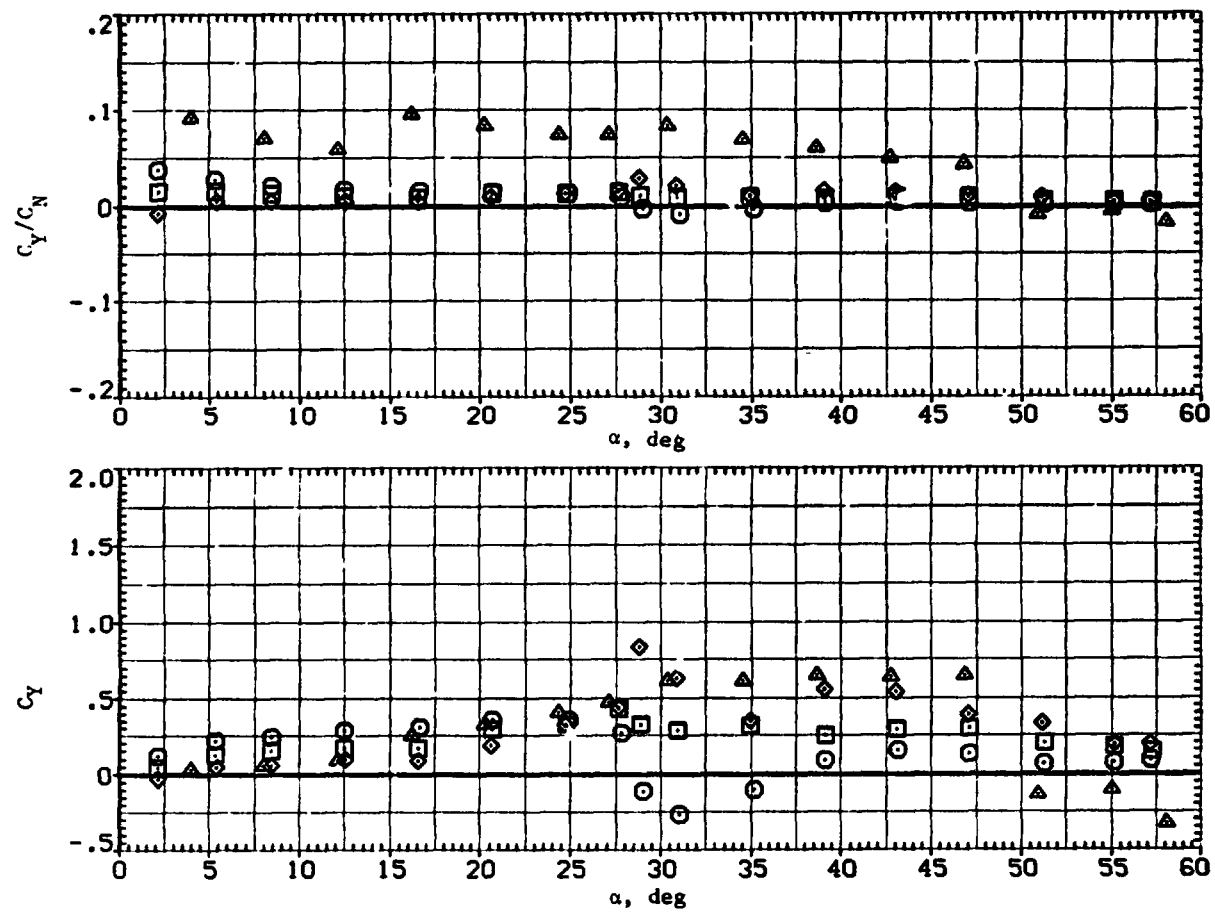


(a)  $x_{acN}/d$  and  $C_N$  versus  $\alpha$ .

Figure 8.— Effect of wing taper ratio with elliptic body;  $M = 0.6$ .

SYMBOL	CONFIGURATION DESCRIPTION	$Re \times 10^{-5}$
C	1	4.300
□	2	4.300
△	3	4.300
◇	4	6.500

PHI=0



(b)  $C_Y/C_N$  and  $C_Y$  versus  $\alpha$ .

Figure 8.— Continued.

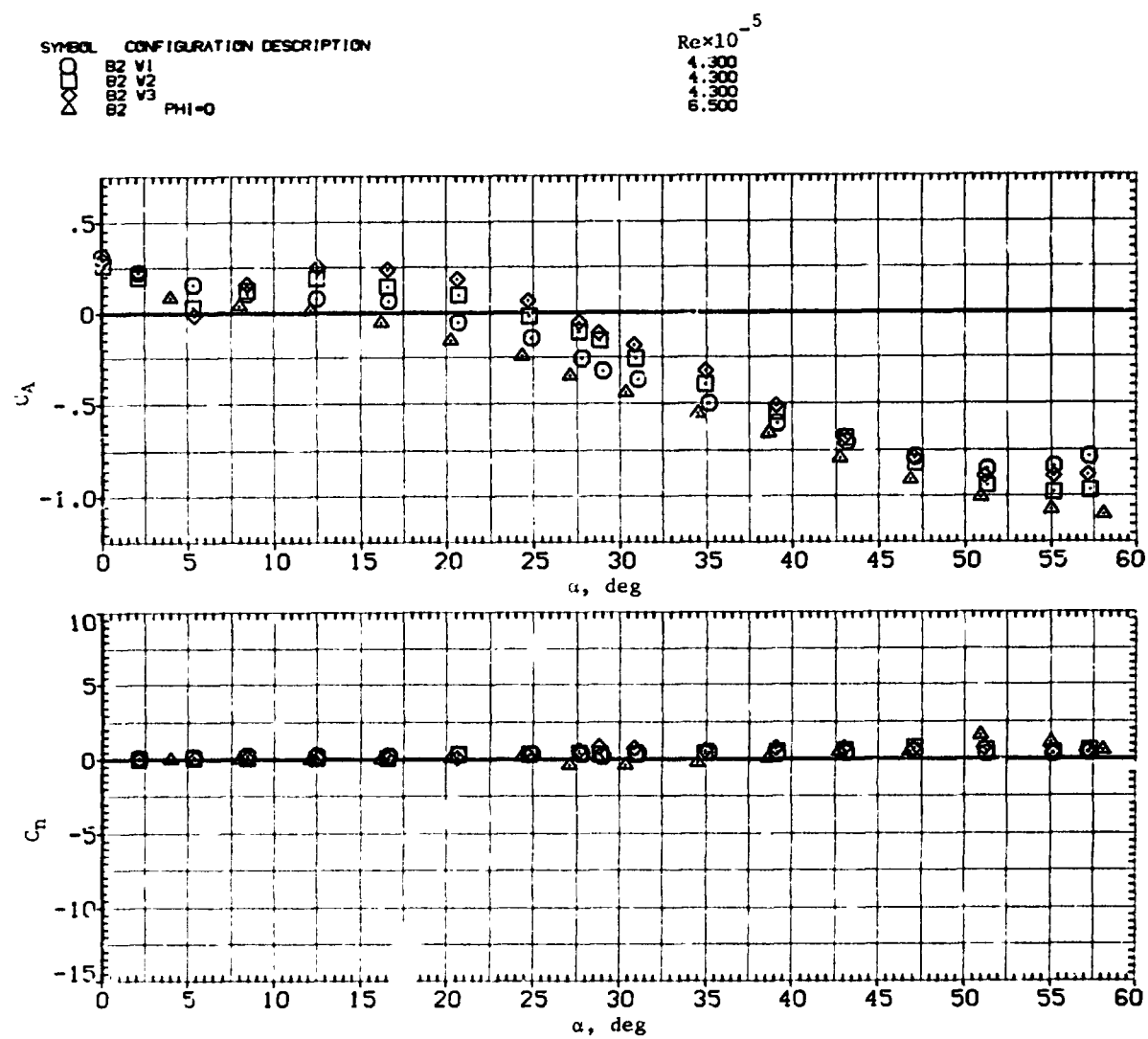


Figure 8. - Continued.



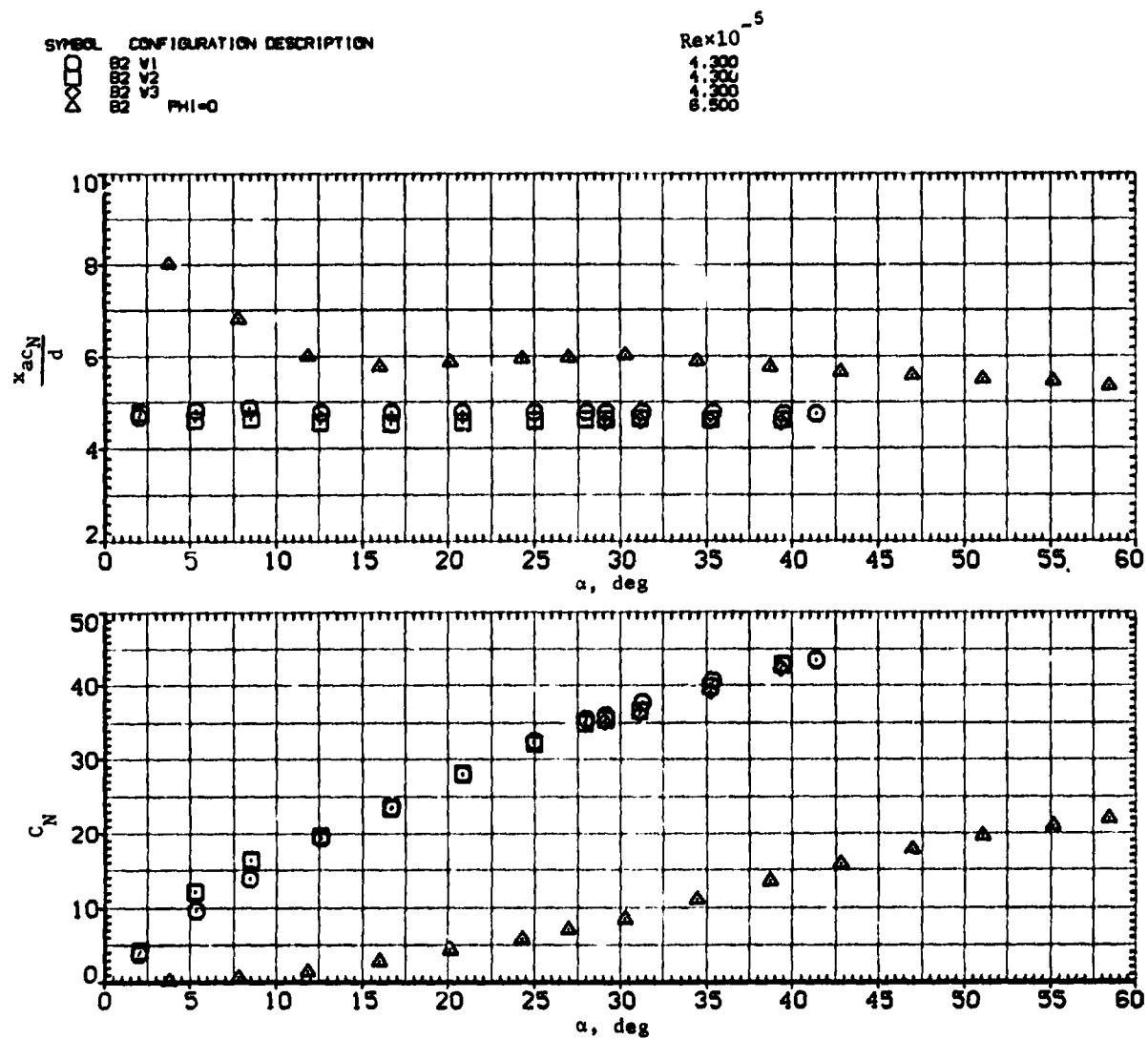


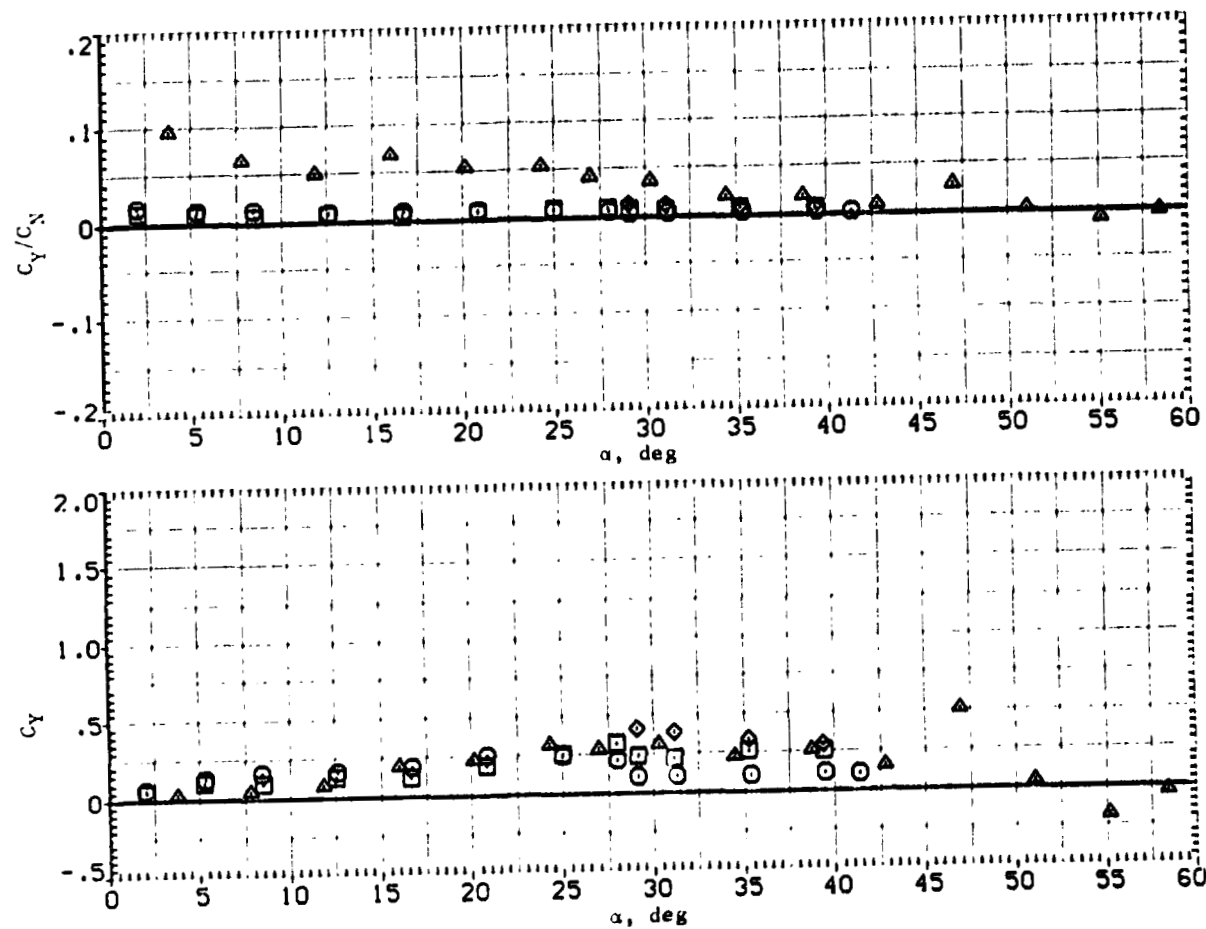
Figure 9.— Effect of wing taper ratio with elliptic body;  $M = 0.9$ .

SYMBOL CONFIGURATION DESCRIPTION

□	B2 V1
○	B2 V2
△	B2 V3
△	B2 PHI=0

$Re \times 10^{-5}$

4.300
4.300
4.300
6.500



(b)  $C_Y/C_N$  and  $C_Y$  versus  $\alpha$ .

Figure 9. - Continued.



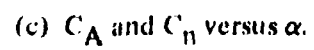
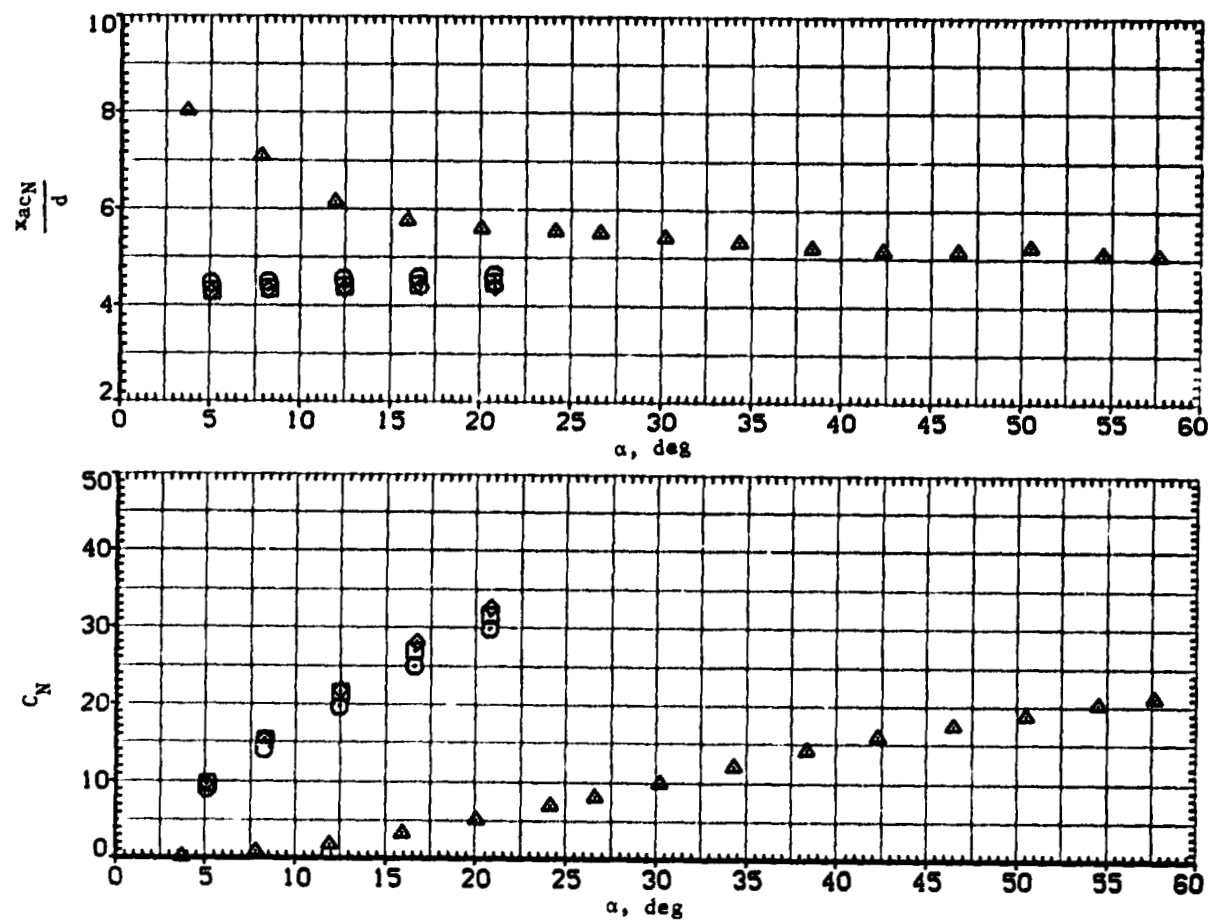


**Figure 9. Continued.**



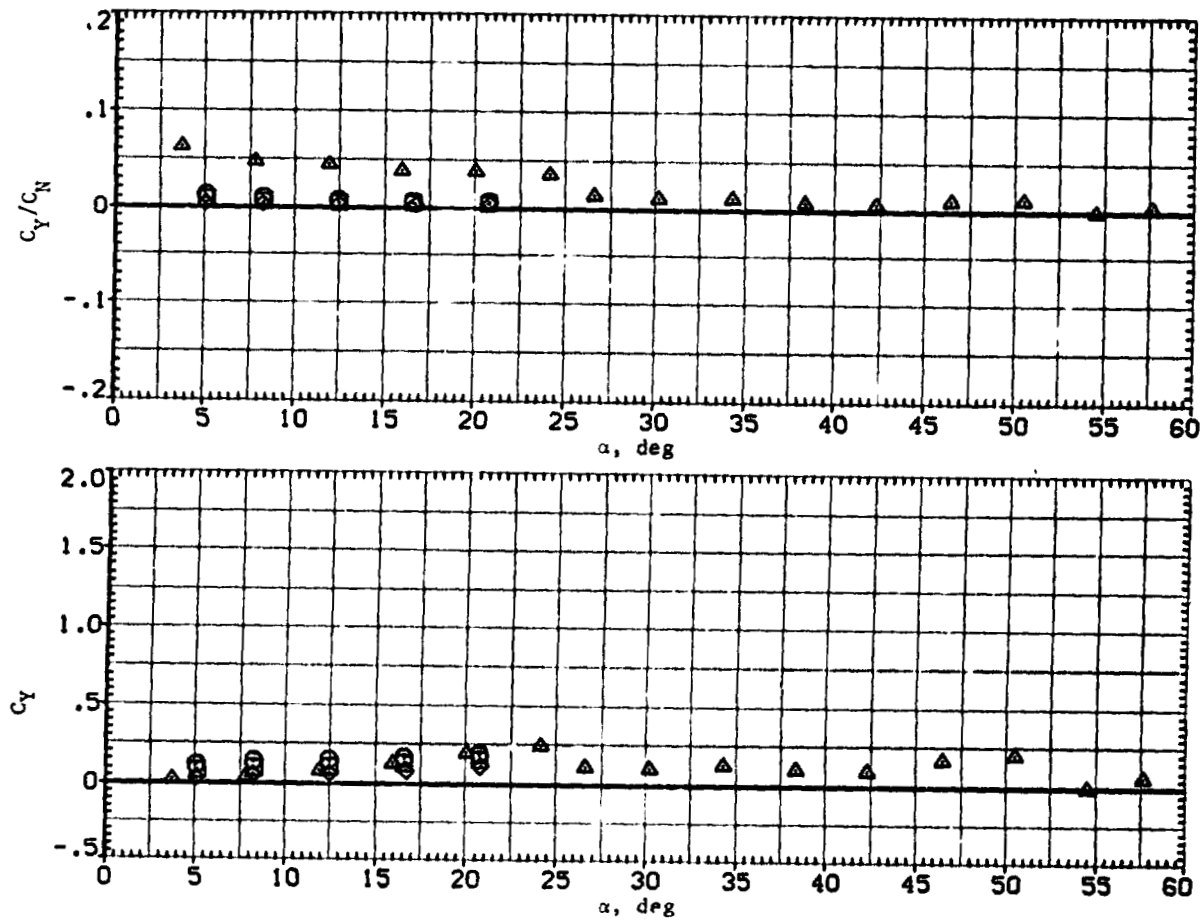


(a)  $x_{acN}/d$  and  $C_N$  versus  $\alpha$ .

**Figure 10.-- Effect of wing taper ratio with elliptic body;  $M = 1.2$ .**

SYMBOL CONFIGURATION DESCRIPTION  
 ○ V1  
 ⊗ V2  
 ⊗ V3  
 PHI=0

$Re \times 10^{-5}$   
 3.800  
 3.800  
 3.800  
 3.800



(b)  $C_Y/C_N$  and  $C_Y$  versus  $\alpha$ .

Figure 10.- Continued.

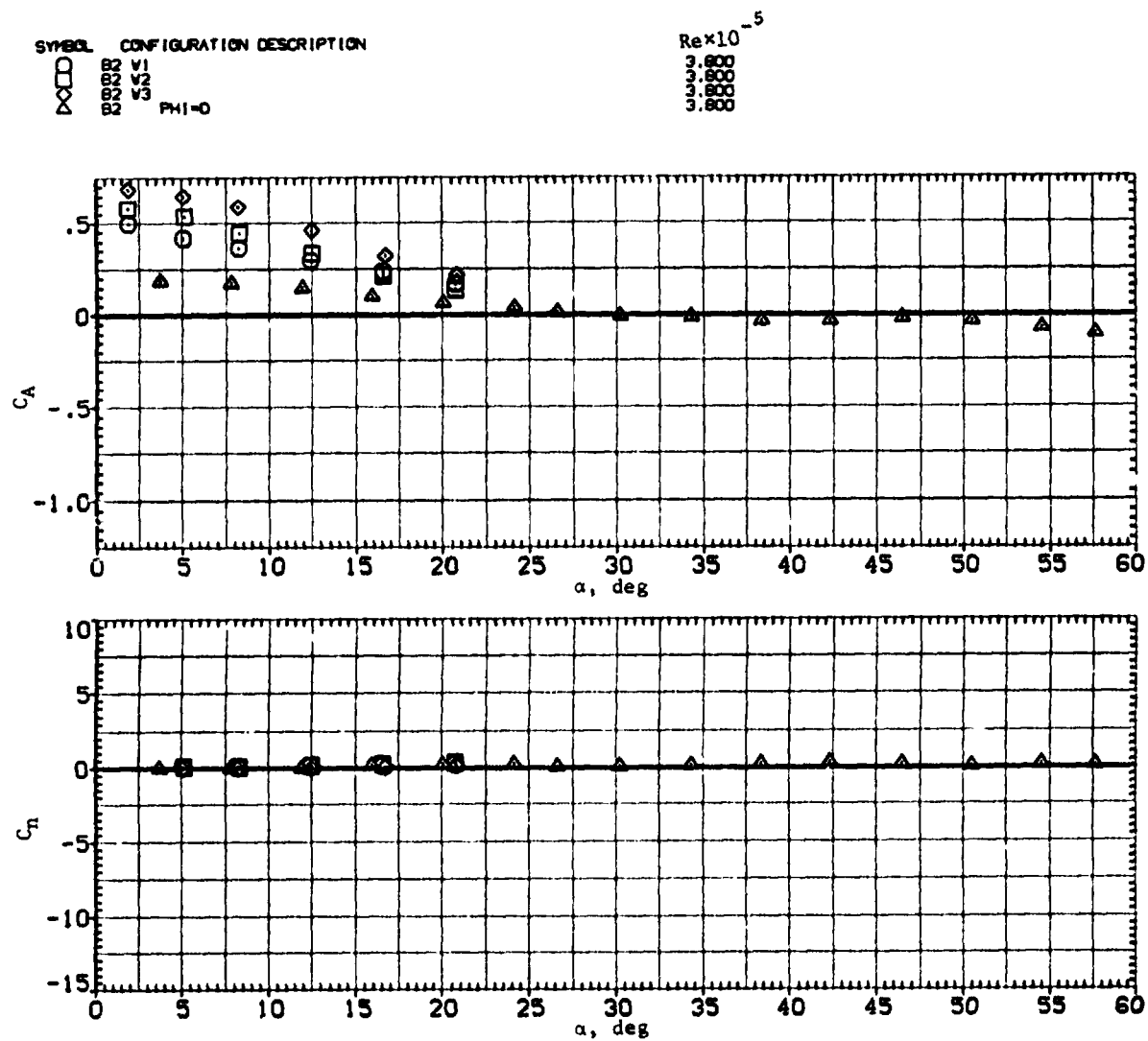
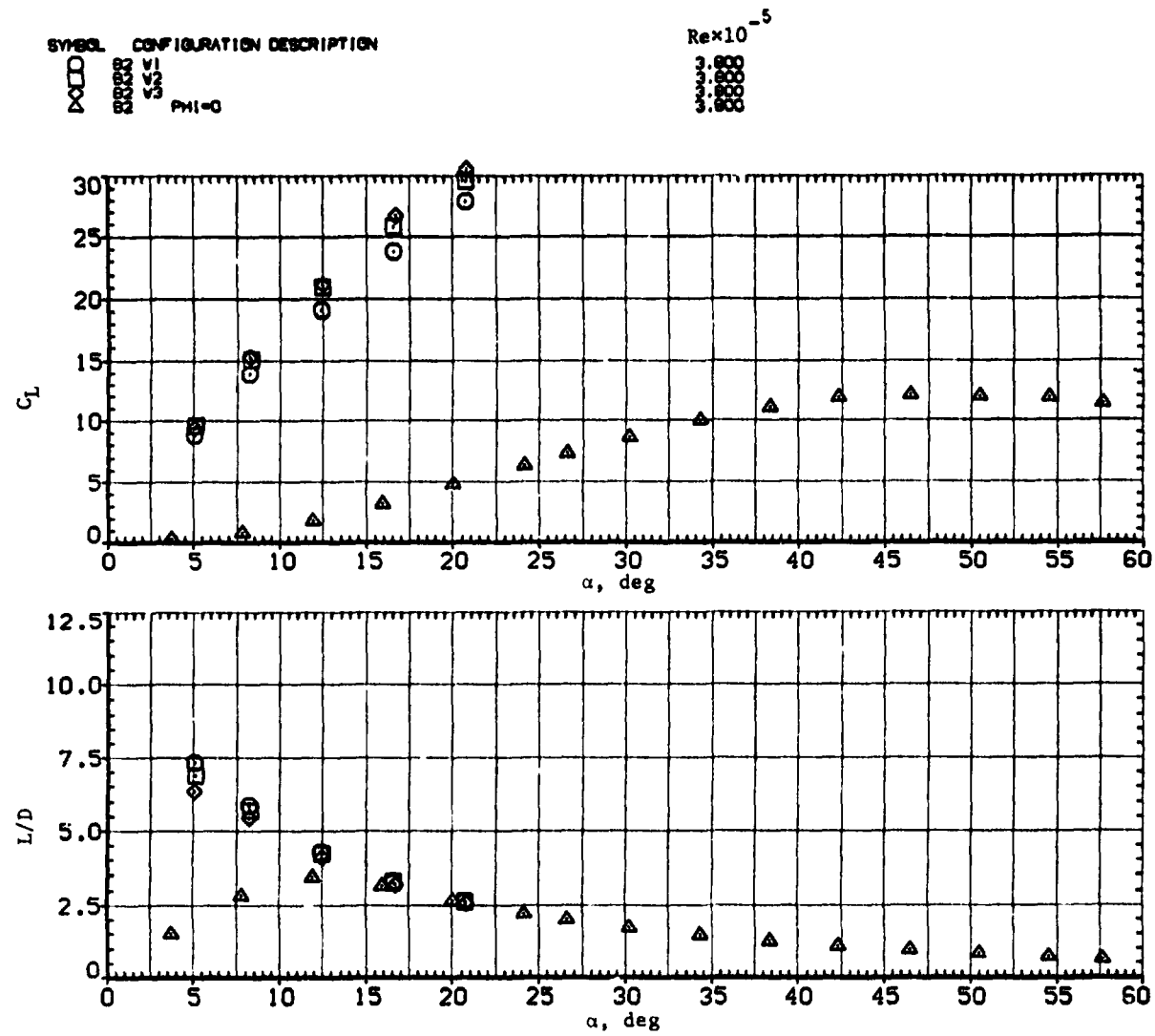
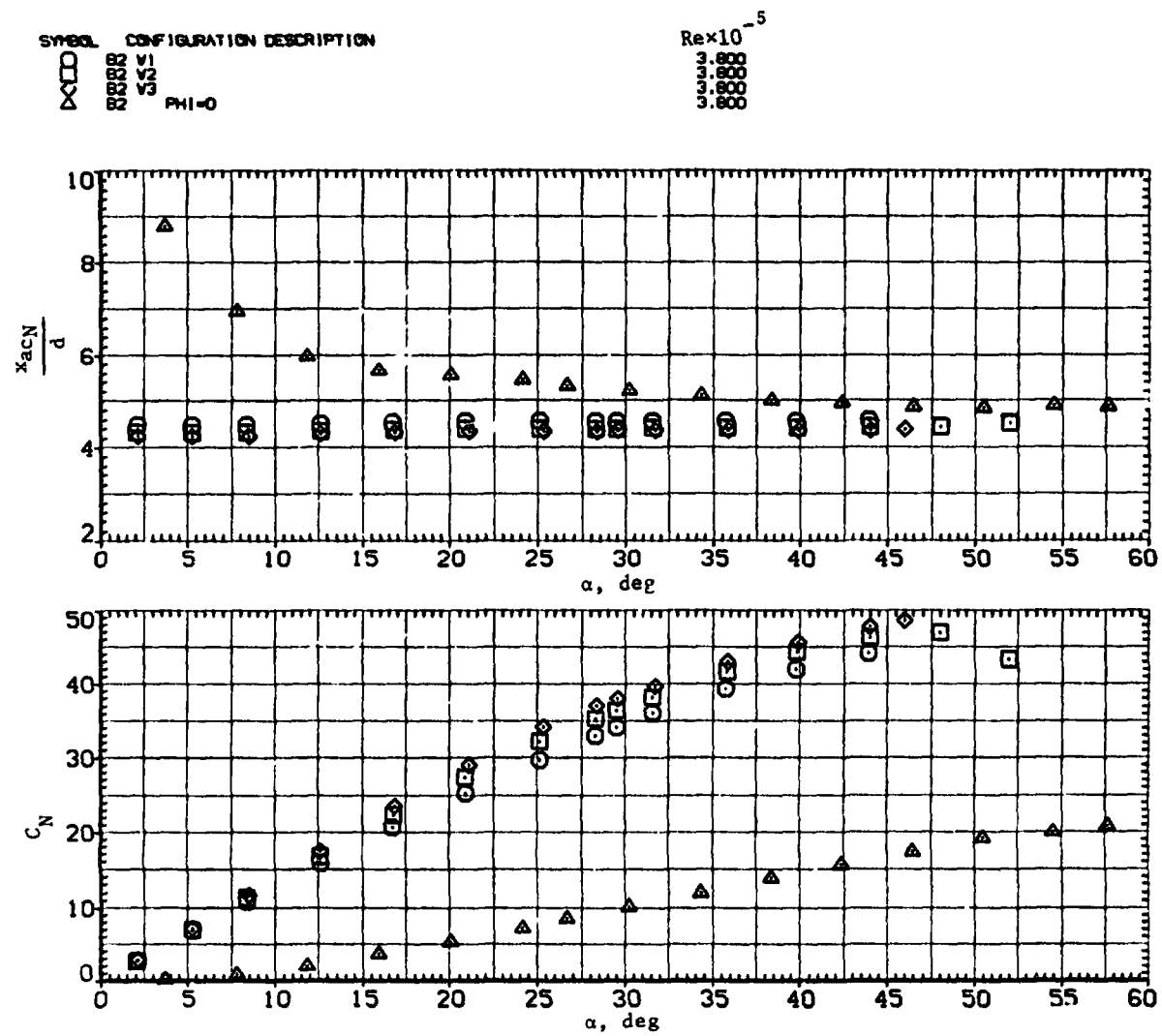
(c)  $C_A$  and  $C_n$  versus  $\alpha$ .

Figure 10.— Continued.



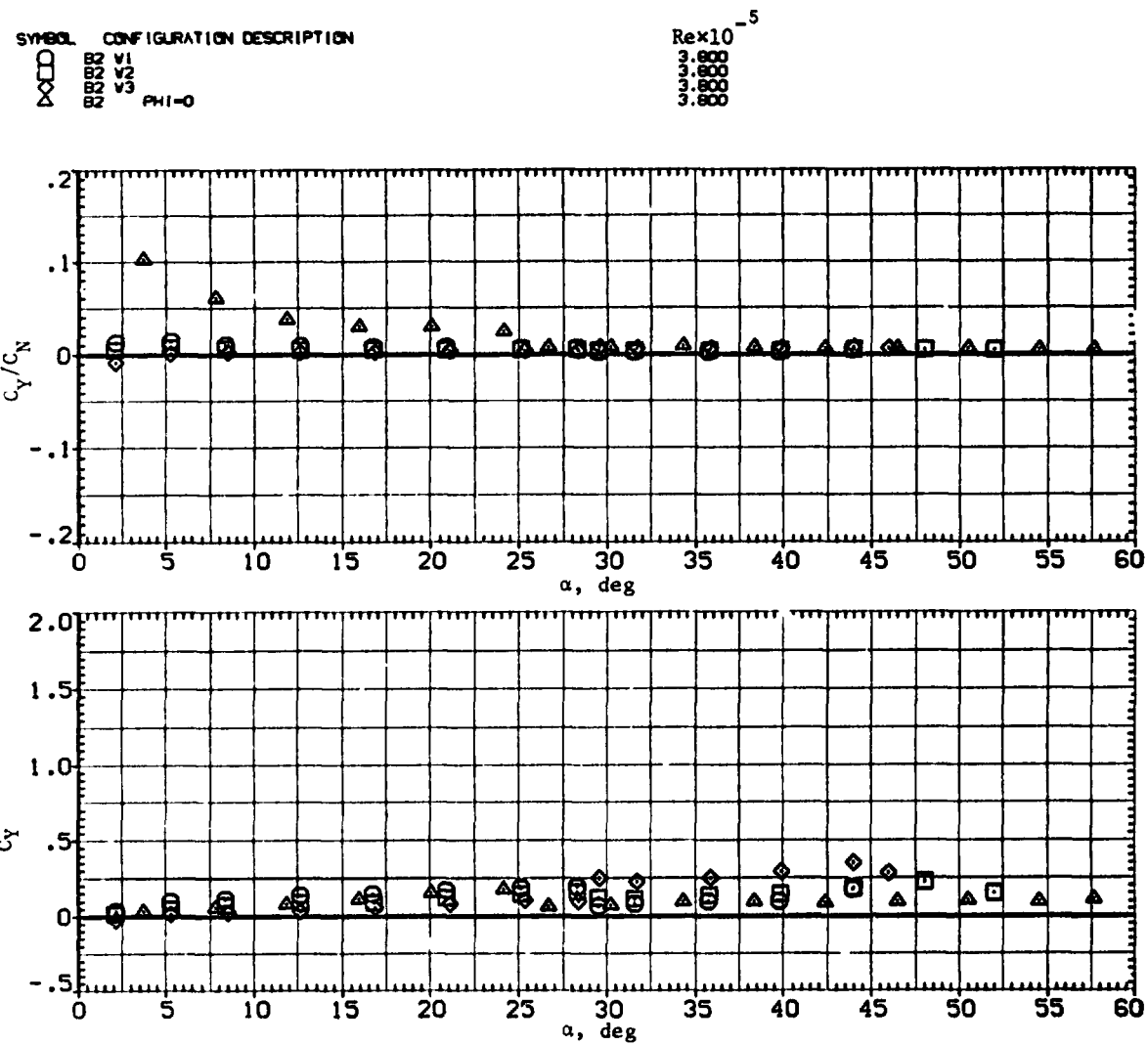
(d)  $C_L$  and  $L/D$  versus  $\alpha$ .

Figure 10.- Concluded.



(a)  $x_{acN}/d$  and  $C_N$  versus  $\alpha$ .

**Figure 11.— Effect of wing taper ratio with elliptic body;  $M = 1.5$ .**



(b)  $C_Y/C_N$  and  $C_Y$  versus  $\alpha$ .

Figure 11.— Continued.



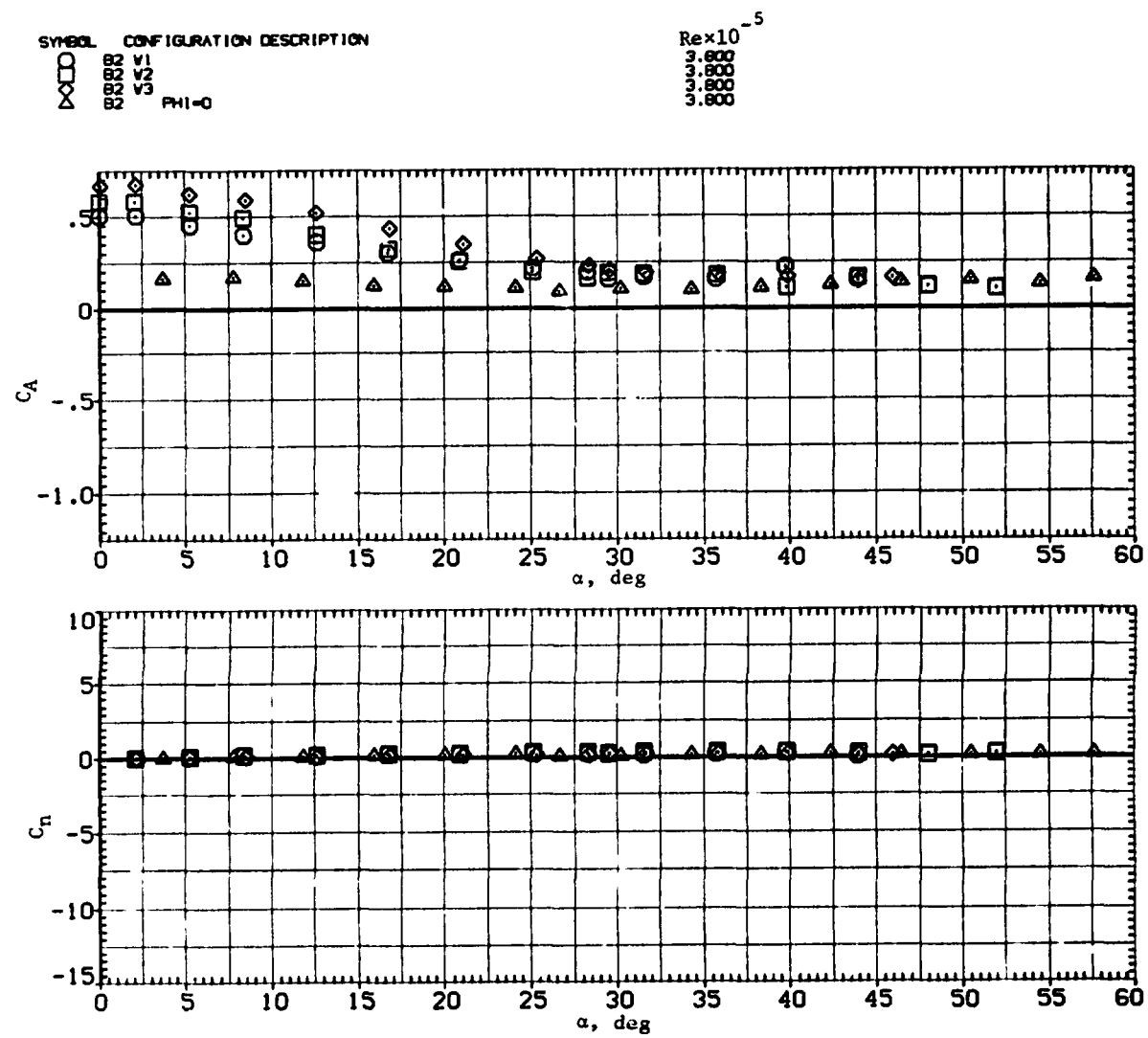
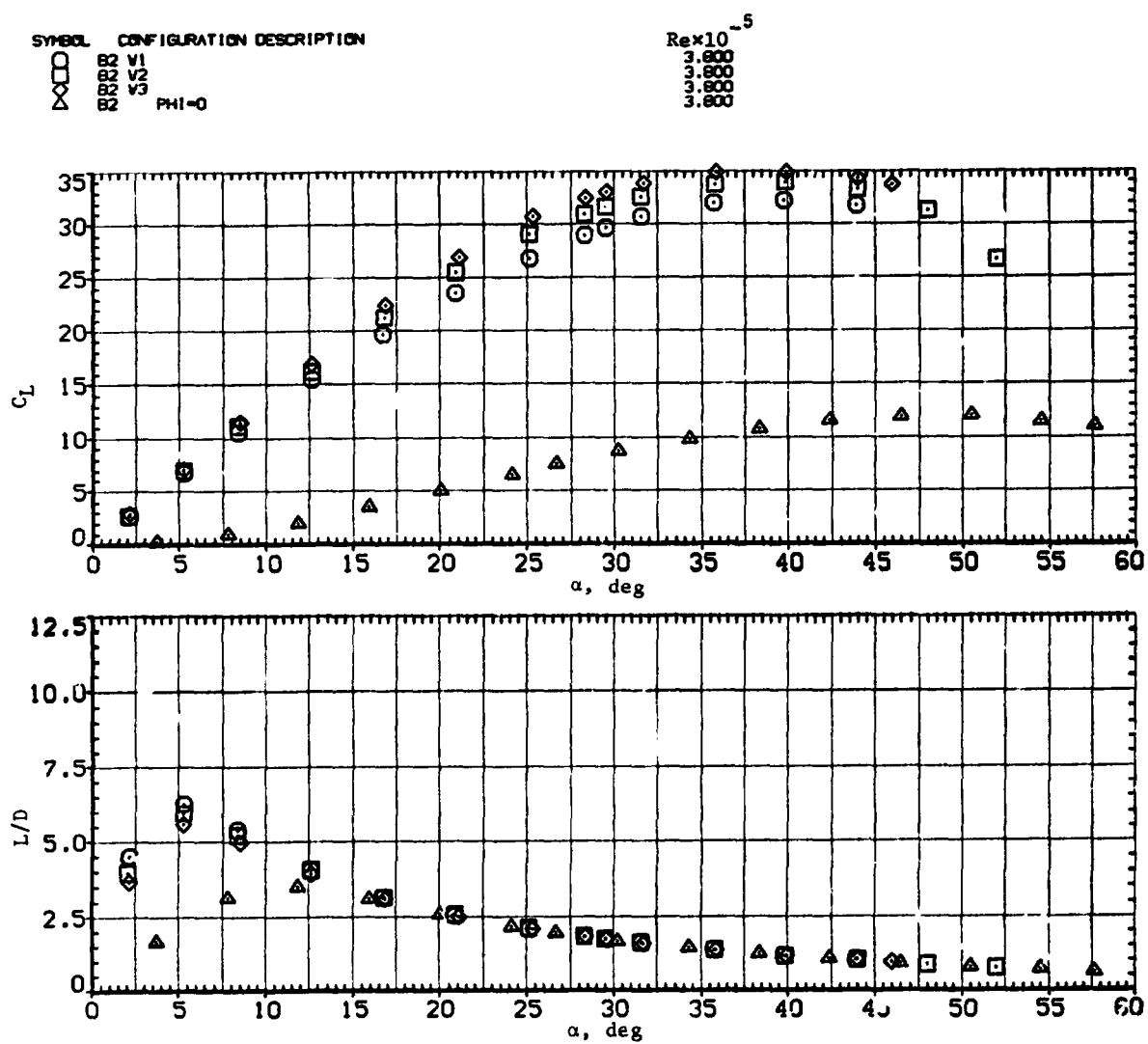
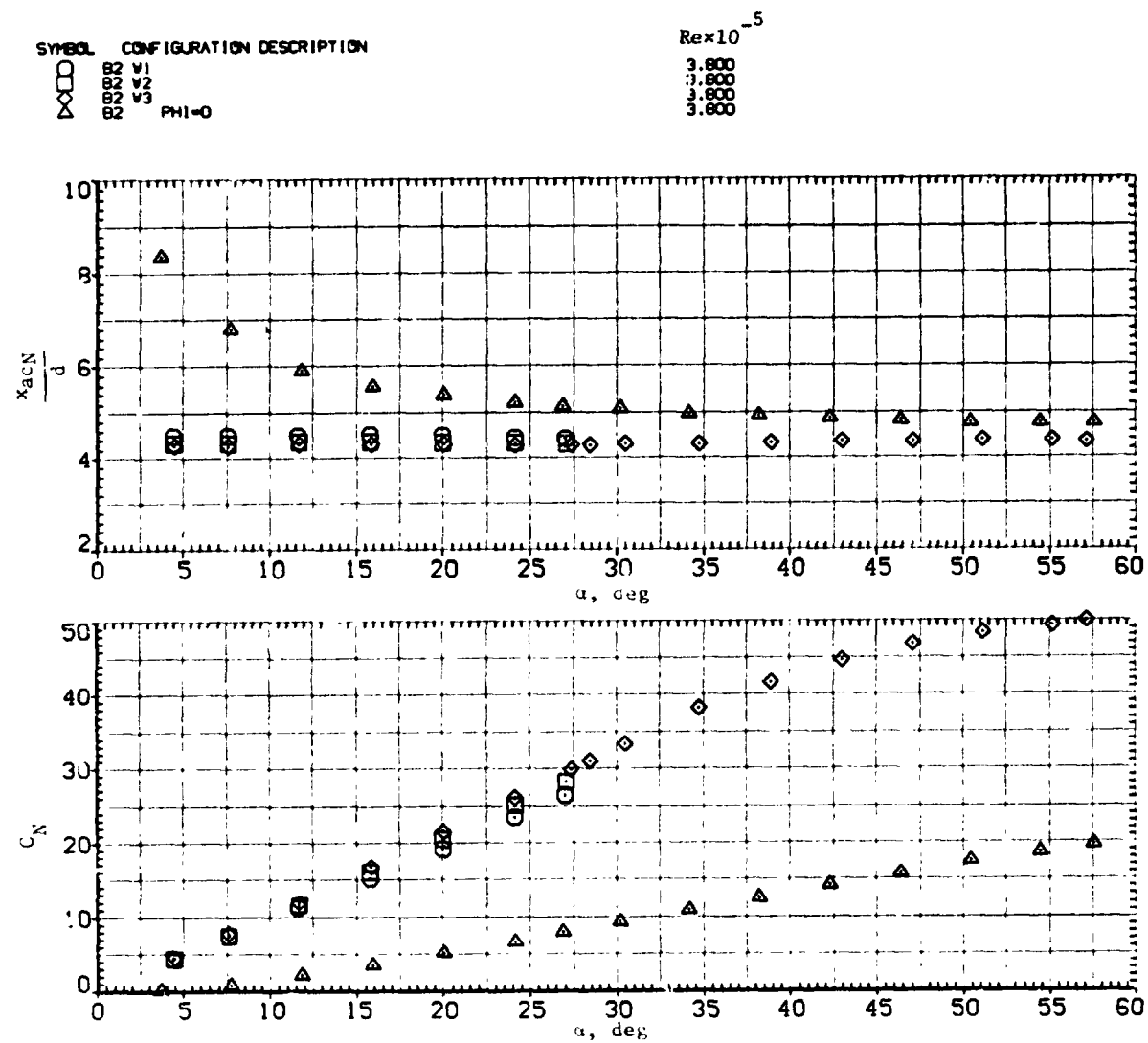
(c)  $C_A$  and  $C_n$  versus  $\alpha$ .

Figure 11.— Continued.



(d)  $C_L$  and  $L/D$  versus  $\alpha$ .

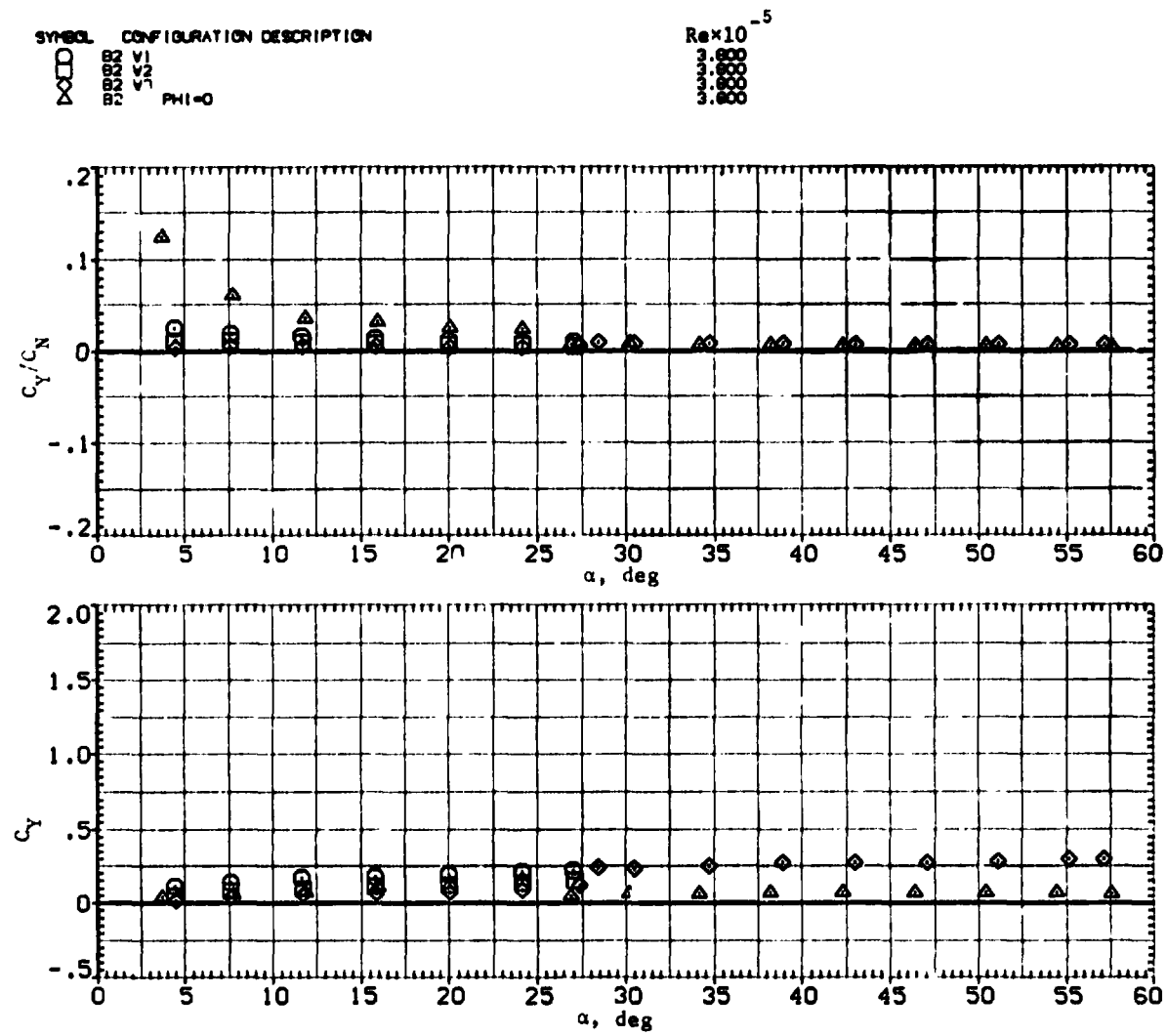
Figure 11.— Concluded.

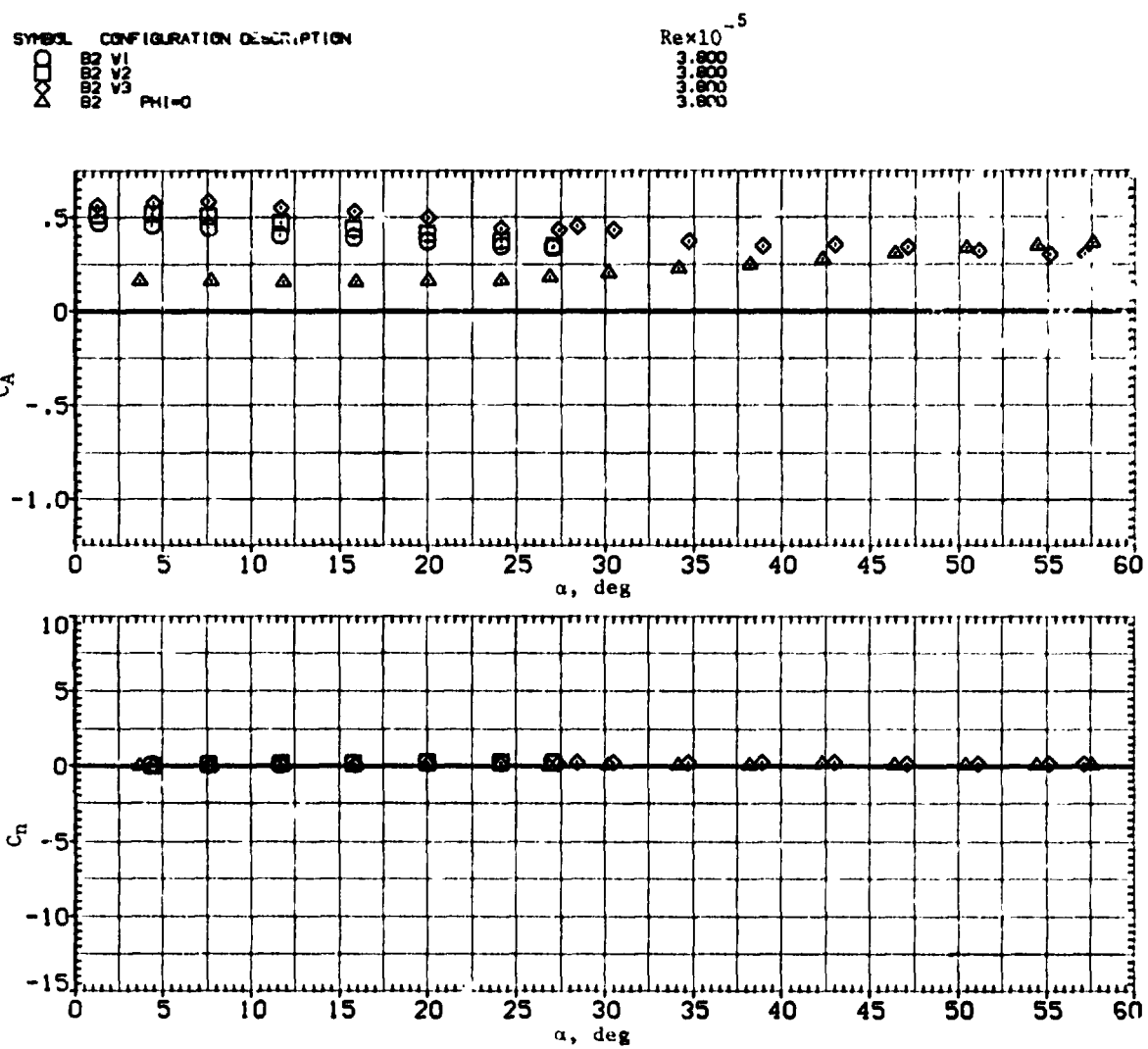


(a)  $x_{acN}/d$  and  $C_N$  versus  $\alpha$ .

Figure 12.- Effect of wing taper ratio with elliptic body:  $M = 2.0$ .

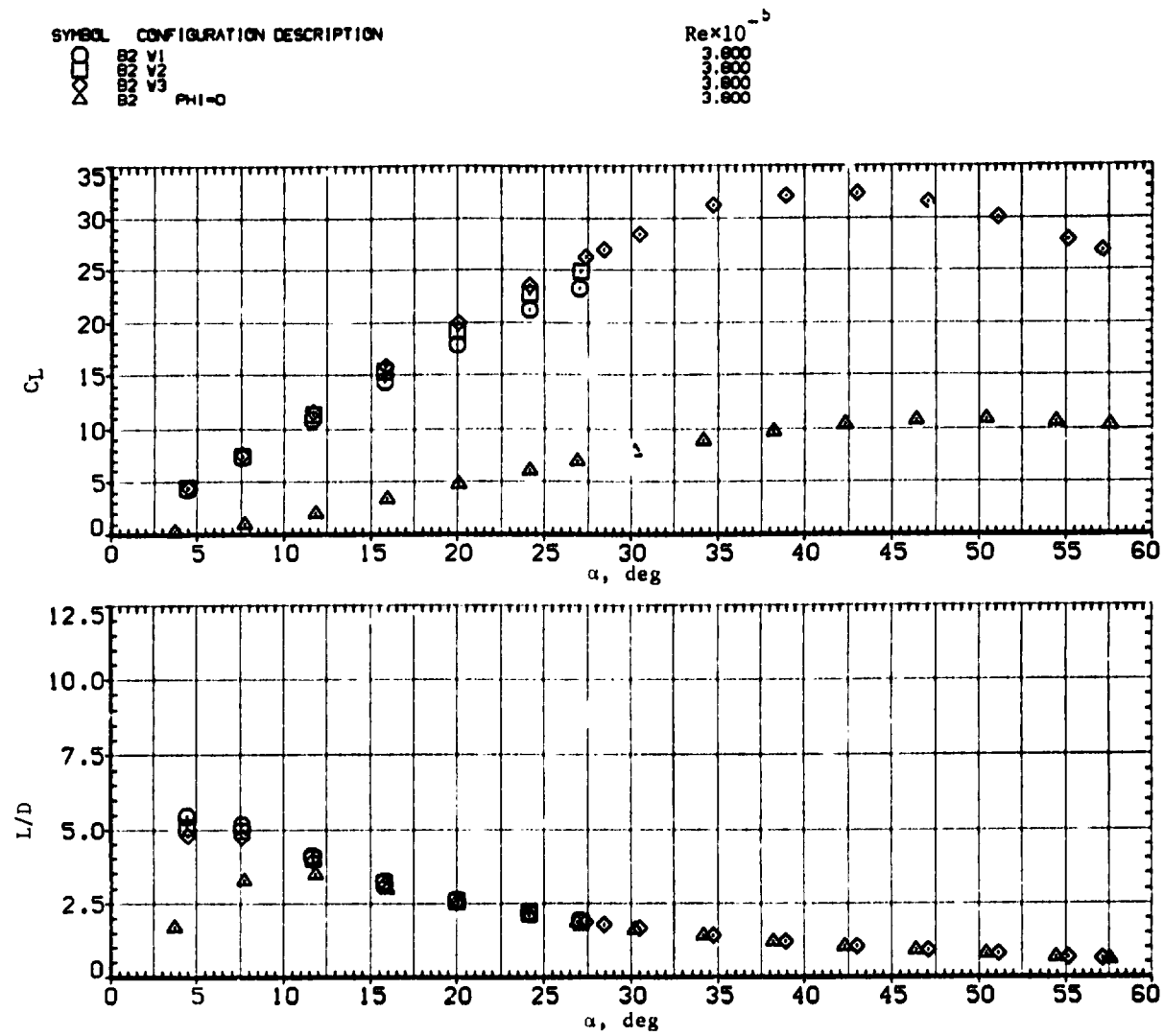
51





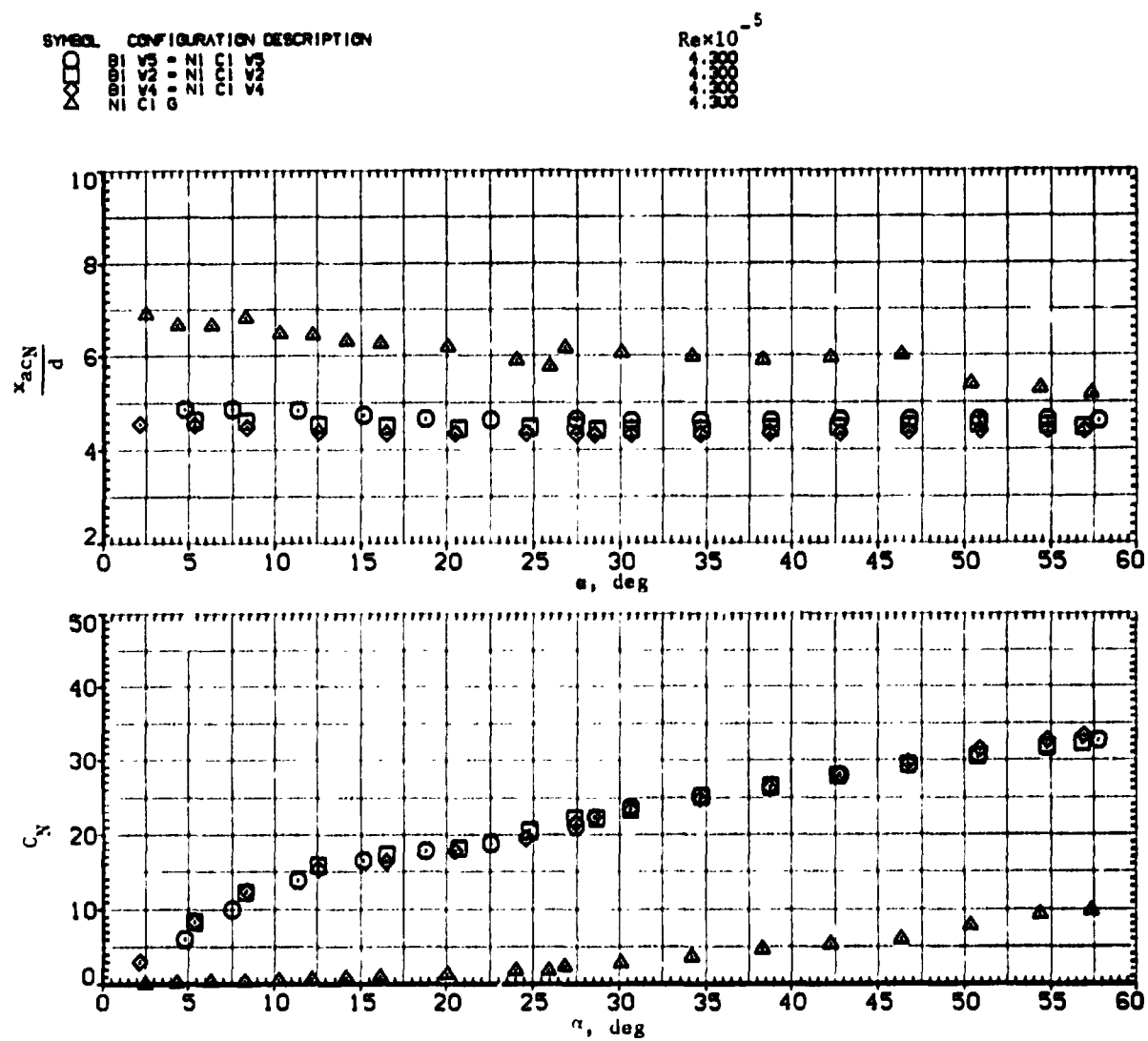
(c)  $C_A$  and  $C_n$  versus  $\alpha$ .

Figure 12.—Continued.



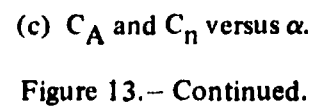
(d)  $C_L$  and  $L/D$  versus  $\alpha$ .

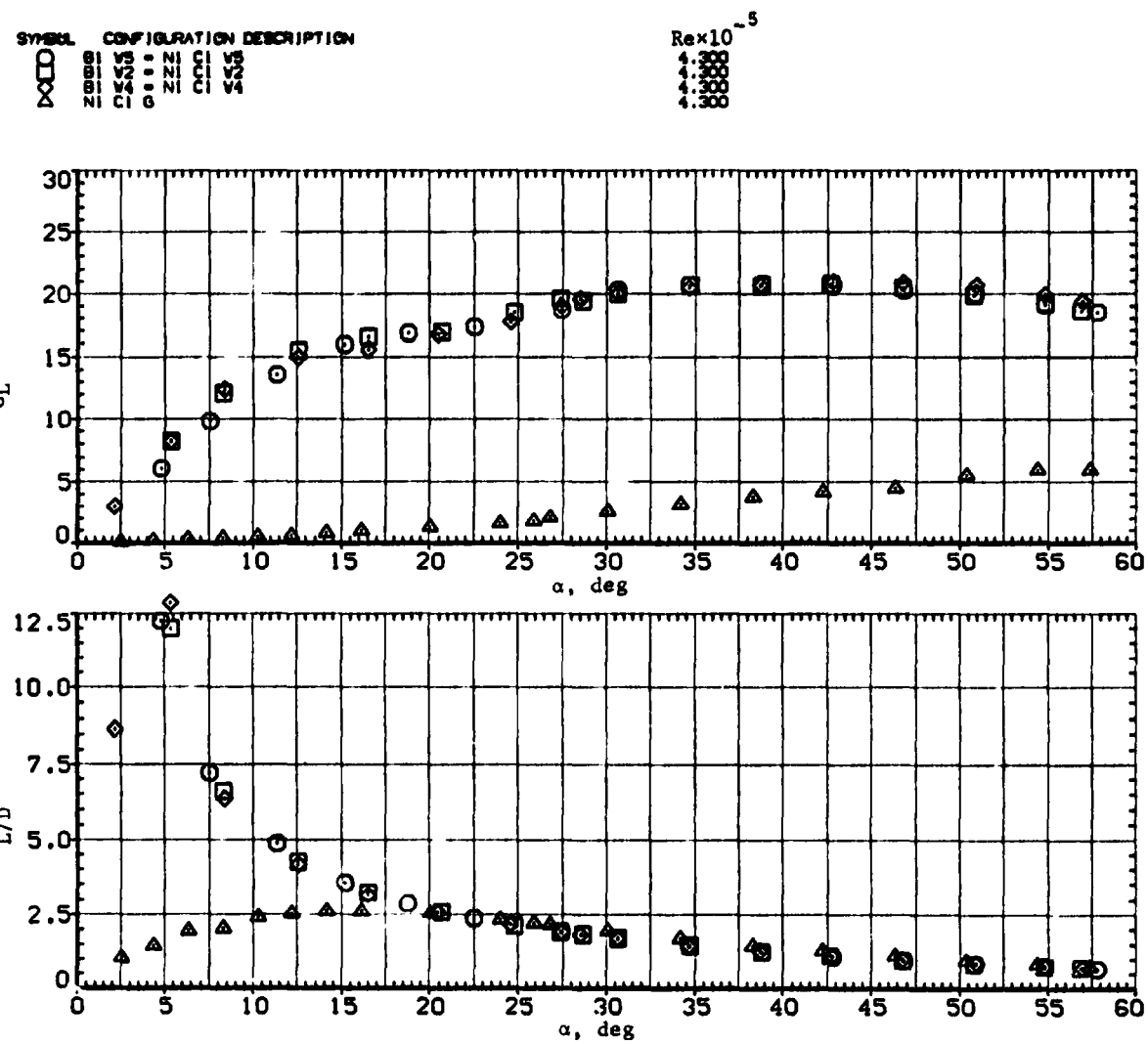
Figure 12.- Concluded.

(a)  $x_{acN}/d$  and  $C_N$  versus  $\alpha$ .Figure 13.— Effect of wing aspect ratio with circular body;  $M = 0.6$ .







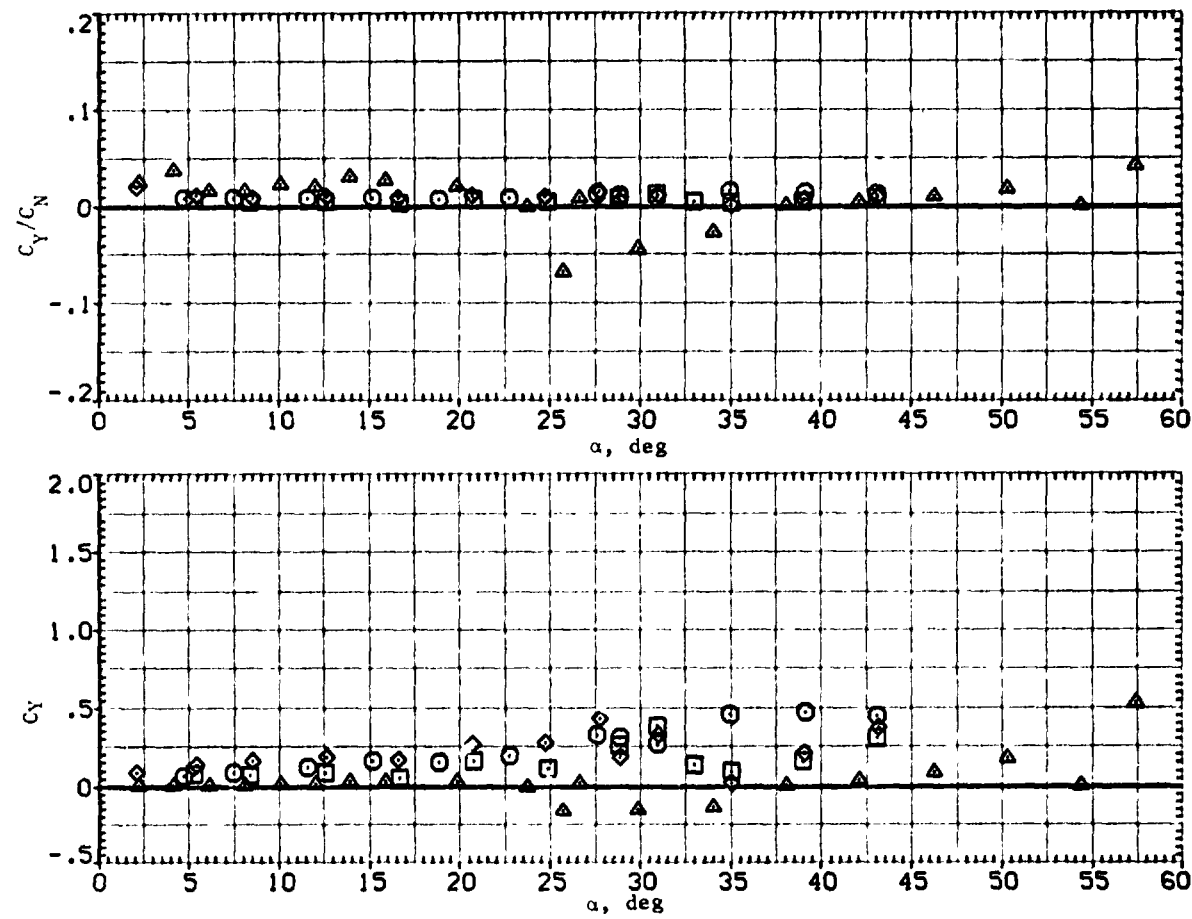


(d)  $C_L$  and  $L/D$  versus  $\alpha$ .

Figure 13.- Concluded.



SYMBOL	CONFIGURATION DESCRIPTION	$Re \times 10^{-5}$
$\square$	01 V3	4.300
$\circ$	01 V2	4.300
$\Delta$	01 V4	4.300
$\square$	01 V3	4.300
$\circ$	01 V2	4.300
$\Delta$	01 V4	4.300



(b)  $C_Y/C_N$  and  $C_Y$  versus  $\alpha$ .

Figure 14.- Continued.

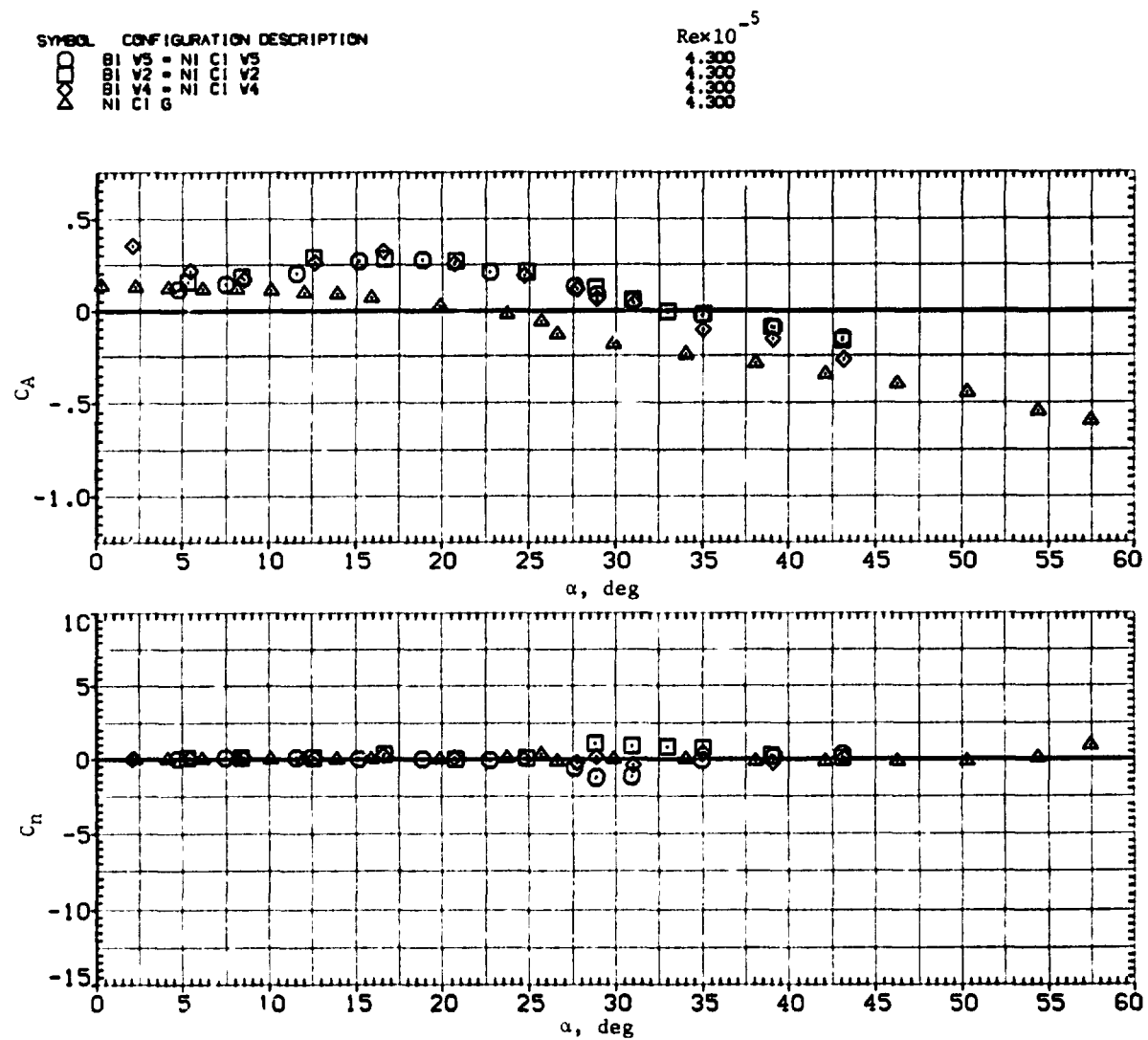
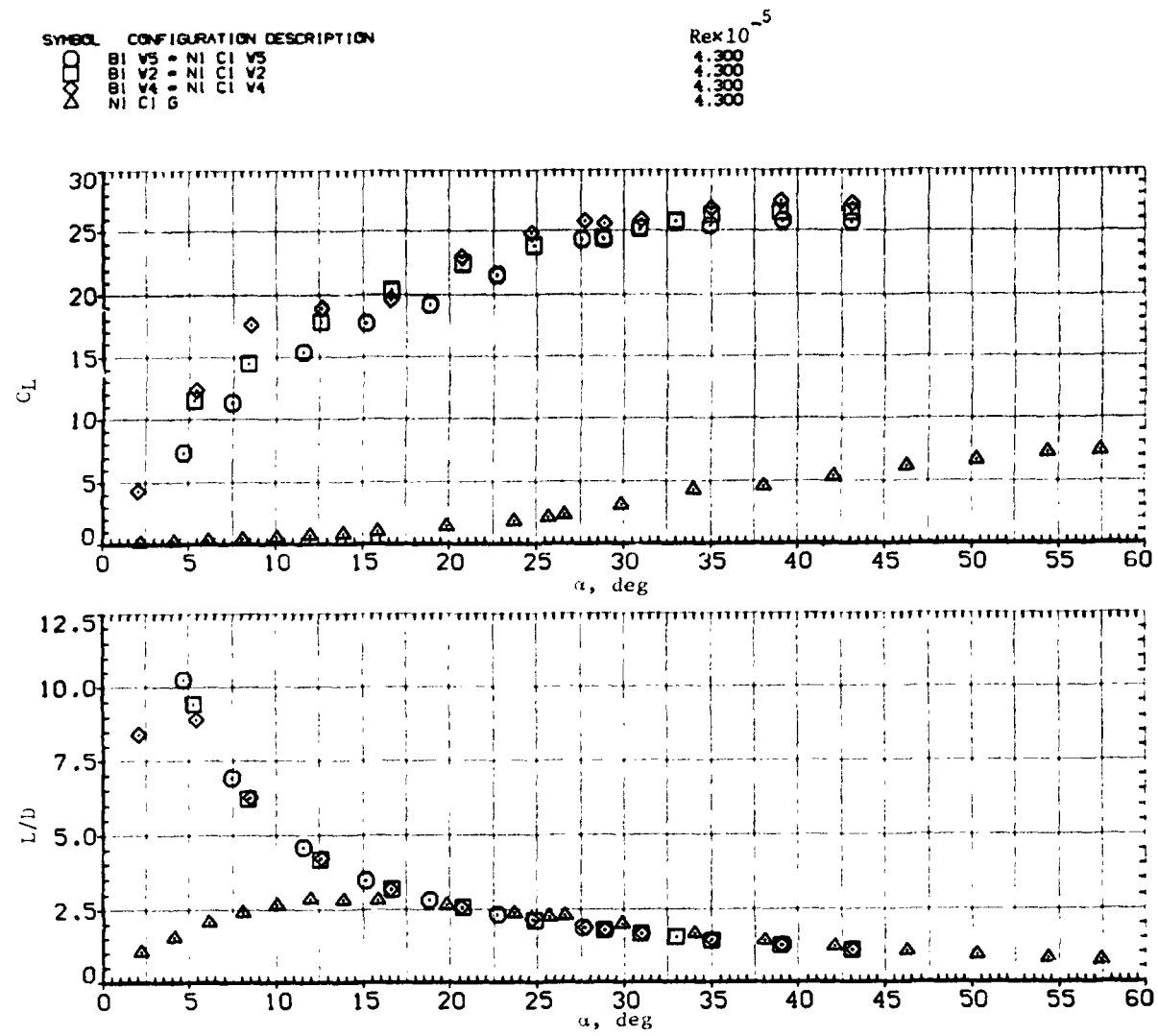
(c)  $C_A$  and  $C_n$  versus  $\alpha$ .

Figure 14. - Continued.



(d)  $C_L$  and  $L/D$  versus  $\alpha$ .

Figure 14.-- Concluded.

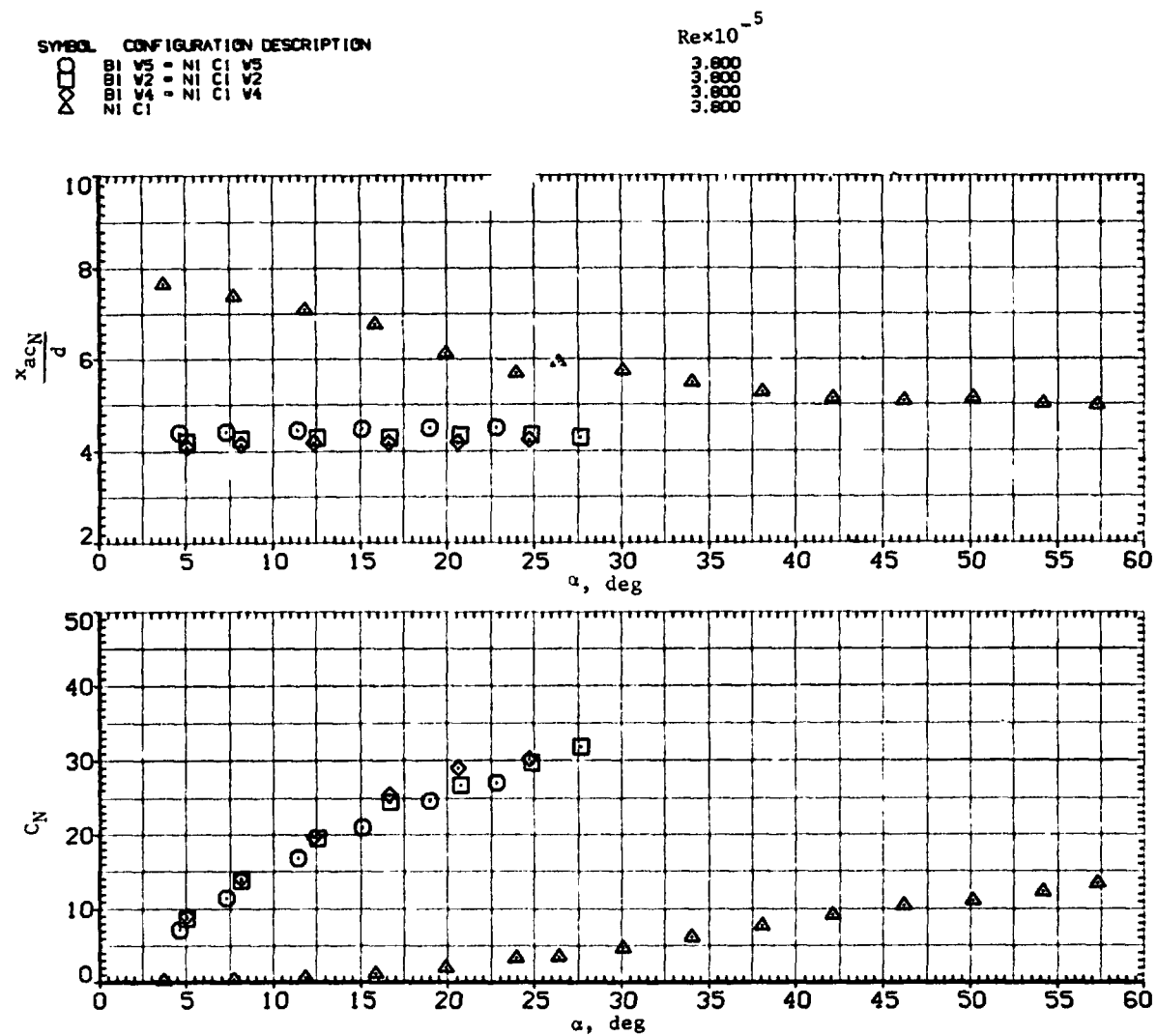
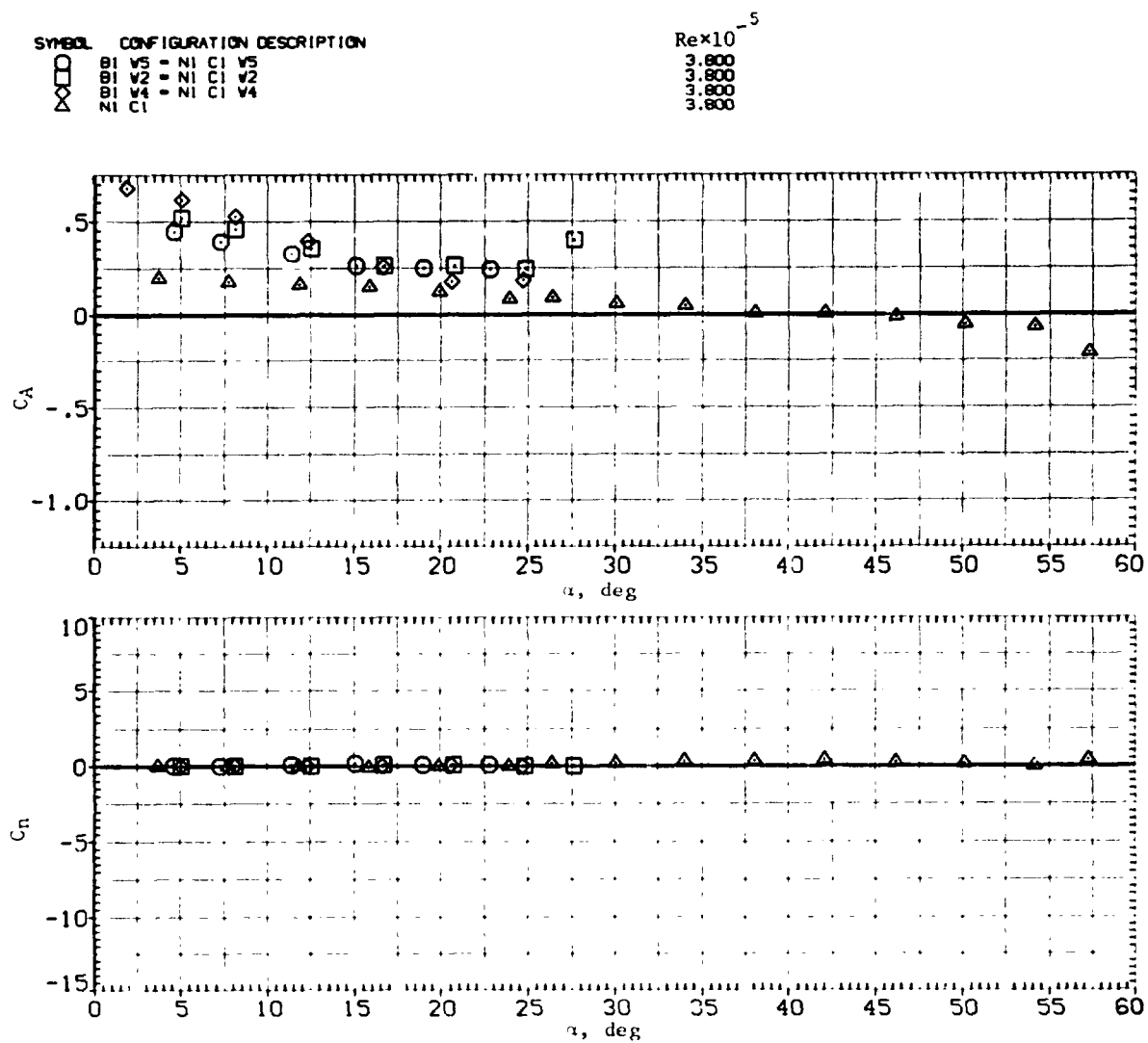
(a)  $x_{acN}/d$  and  $C_N$  versus  $\alpha$ .Figure 15.— Effect of wing aspect ratio with circular body;  $M = 1.2$ .

Figure 1 consists of two vertically stacked plots. The top plot shows the ratio  $C_Y/C_N$  on the y-axis (ranging from -0.2 to 0.2) versus the angle  $\alpha$  in degrees on the x-axis (ranging from 0 to 60). The data points, represented by various symbols (circles, squares, triangles), are clustered around the zero line, with some scatter at lower  $\alpha$  values. The bottom plot shows the coefficient  $C_Y$  on the y-axis (ranging from -0.5 to 2.0) versus the angle  $\alpha$  in degrees on the x-axis (ranging from 0 to 60). The data points are clustered around the zero line, with some scatter at lower  $\alpha$  values.

Figure 15.—Continued.

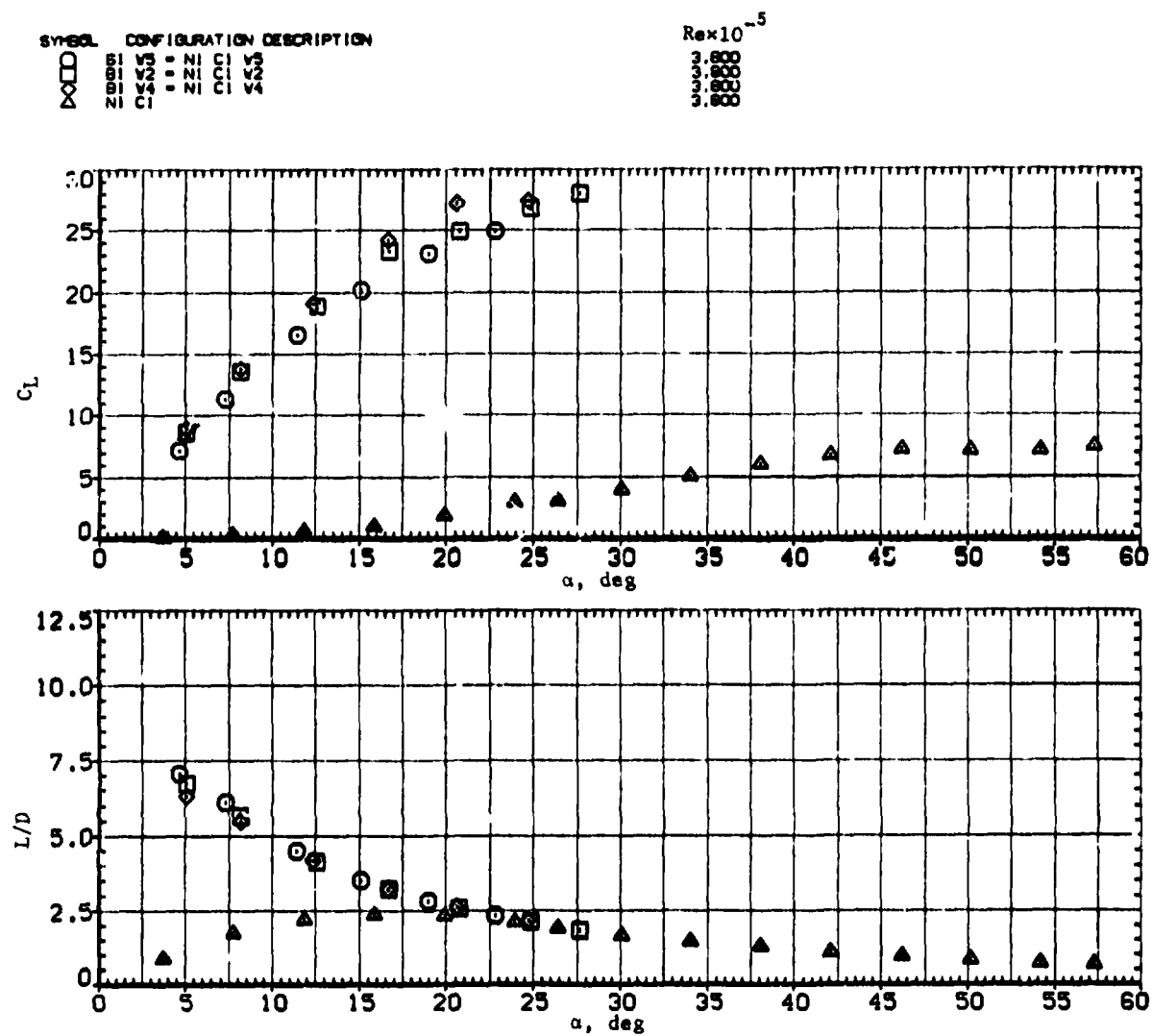




(c)  $C_A$  and  $C_N$  versus  $\alpha$ .

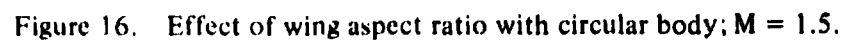
Figure 15.  $C_A$  and  $C_N$  versus  $\alpha$ .

REPRODUCIBILITY OF THE  
ORIGINAL PAGE IS POOR



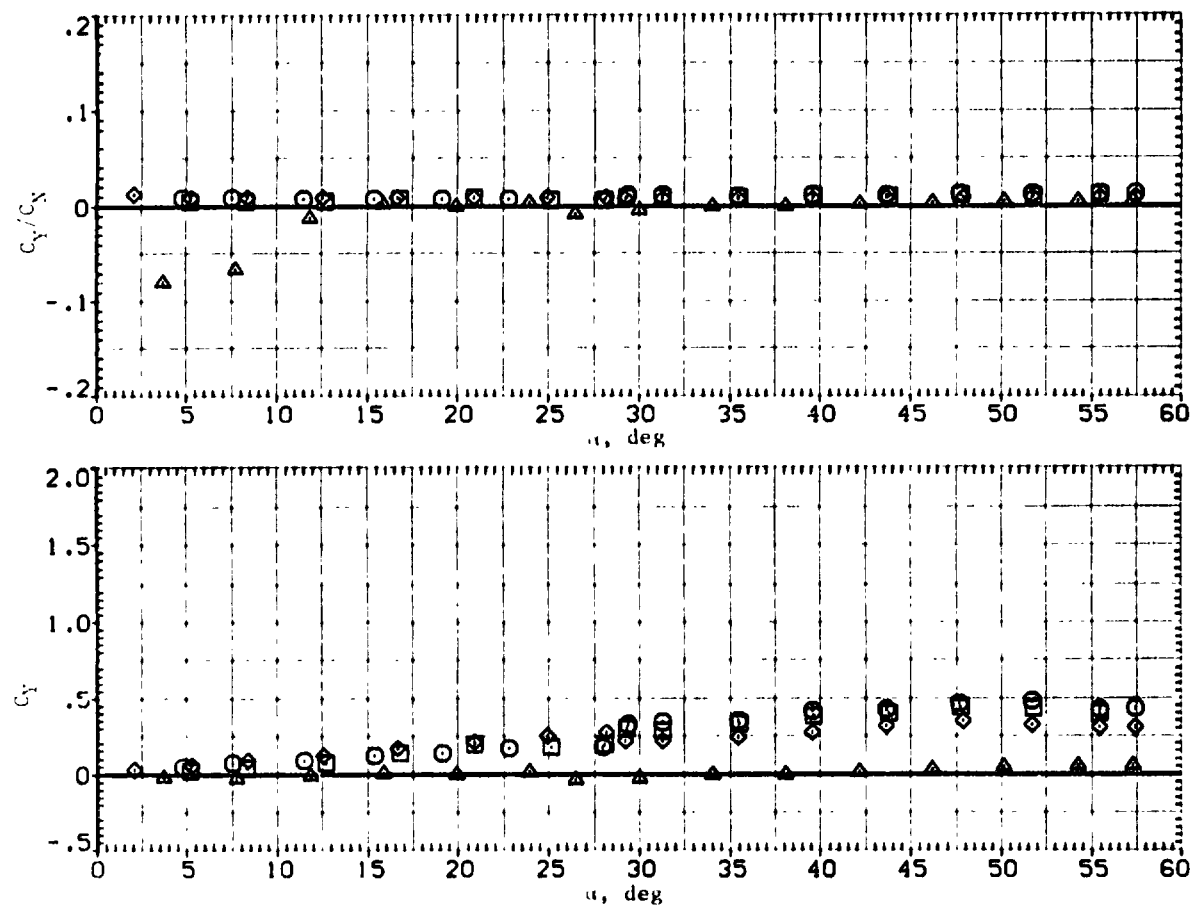
(d)  $C_L$  and  $L/D$  versus  $\alpha$ .

Figure 15.- Concluded.



**Figure 16. Effect of wing aspect ratio with circular body;  $M = 1.5$ .**

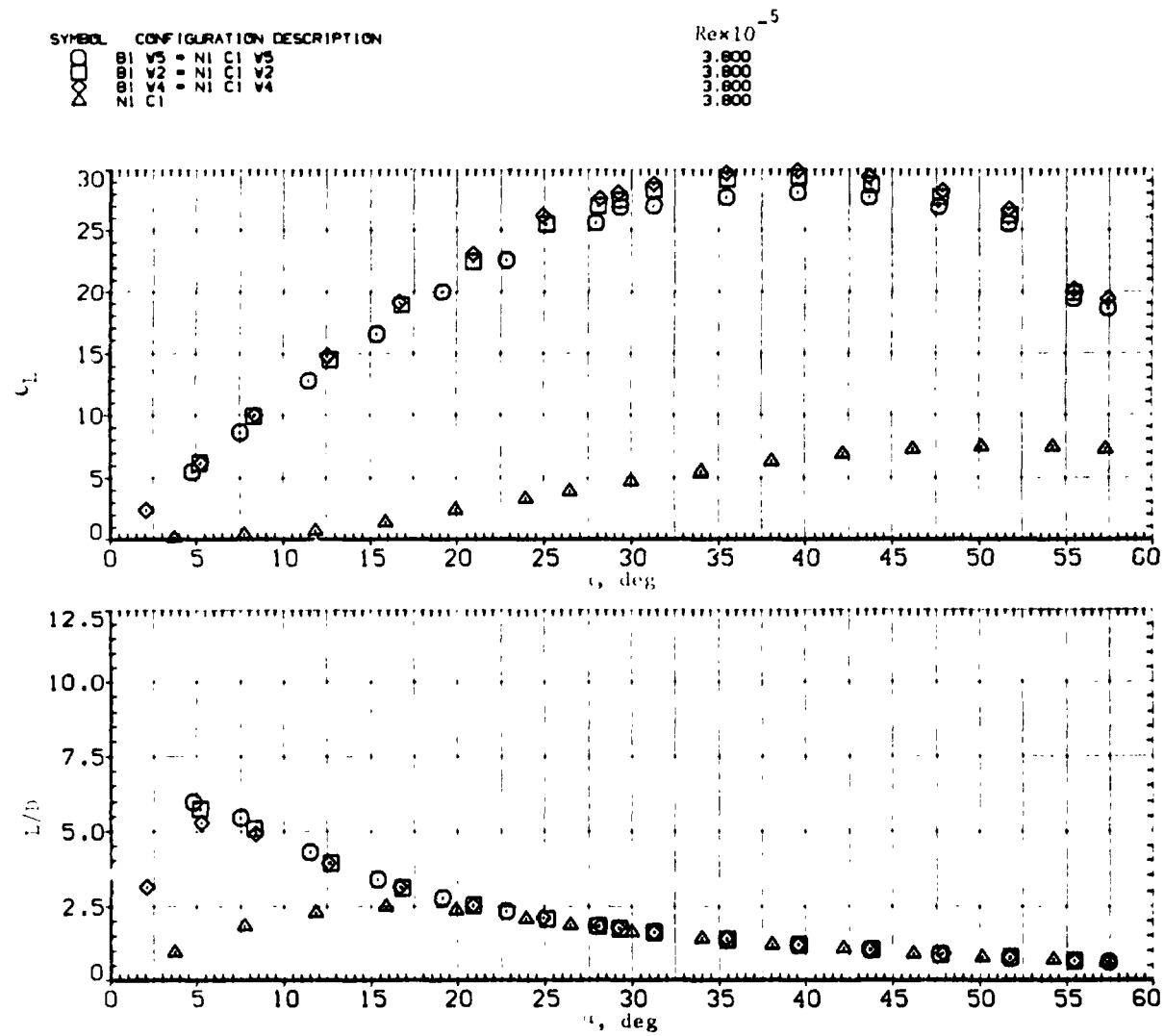
SYMBOL	CONFIGURATION DESCRIPTION	$Re \times 10^{-5}$
$\square$	55 = N1 C1 55	3.800
$\circ$	55 = N1 C1 55	3.800
$\triangle$	55 = N1 C1 55	3.800
$\times$	55 = N1 C1 55	3.800
$\square$	55 = N1 C1 55	3.800
$\circ$	55 = N1 C1 55	3.800
$\triangle$	55 = N1 C1 55	3.800
$\times$	55 = N1 C1 55	3.800



(b)  $C_Y/C_N$  and  $C_Y$  versus  $\alpha$ .

Figure 16. - Continue.





(d)  $C_L$  and  $L/D$  versus  $\alpha$ .

Figure 16. Concluded.

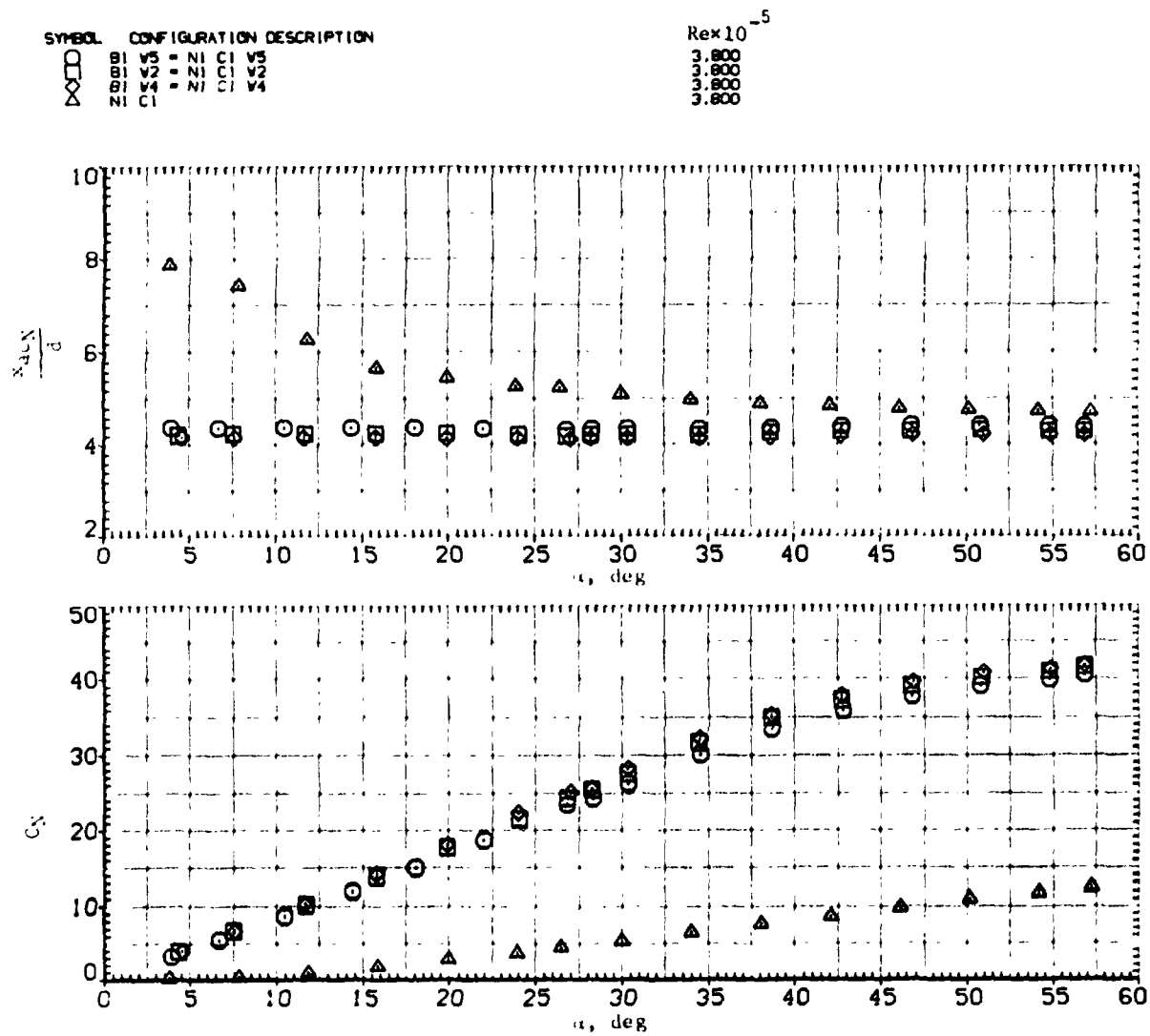
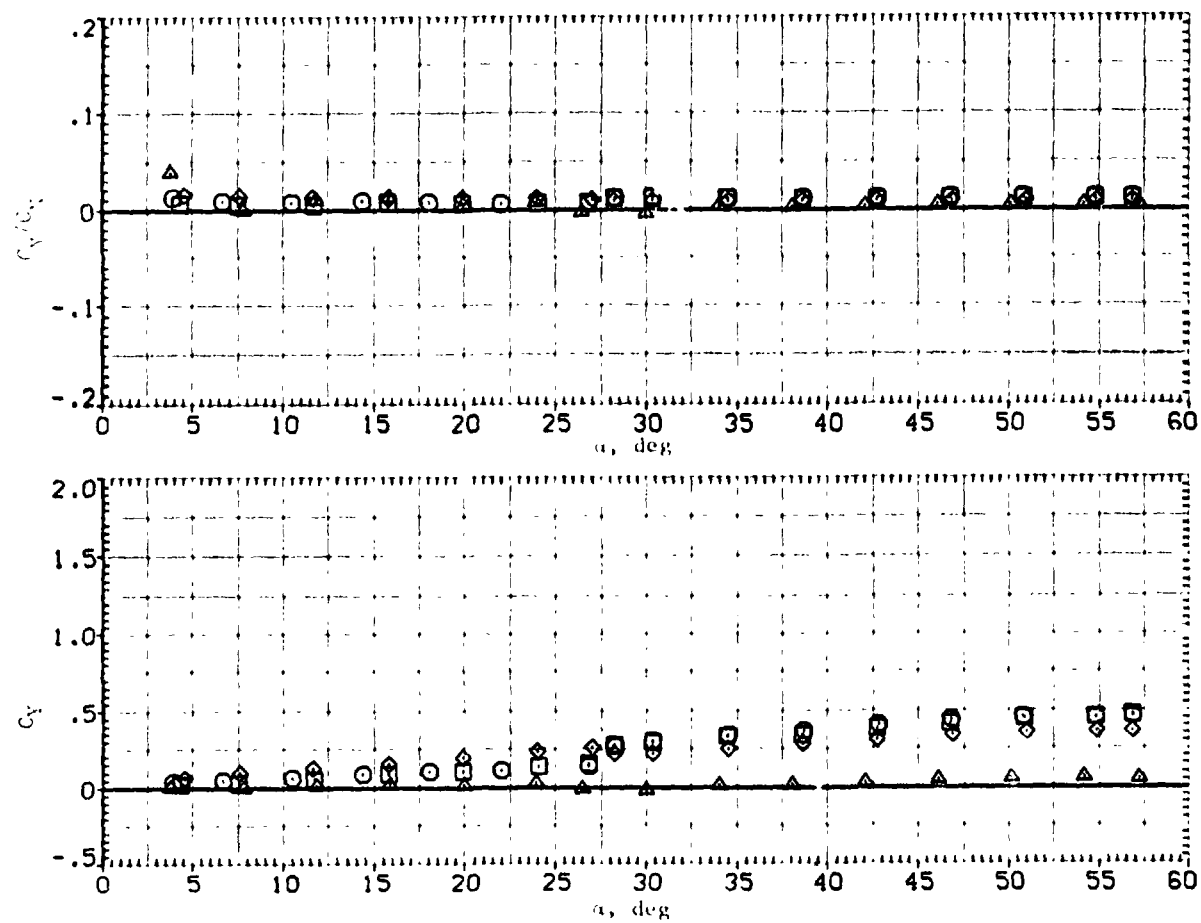


Figure 17.-- Effect of wing aspect ratio with circular body;  $M = 2.0$ .

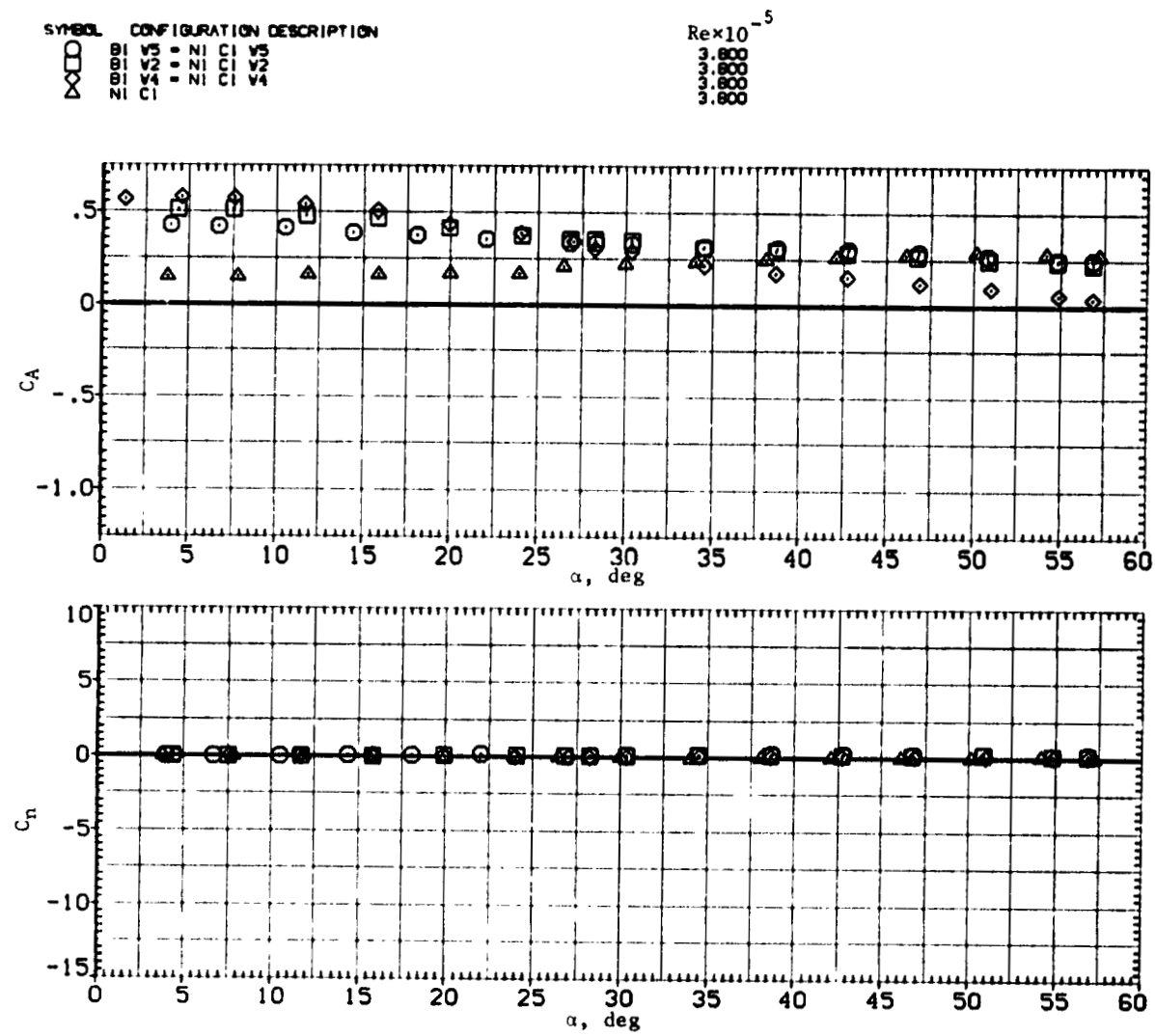
SYMBOL	CONFIGURATION DESCRIPTION	$Re \times 10^{-5}$
$\square$	B1 V5 = N1 C1 V5	3.600
$\circ$	B1 V3 = N1 C1 V3	3.600
$\triangle$	B1 V4 = N1 C1 V4	3.600
$\times$	N1 C1	3.600



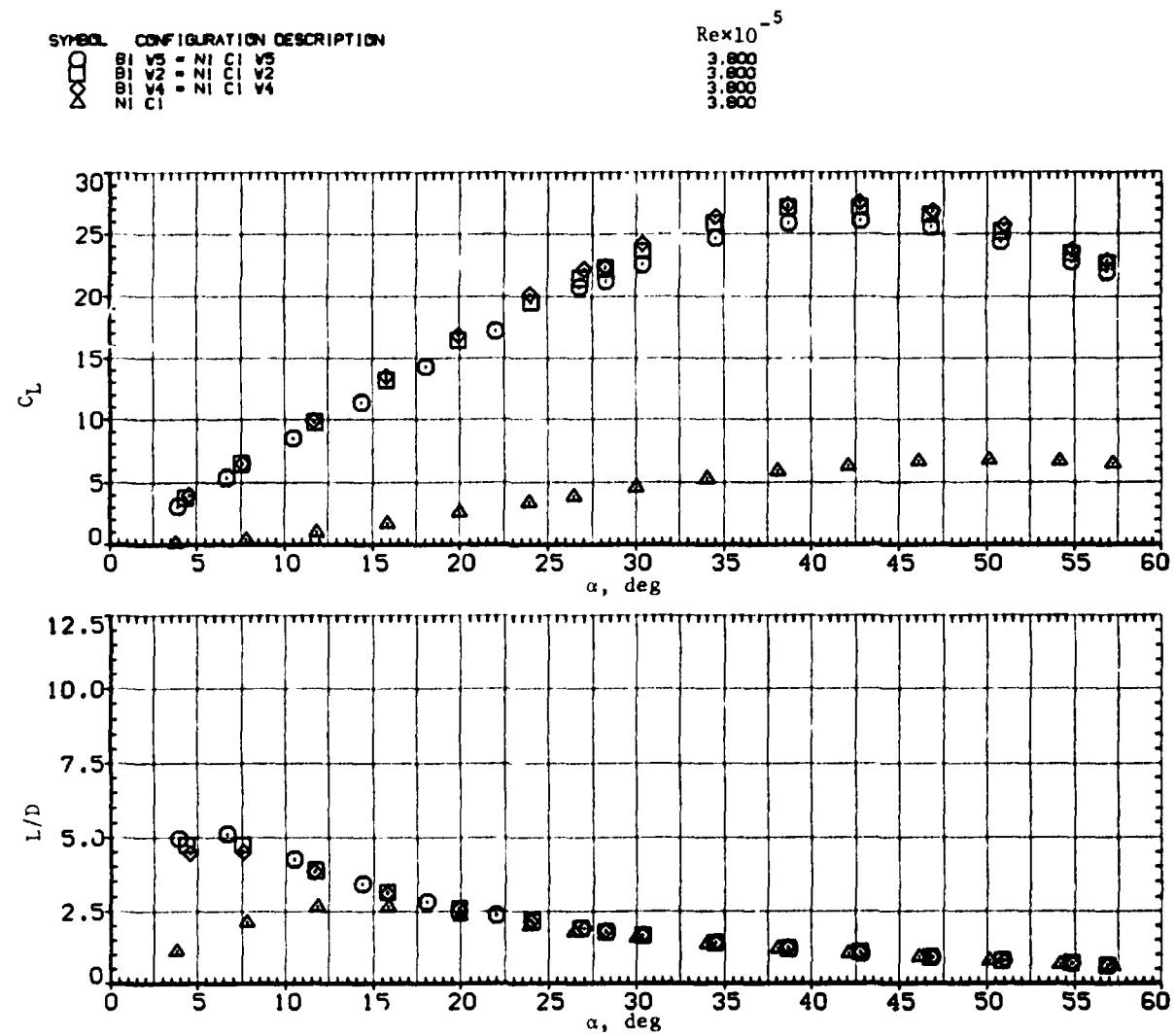
(b)  $C_Y/C_N$  and  $C_Y$  versus  $\alpha$ .

Figure 17.— Continued.





(c)  $C_A$  and  $C_n$  versus  $\alpha$ .



(d)  $C_L$  and  $L/D$  versus  $\alpha$ .

Figure 17.- Concluded.

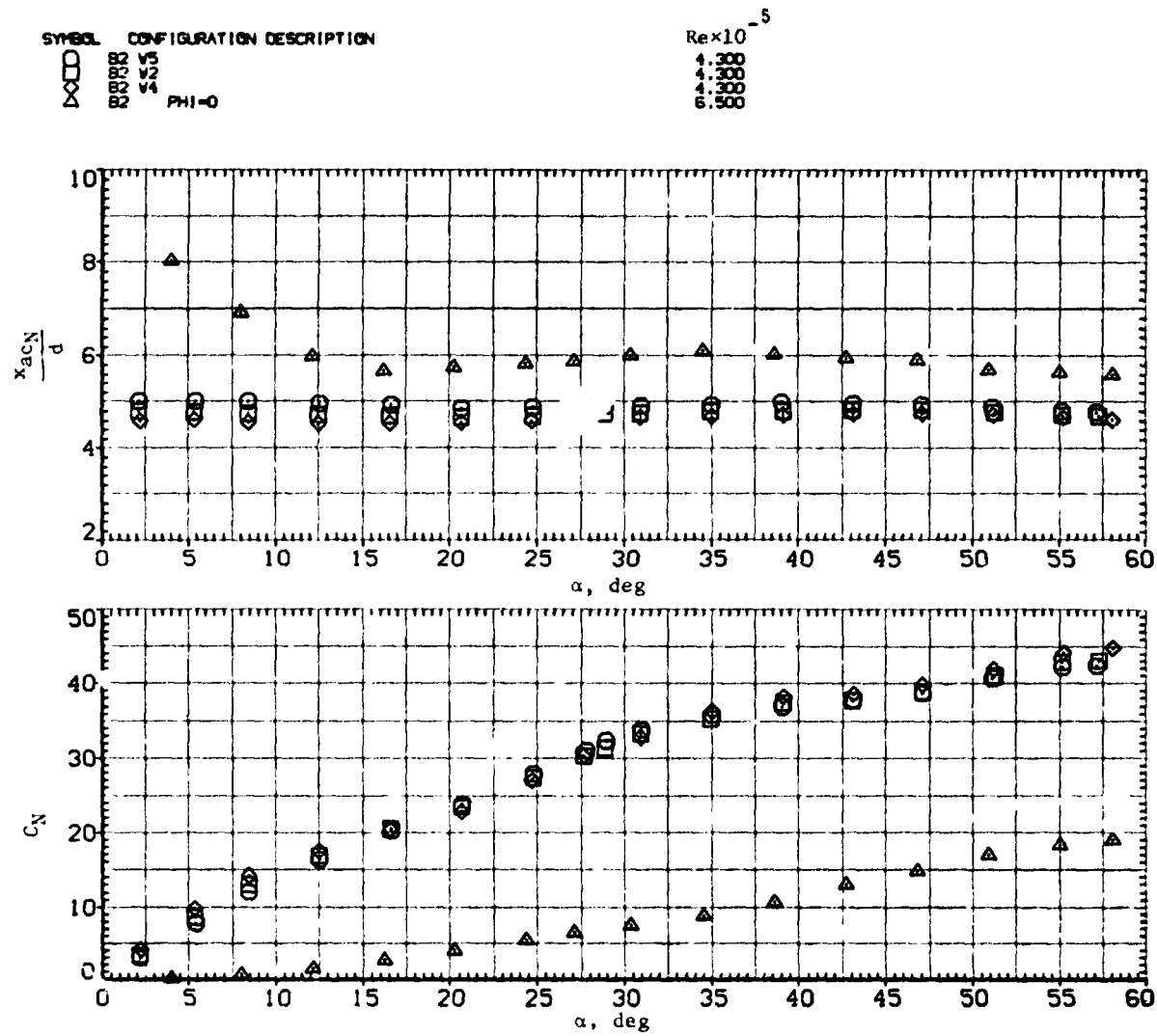
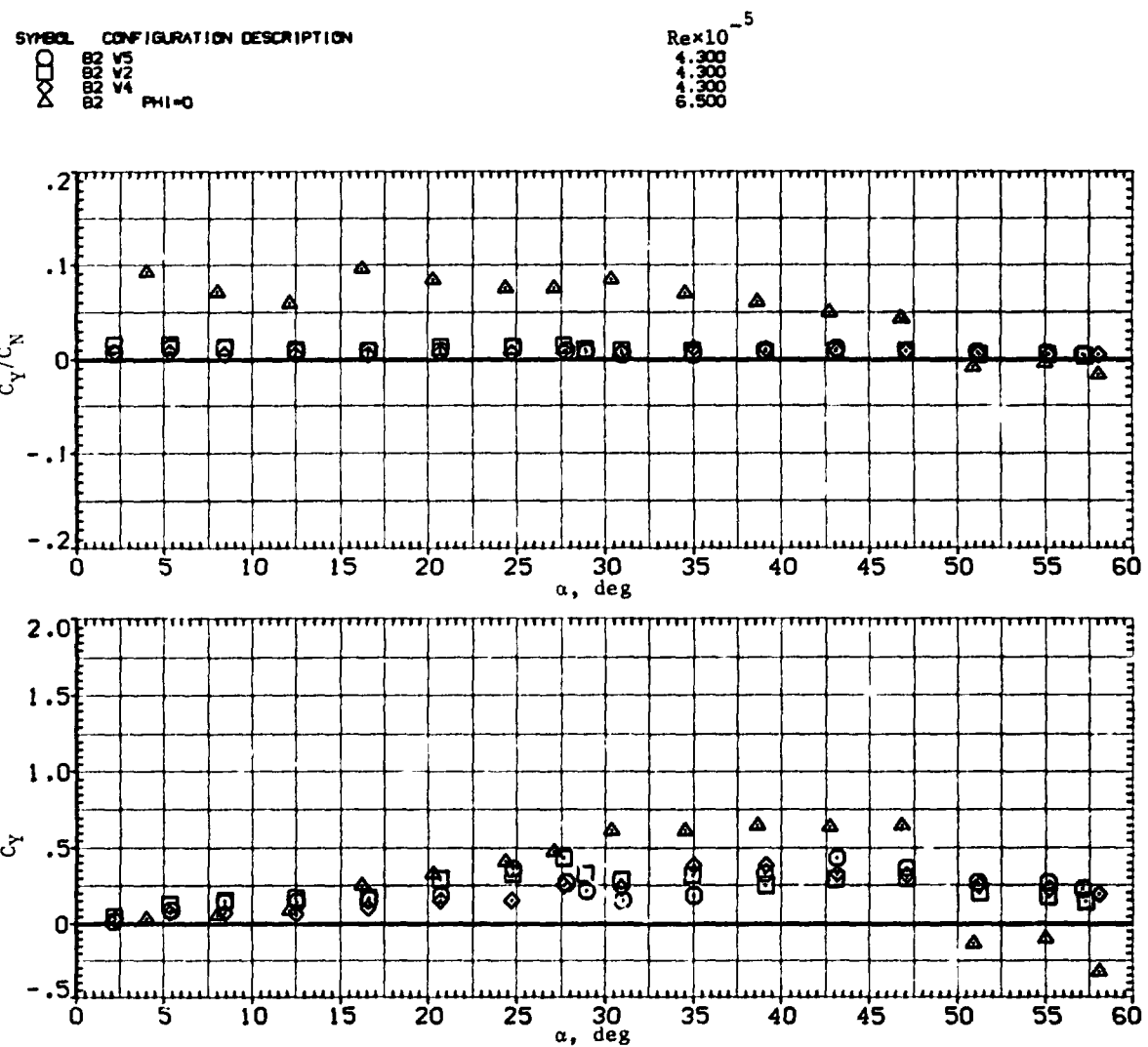


Figure 18.- Effect of wing aspect ratio with elliptic body;  $M = 0.6$ .



(b)  $C_Y/C_N$  and  $C_Y$  versus  $\alpha$ .

Figure 18.— Continued.

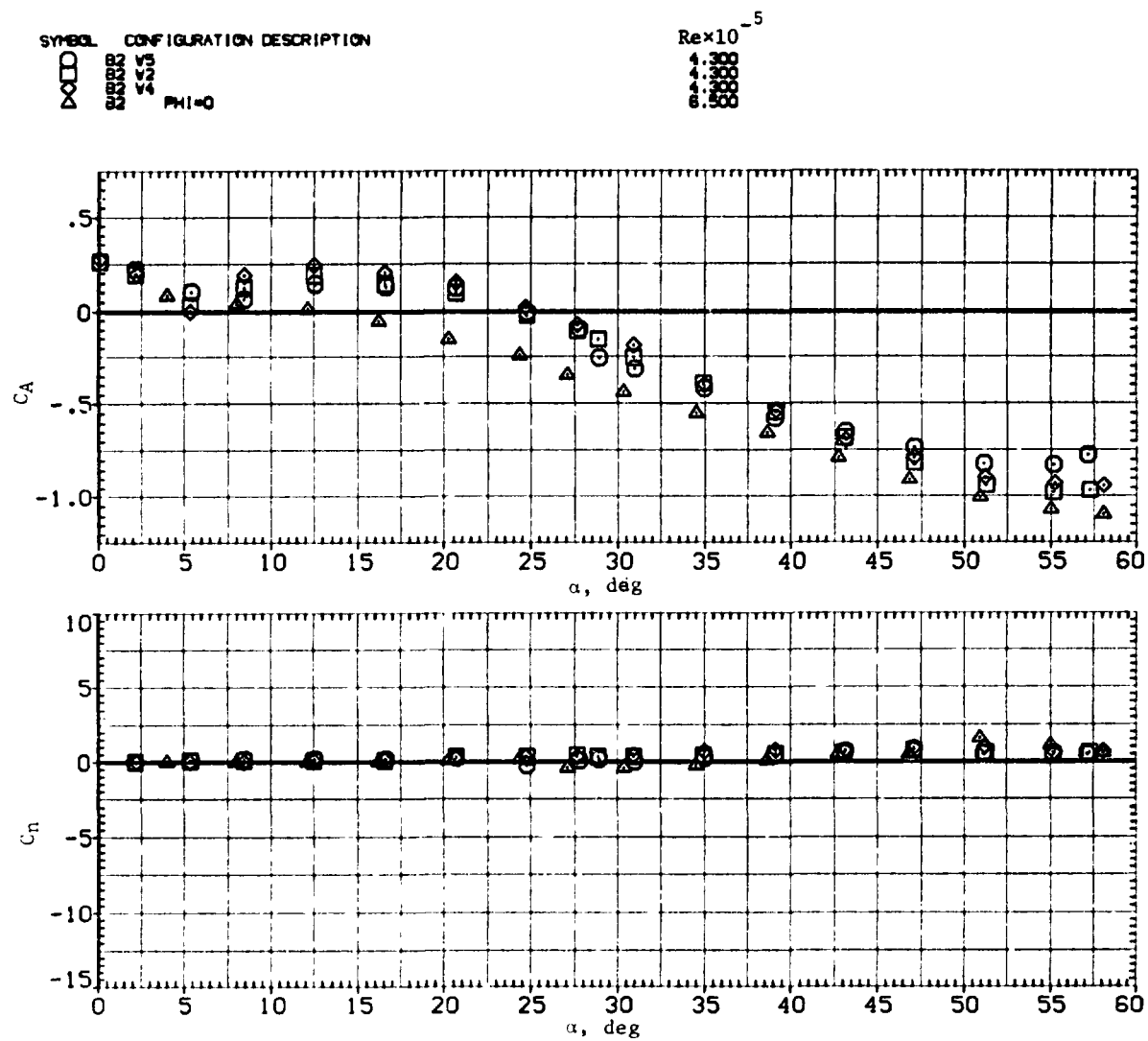
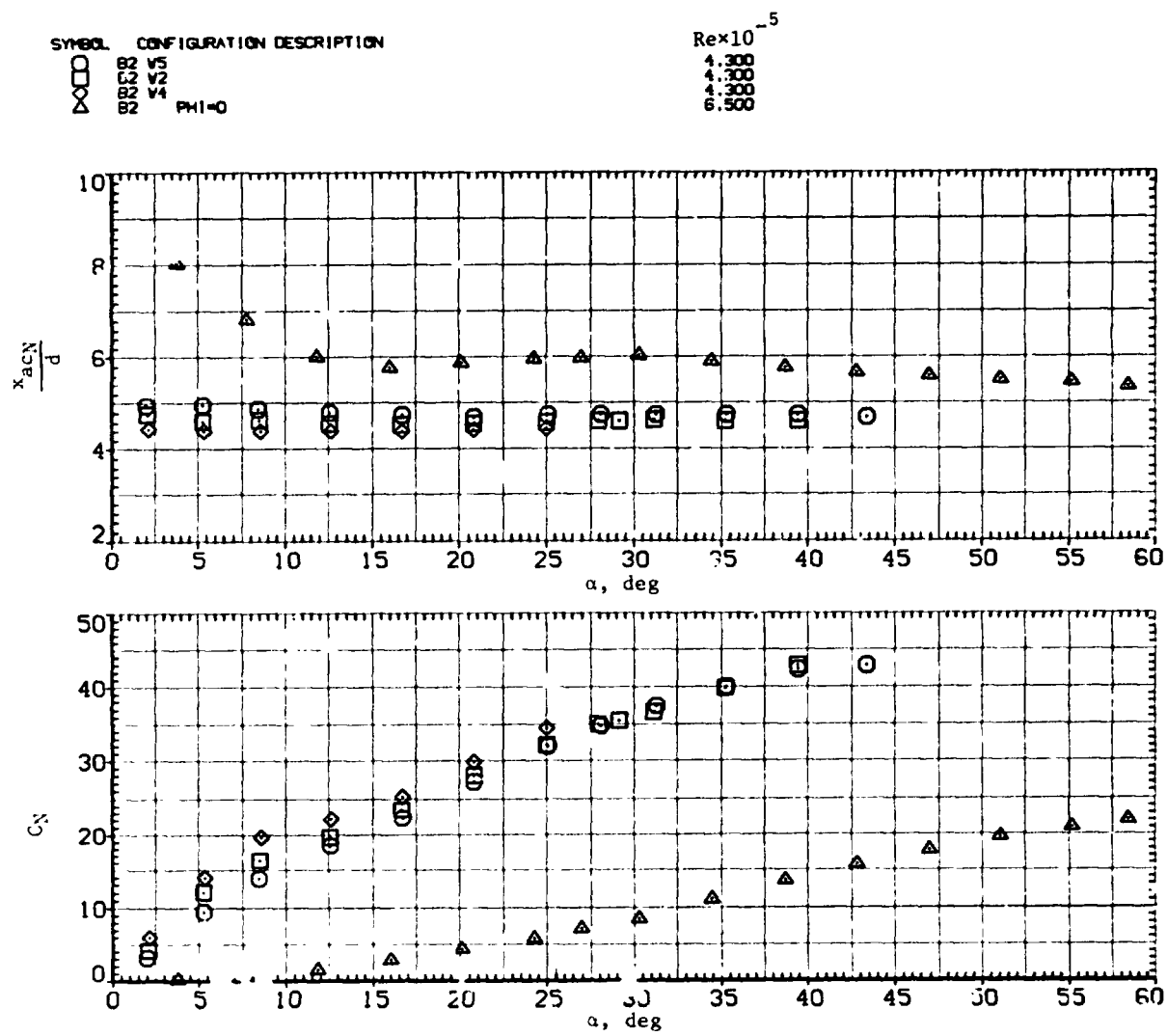
(c)  $C_A$  and  $C_n$  versus  $\alpha$ .

Figure 18.— Continued.



(a)  $x_{acN}/d$  and  $C_N$  versus  $\alpha$ .Figure 19. Effect of wing aspect ratio with elliptic body;  $M = 0.9$ .





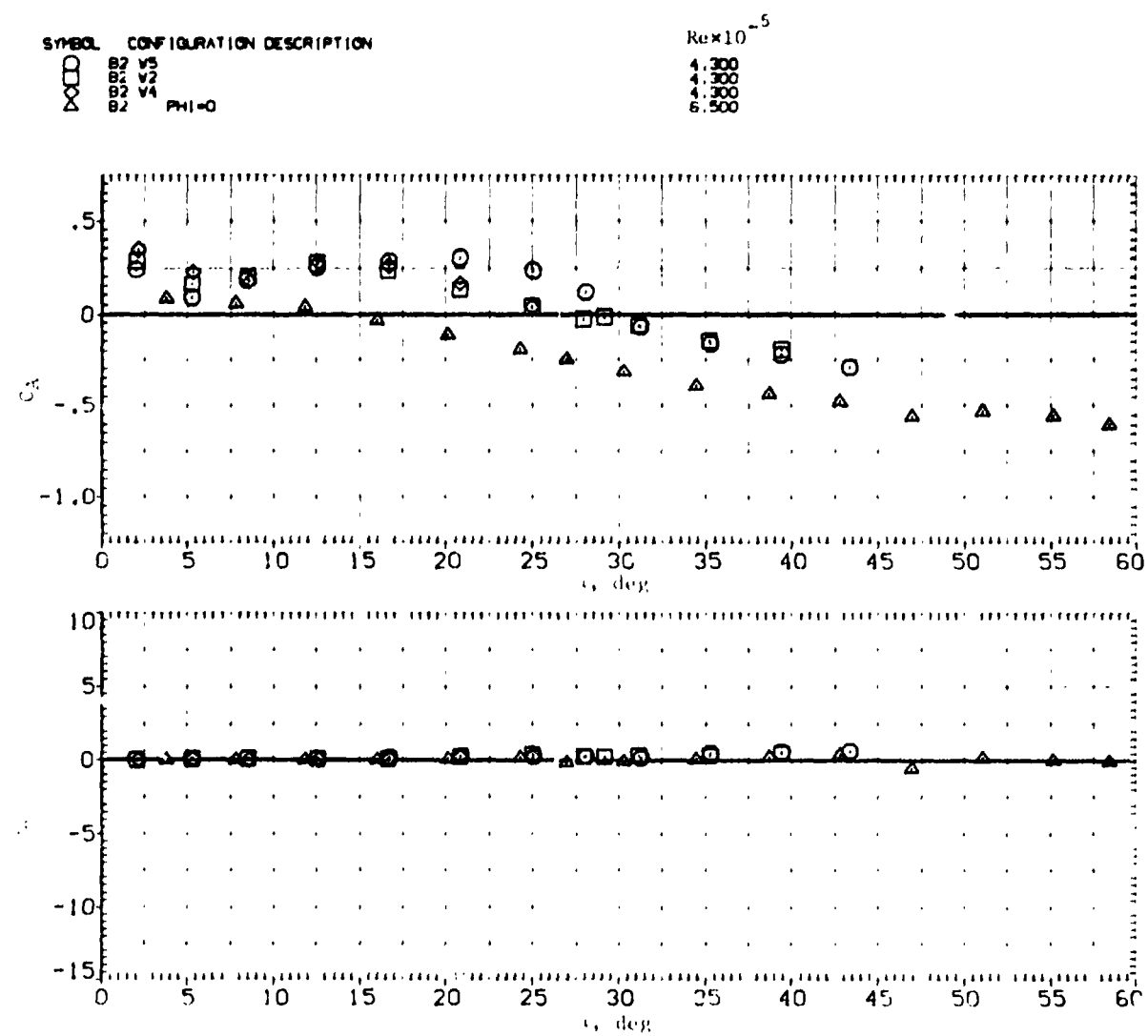
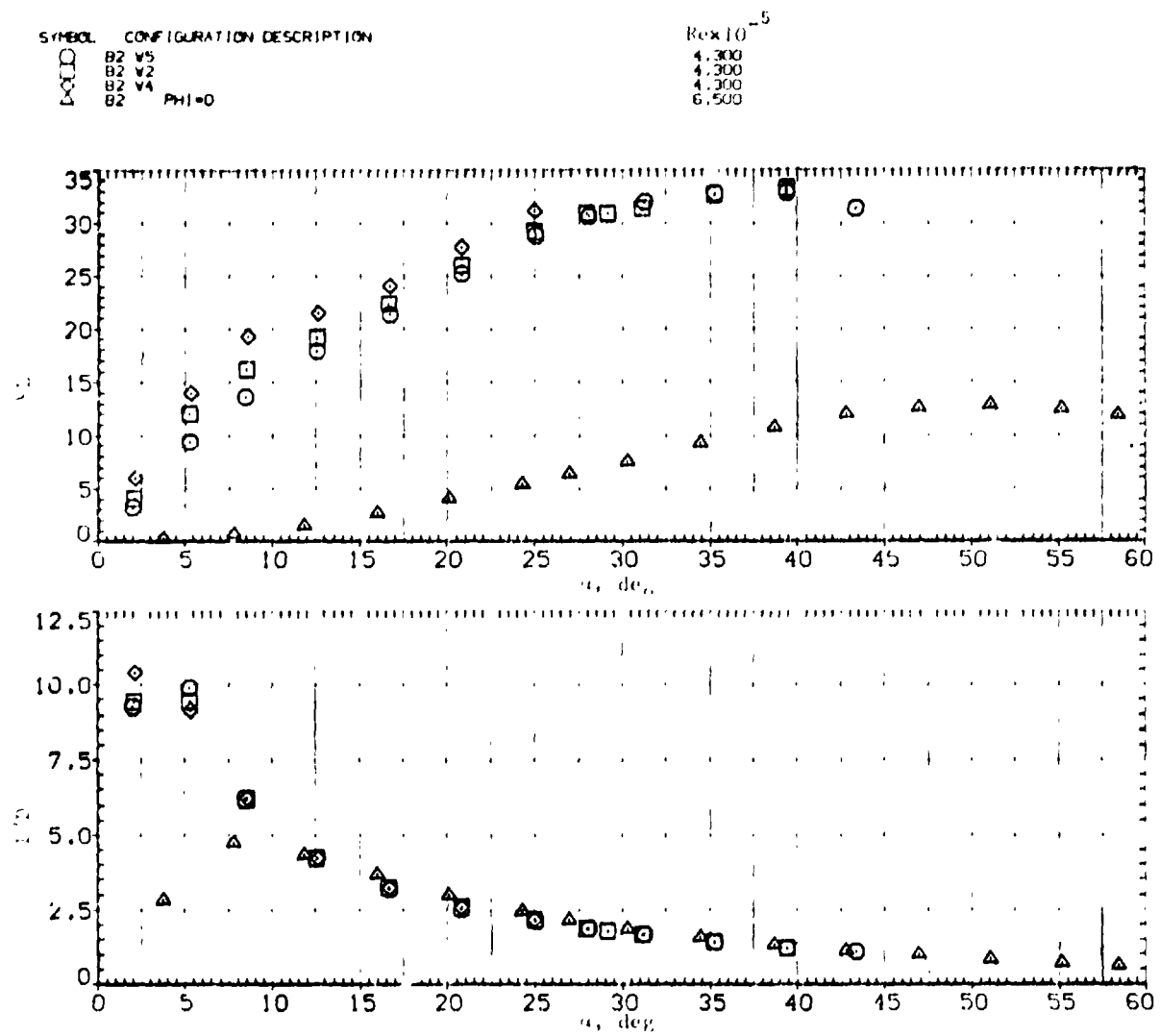
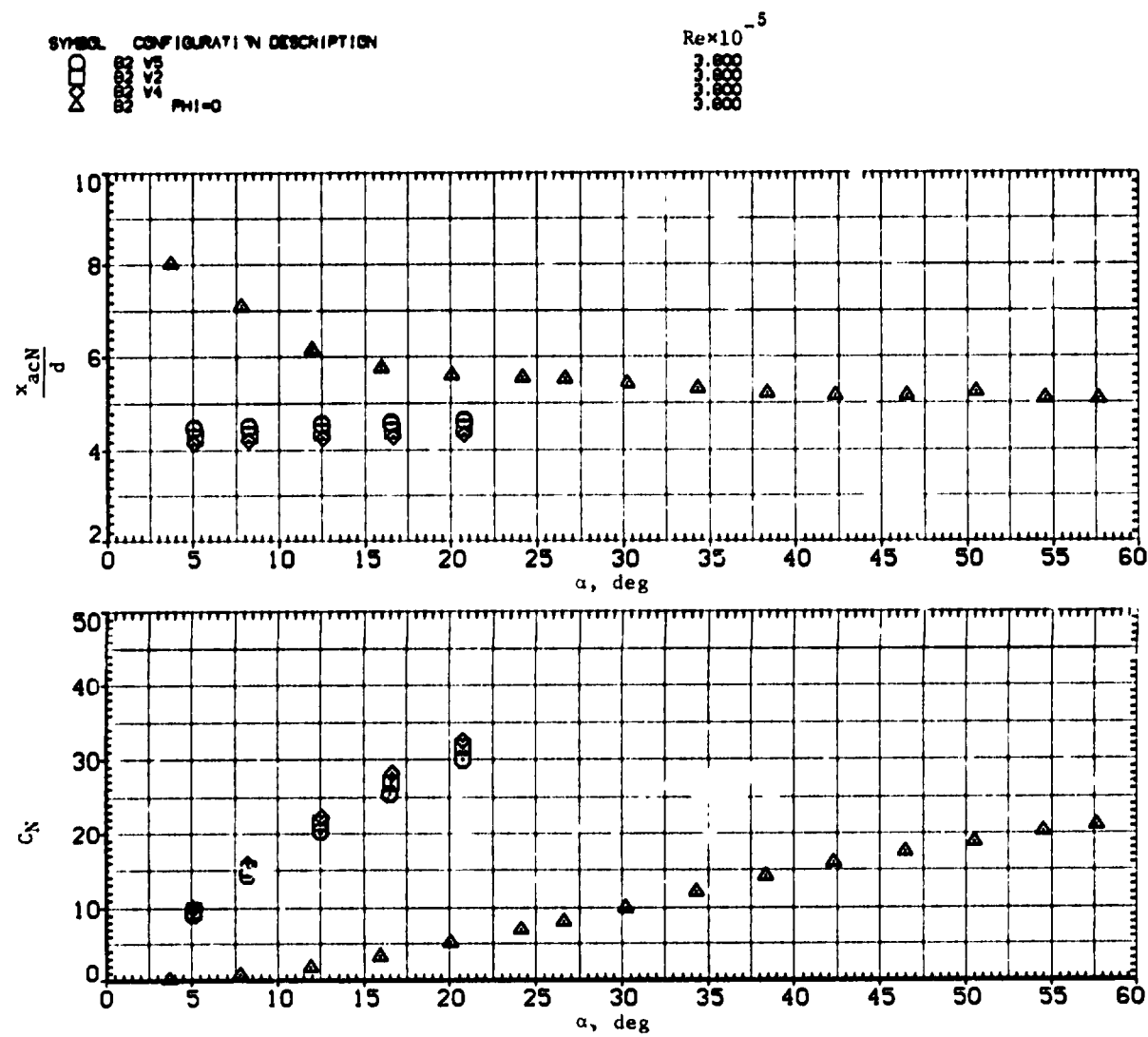
(c)  $C_A$  and  $C_D$  versus  $\alpha$ .

Figure 19. Continued.



(d)  $C_L$  and  $L/D$  versus  $\alpha$ .

Figure 19. - Concluded.



(a)  $x_{acN}/d$  and  $C_N$  versus  $\alpha$ .

**Figure 20. Effect of wing aspect ratio with elliptic body;  $M = 1.2$ .**

SYMBOL CONFIGURATION DESCRIPTION



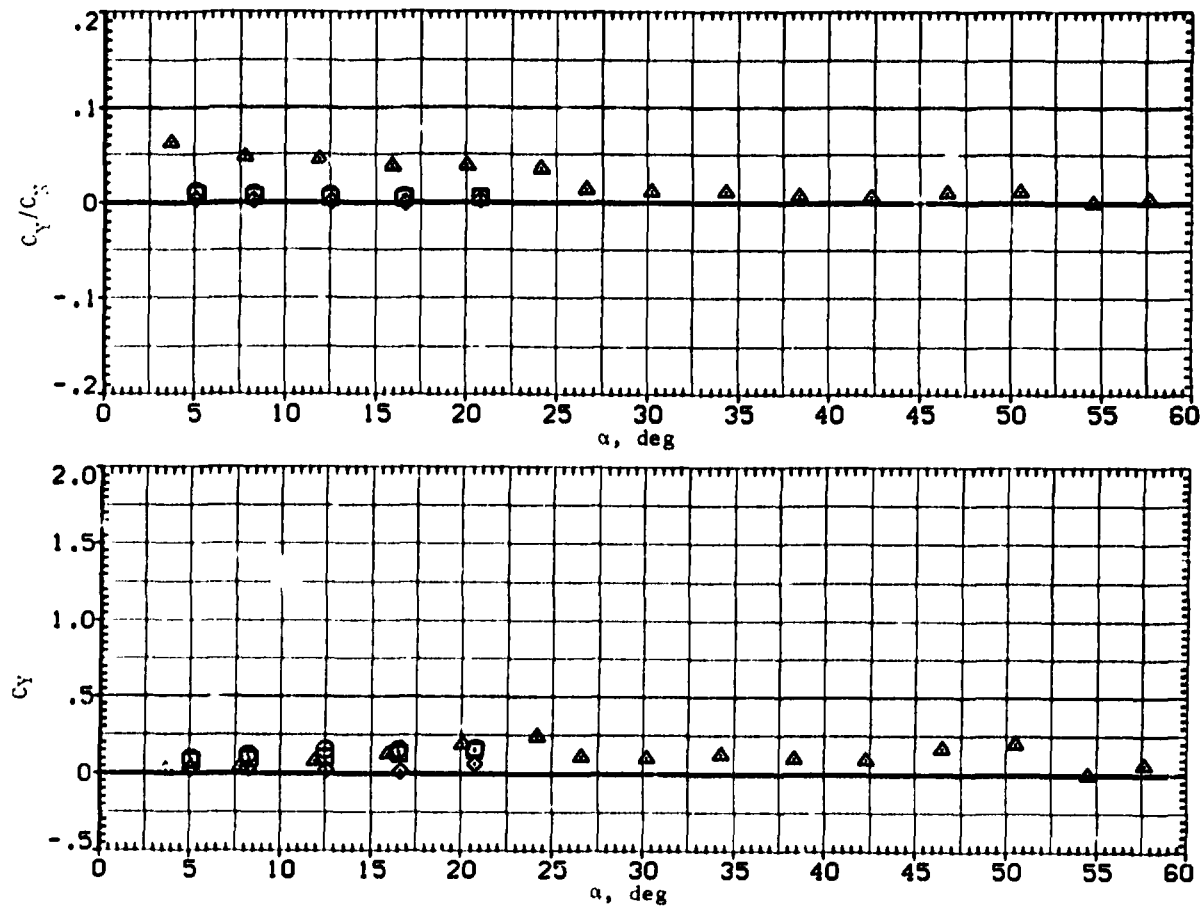
233333

5555

PHI=0

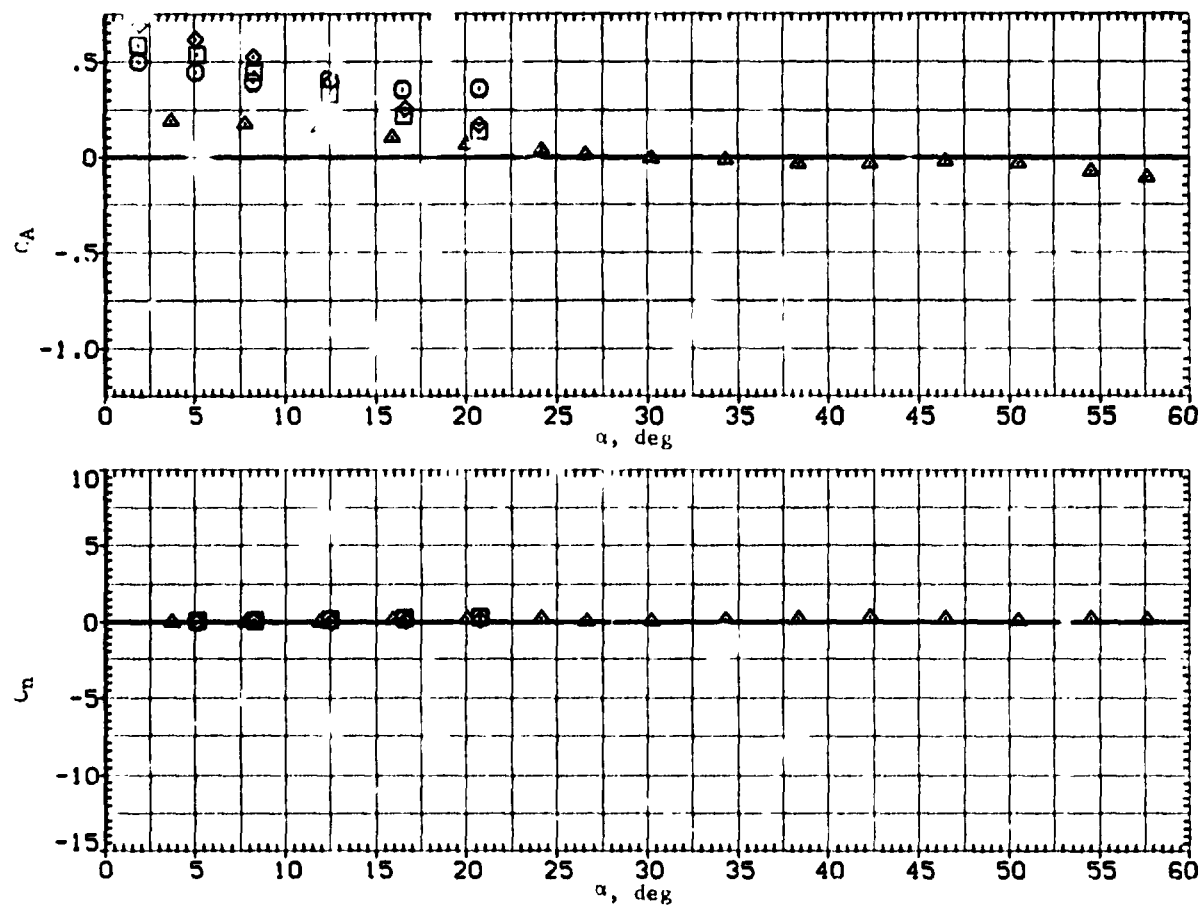
$Re \times 10^{-5}$

3.800  
3.800  
3.800  
3.800



(L)  $C_Y/C_N$  and  $C_Y$  versus  $\alpha$ .

Figure 20. - Continued.

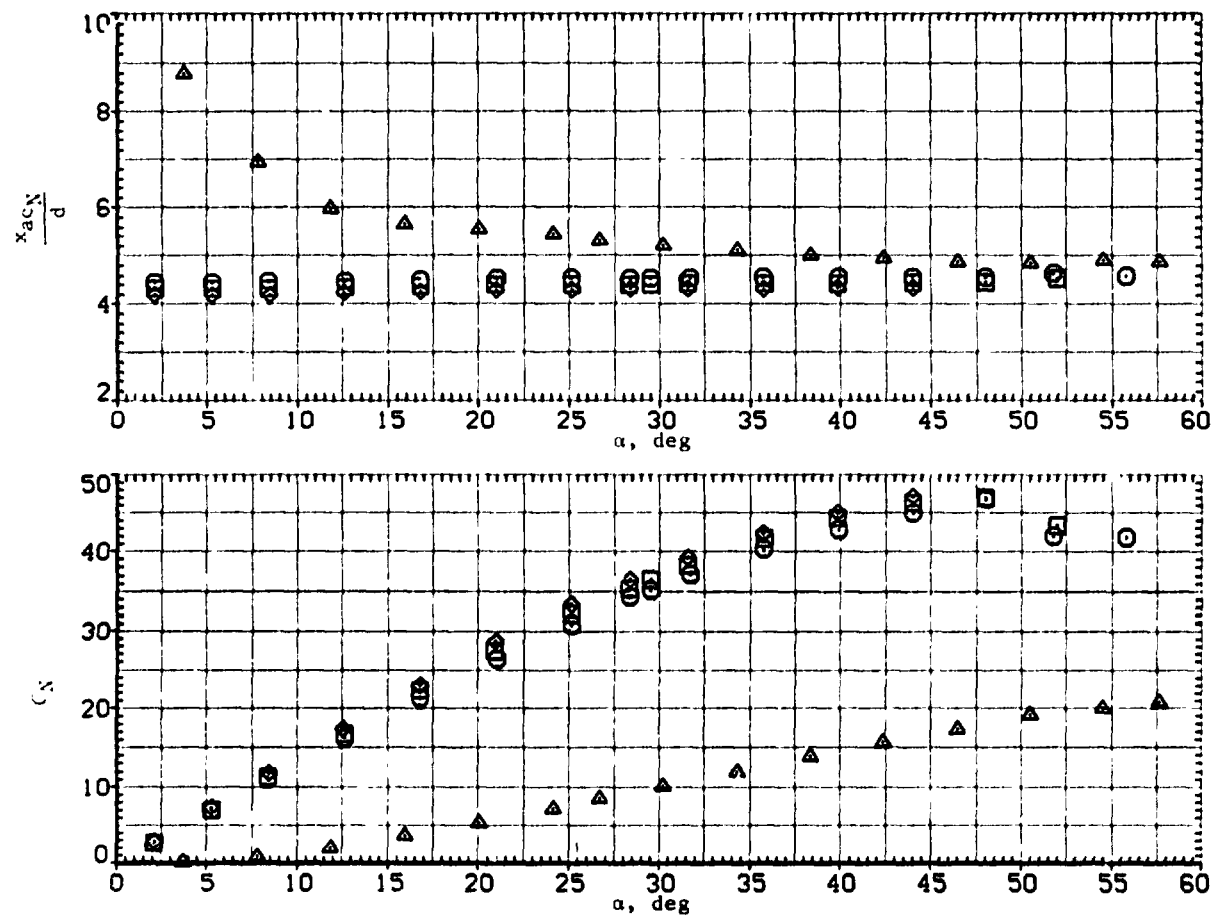


(c)  $C_A$  and  $C_n$  versus  $\alpha$ .

Figure 20.-- Continued.



SYMBOL	CONFIGURATION DESCRIPTION	$Re \times 10^{-5}$
	3.553	3.800
	5.553	3.800
	PHI=0	3.800



(a)  $x_{acN}/d$  and  $C_N$  versus  $\alpha$ .

Figure 21.— Effect of wing aspect ratio with elliptic body;  $M = 1.5$ .

REPRODUCIBILITY OF THE  
ORIGINAL PAGE IS POOR





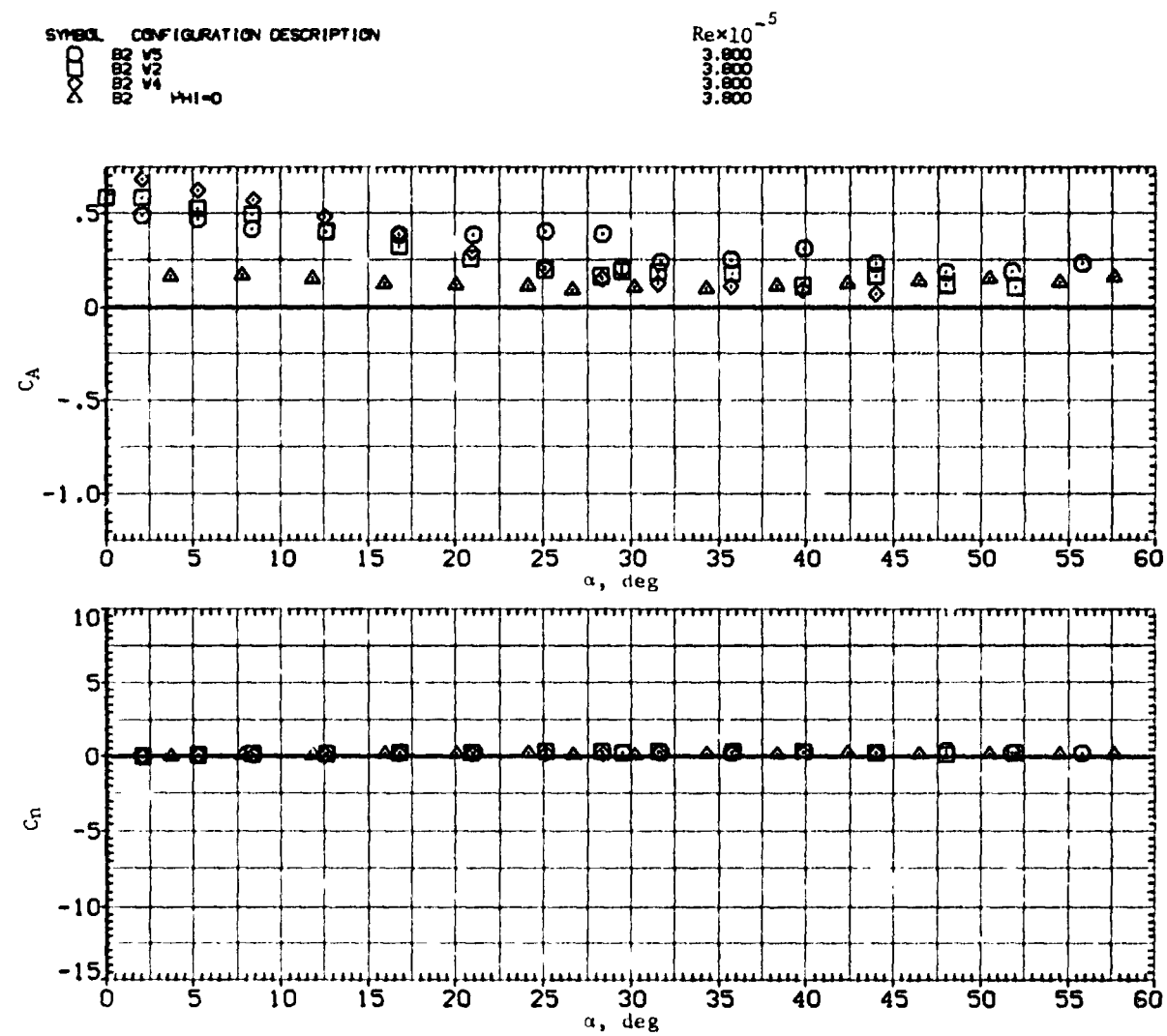
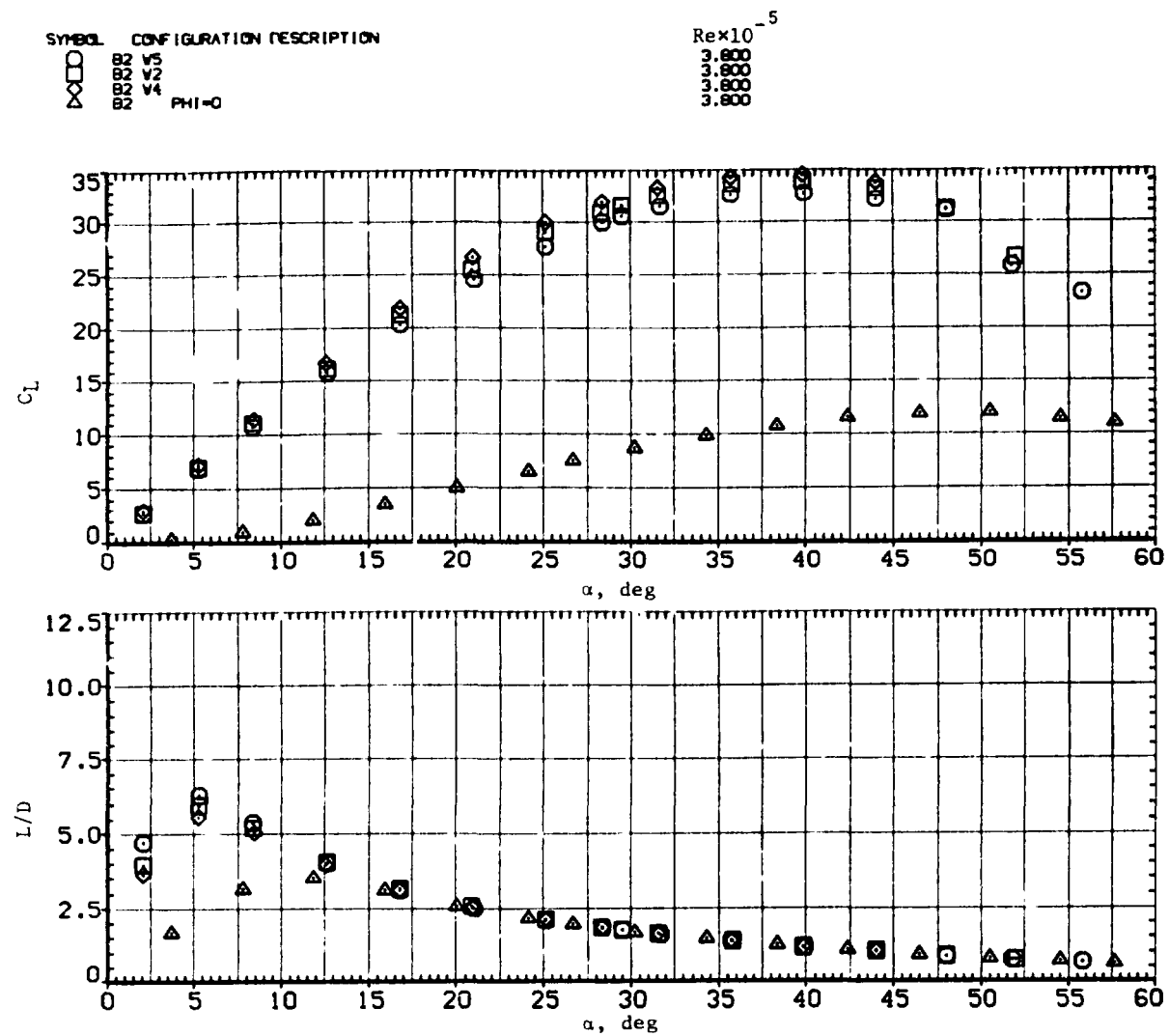
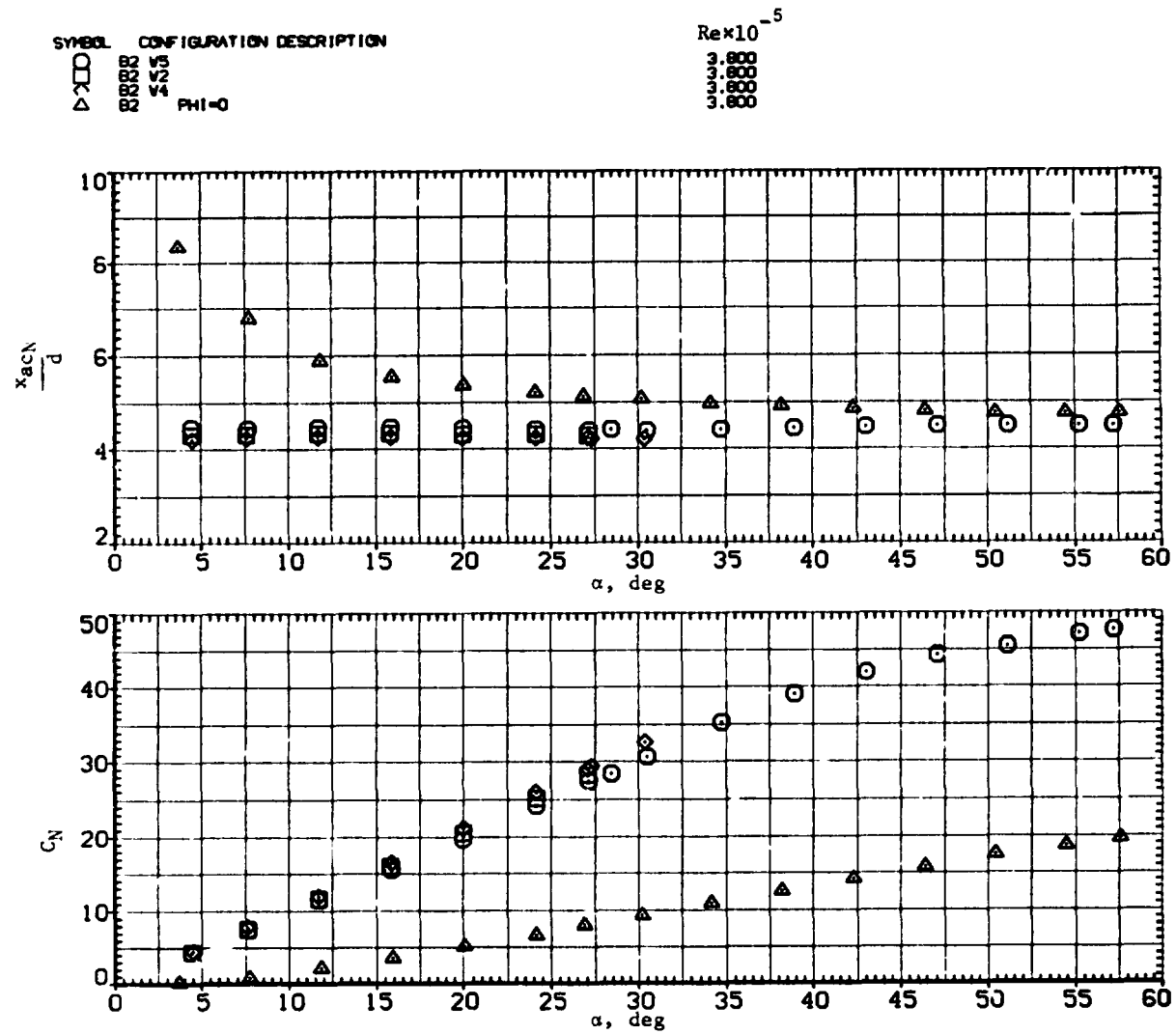
(c)  $C_A$  and  $C_n$  versus  $\alpha$ .

Figure 21.- Continued.



(d)  $C_L$  and  $L/D$  versus  $\alpha$ .

Figure 21.— Concluded.



(a)  $x_{acN}/d$  and  $C_N$  versus  $\alpha$ .

Figure 22.— Effect of wing aspect ratio with elliptic body;  $M = 2.0$ .



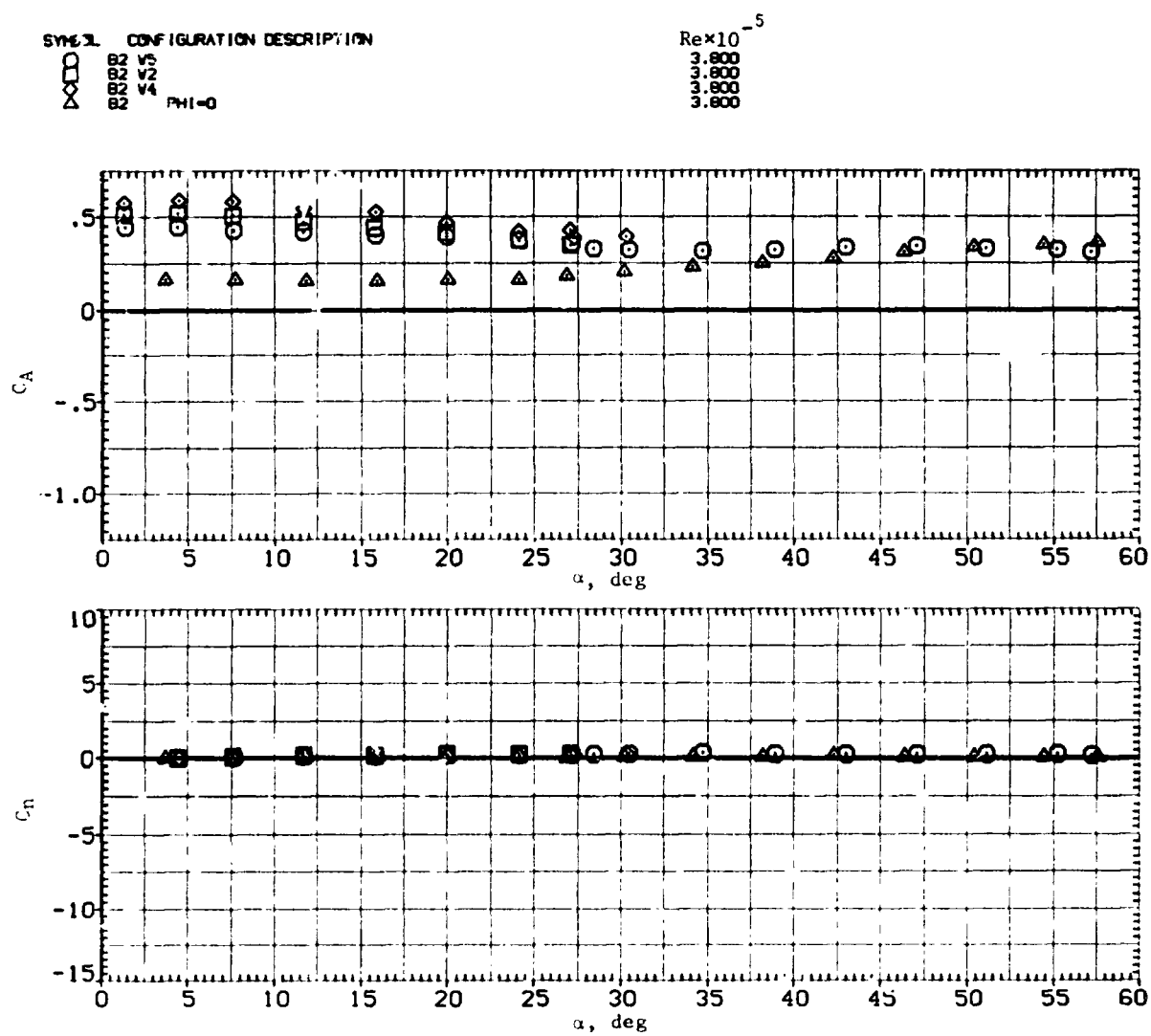
(c)  $C_A$  and  $C_n$  versus  $\alpha$ .

Figure 22. Continued.

SYMBOL CONFIGURATION DESCRIPTION  $Re \times 10^{-5}$

$\circ$  1.0  $\square$  2.0  $\triangle$  3.0

$\Phi = 0$

$C_L$

$\alpha, \text{deg}$

$L/D$

$\alpha, \text{deg}$

**Figure 22.— Concluded.**

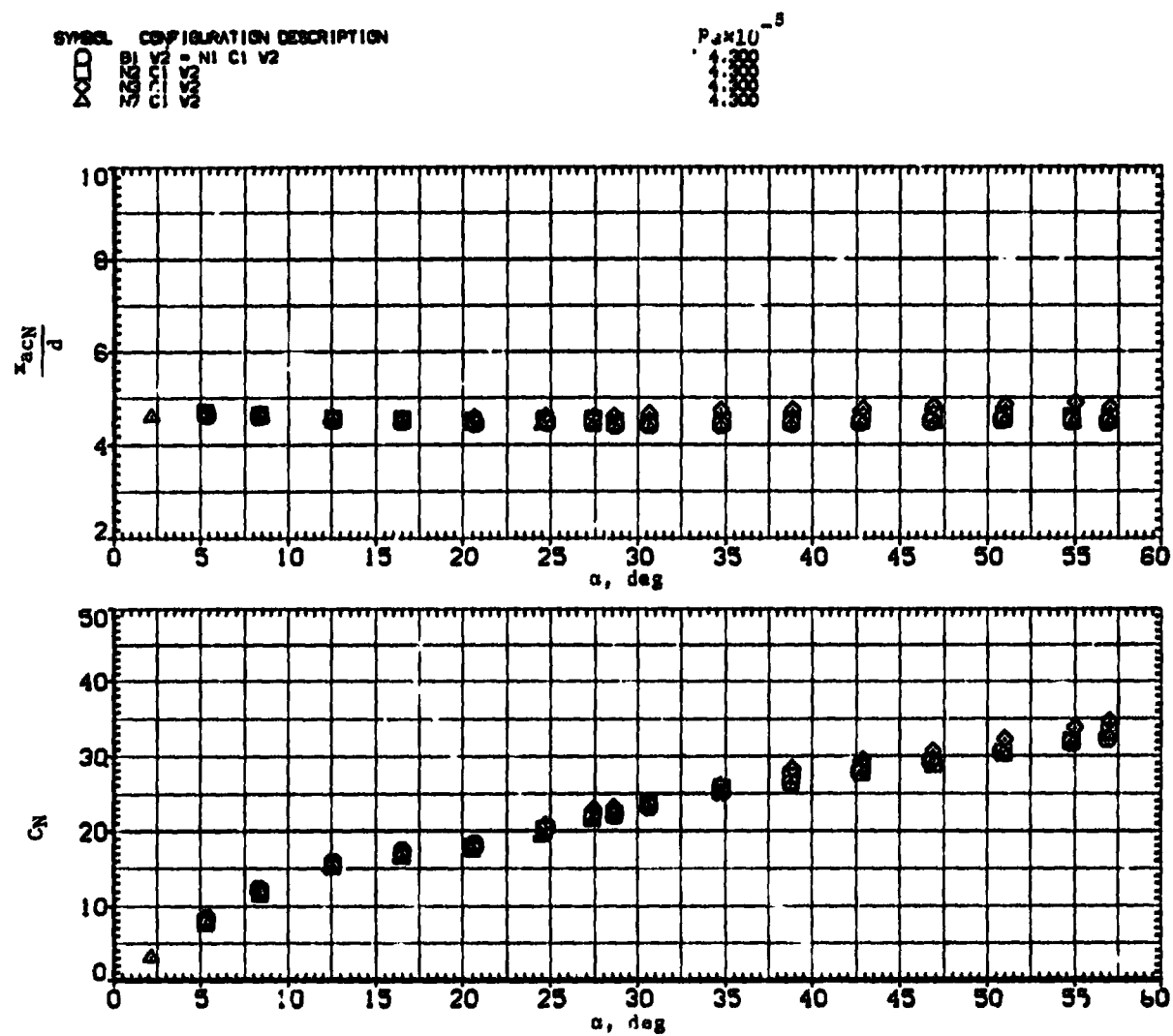
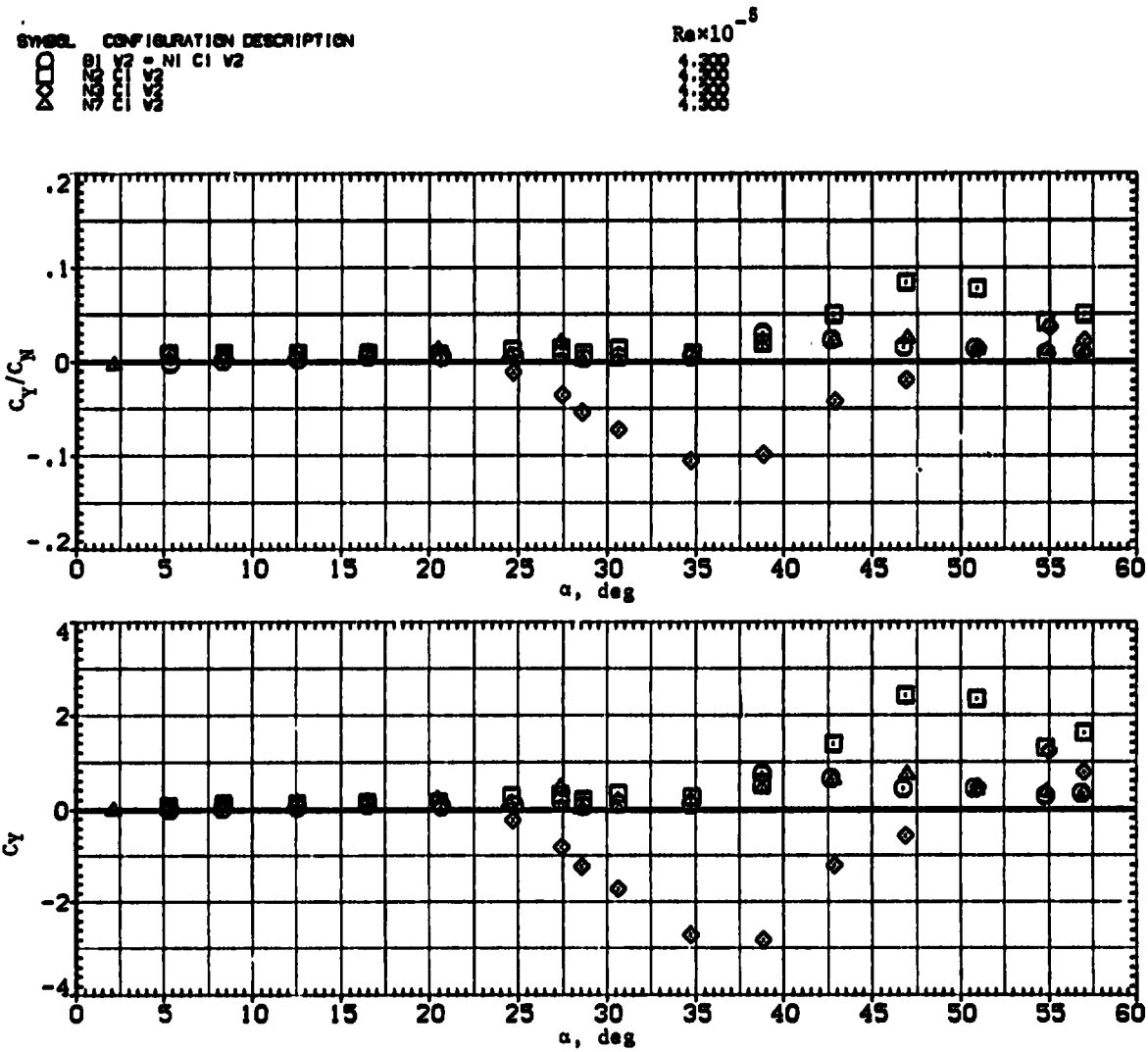


Figure 23.— Effect of nose fineness ratio on wing-body characteristics;  $M = 0.6$ .



(b)  $C_Y/C_N$  and  $C_Y$  versus  $\alpha$ .

Figure 23.— Continued.



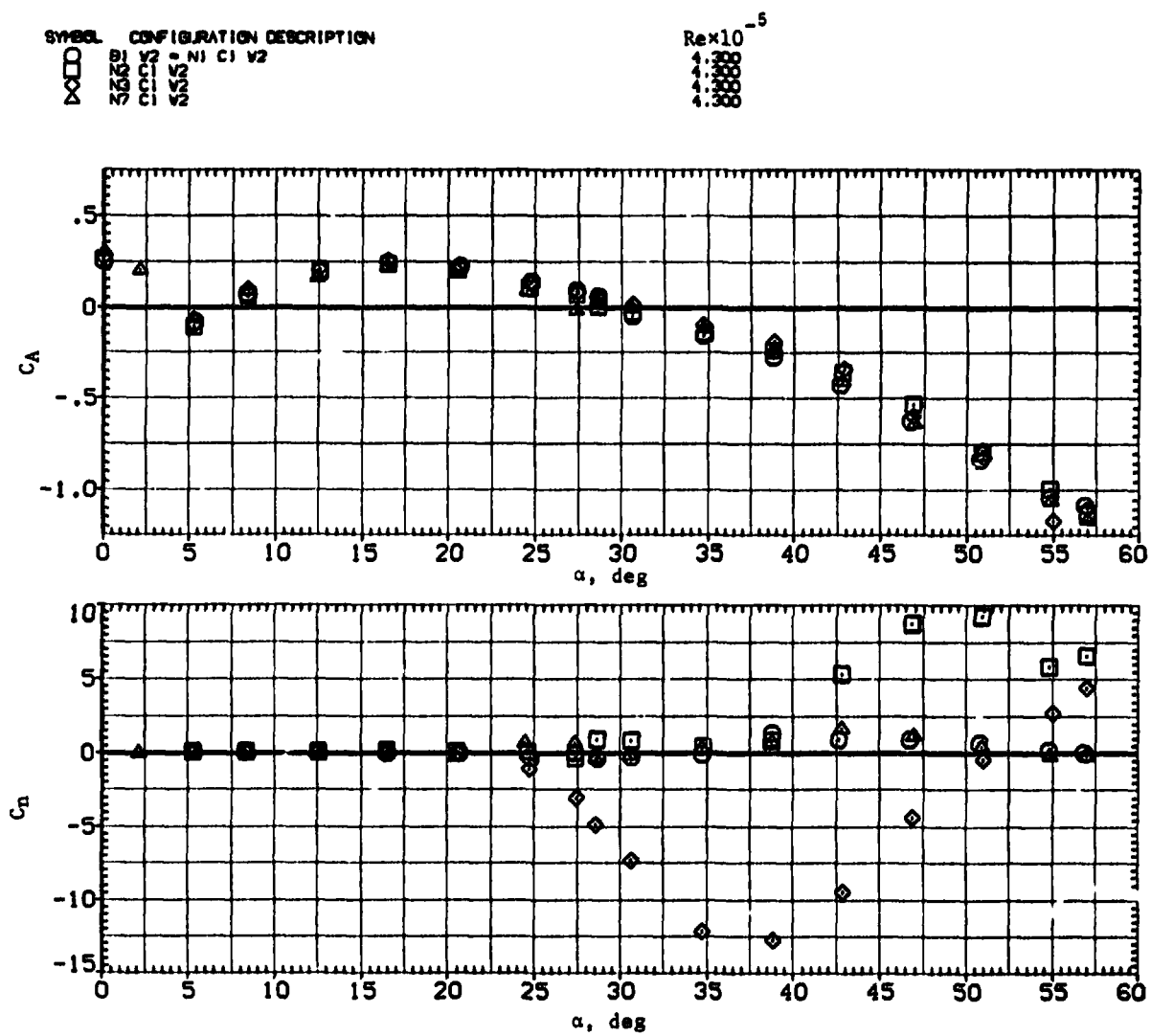
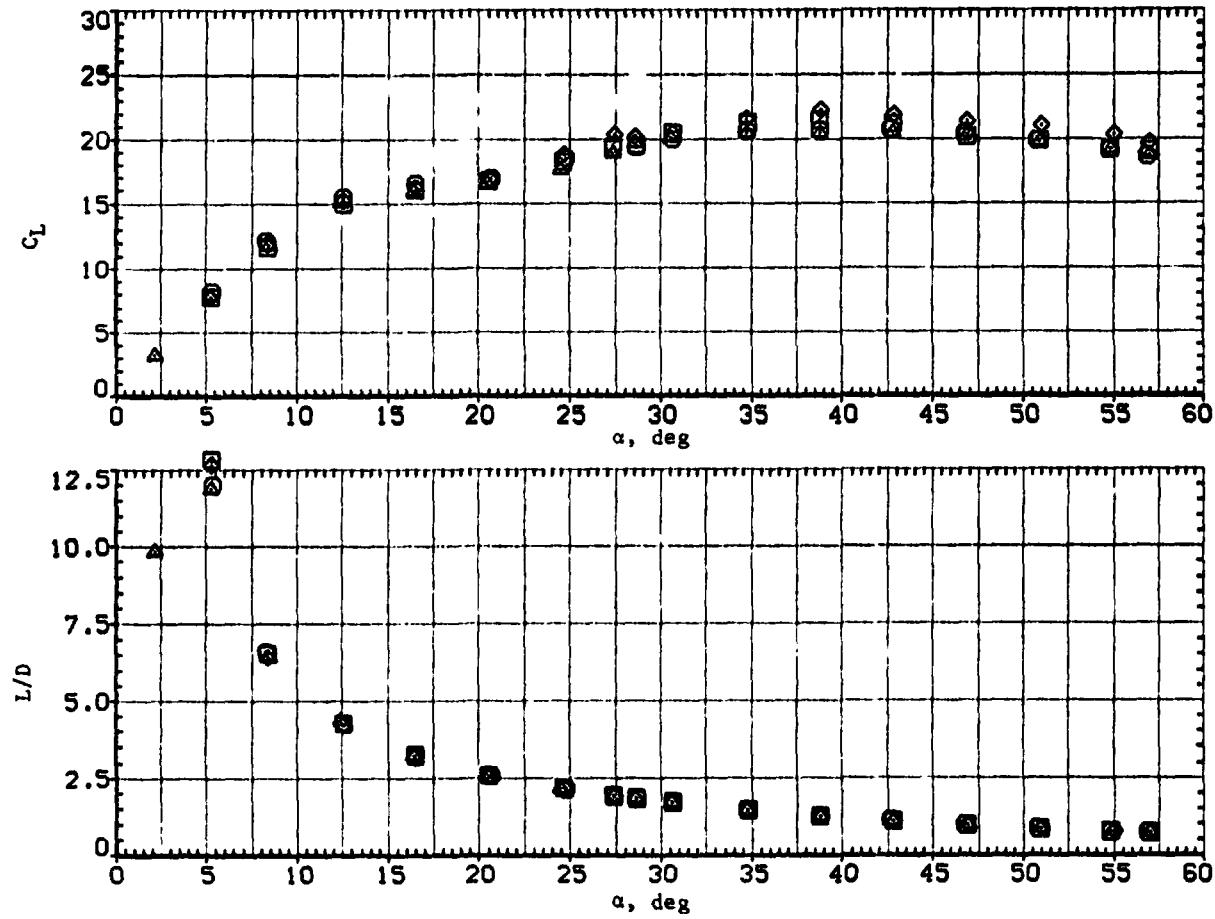
(c)  $C_A$  and  $C_n$  versus  $\alpha$ .

Figure 23.— Continued.

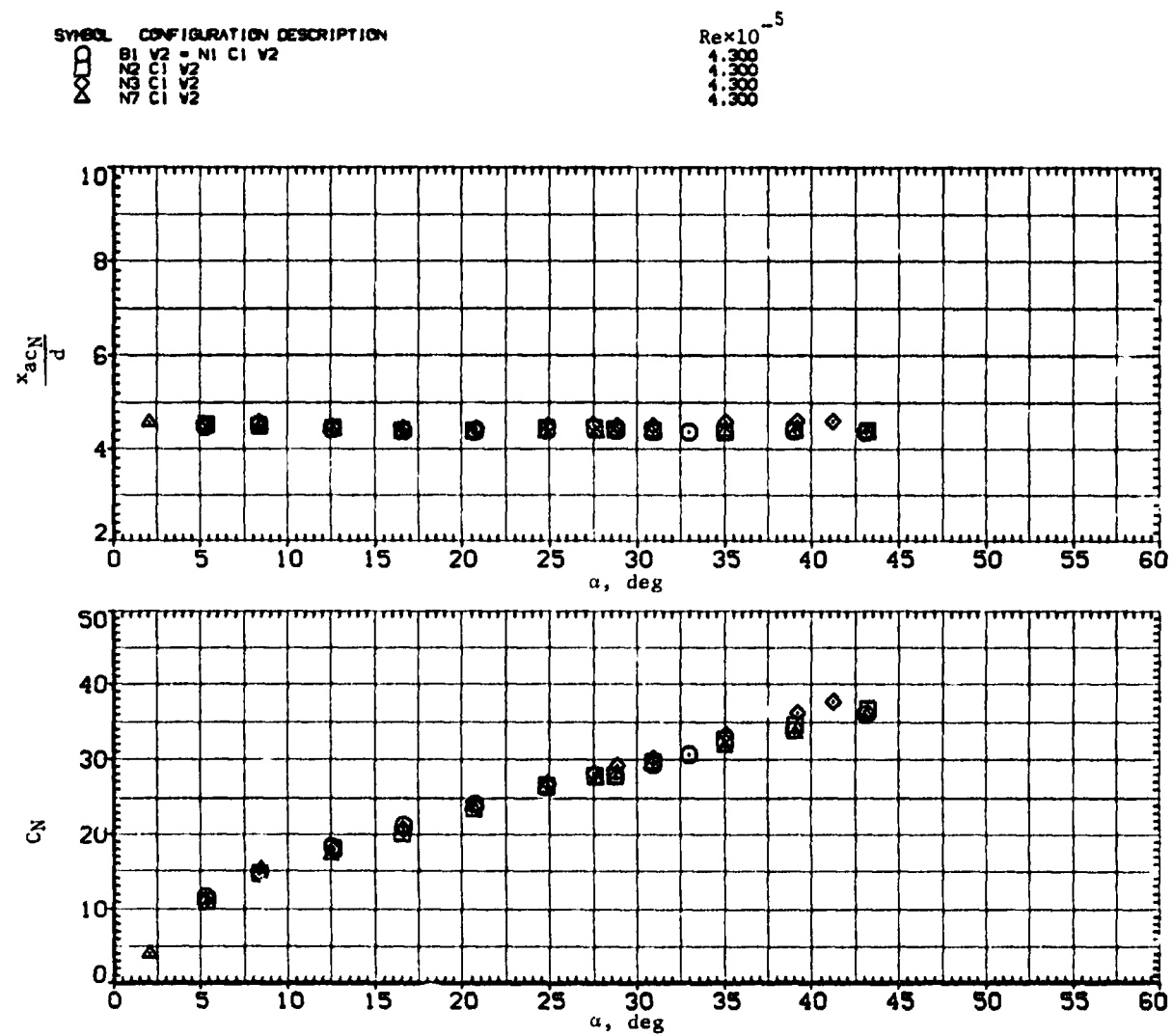
SYMBOL CONFIGURATION DESCRIPTION  
 □ BI  
 ○ CI  
 △ V2

Re × 10<sup>-4</sup>  
 4.300  
 4.300  
 4.300  
 4.300  
 4.300



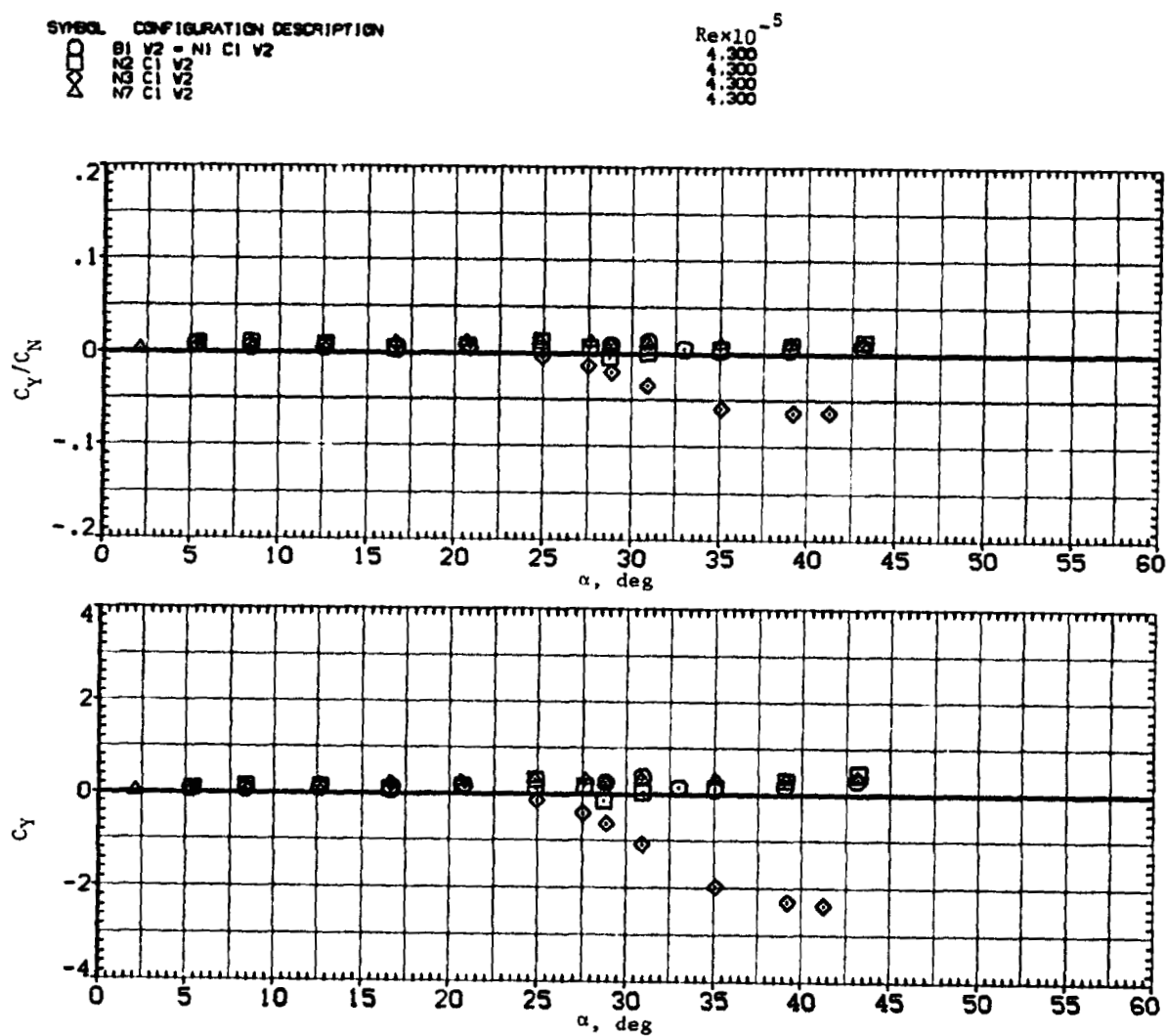
(d)  $C_L$  and  $L/D$  versus  $\alpha$ .

Figure 23.— Concluded.



(a)  $x_{acN}/d$  and  $C_N$  versus  $\alpha$ .

Figure 24.— Effect of nose fineness ratio on wing-body characteristics;  $M = 0.9$ .



(b)  $C_Y/C_N$  and  $C_Y$  versus  $\alpha$ .

Figure 24.— Continued.

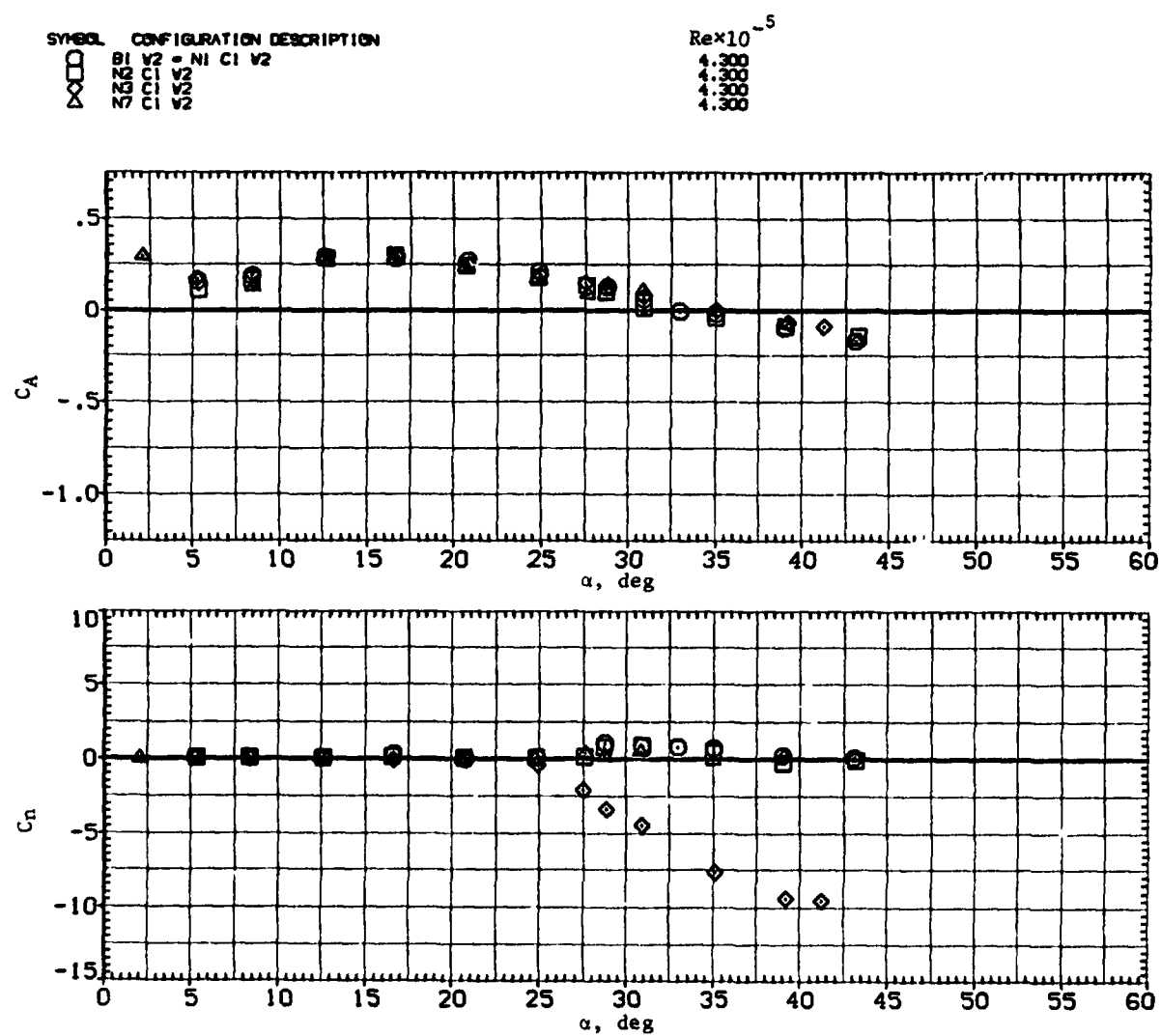
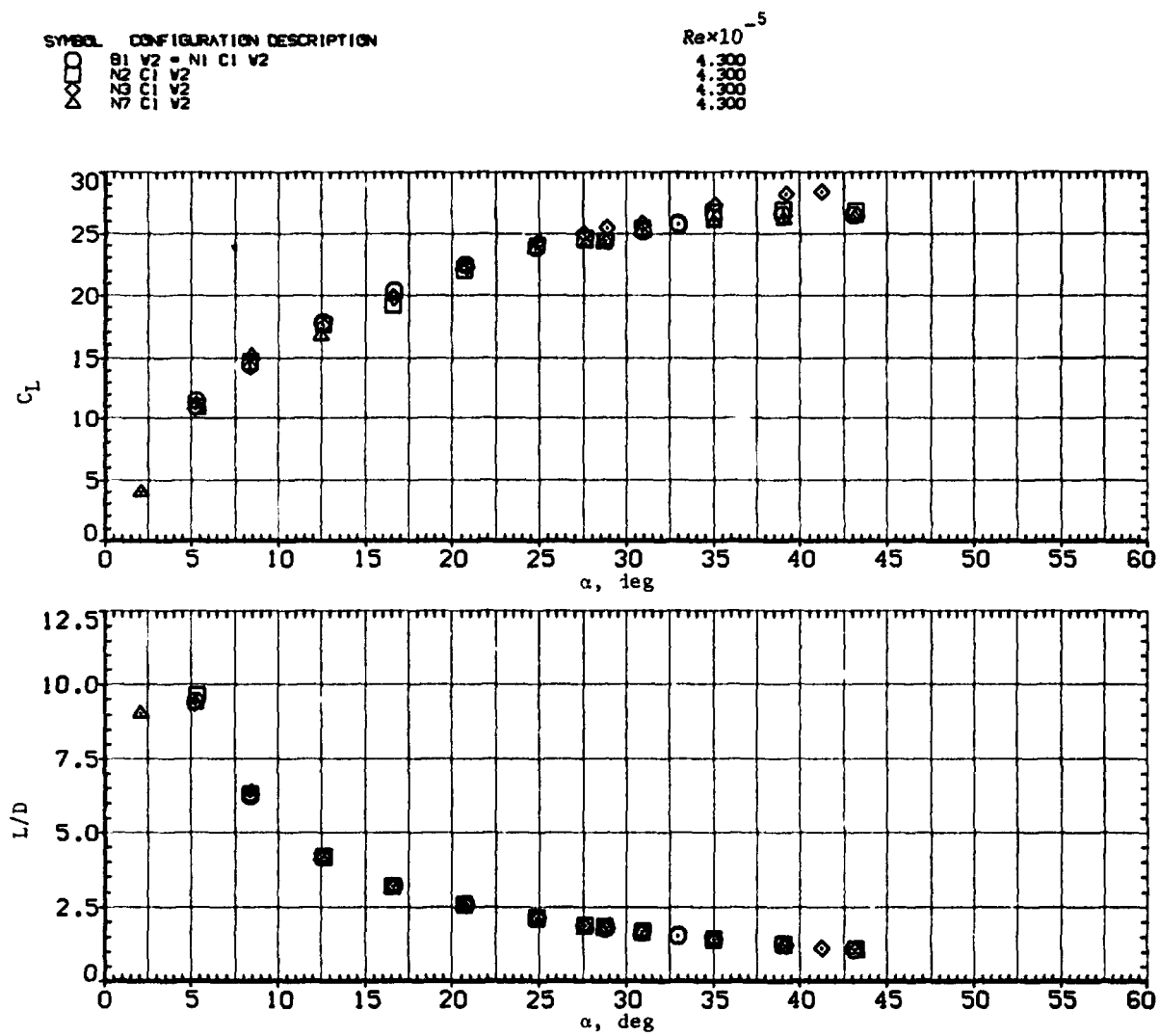
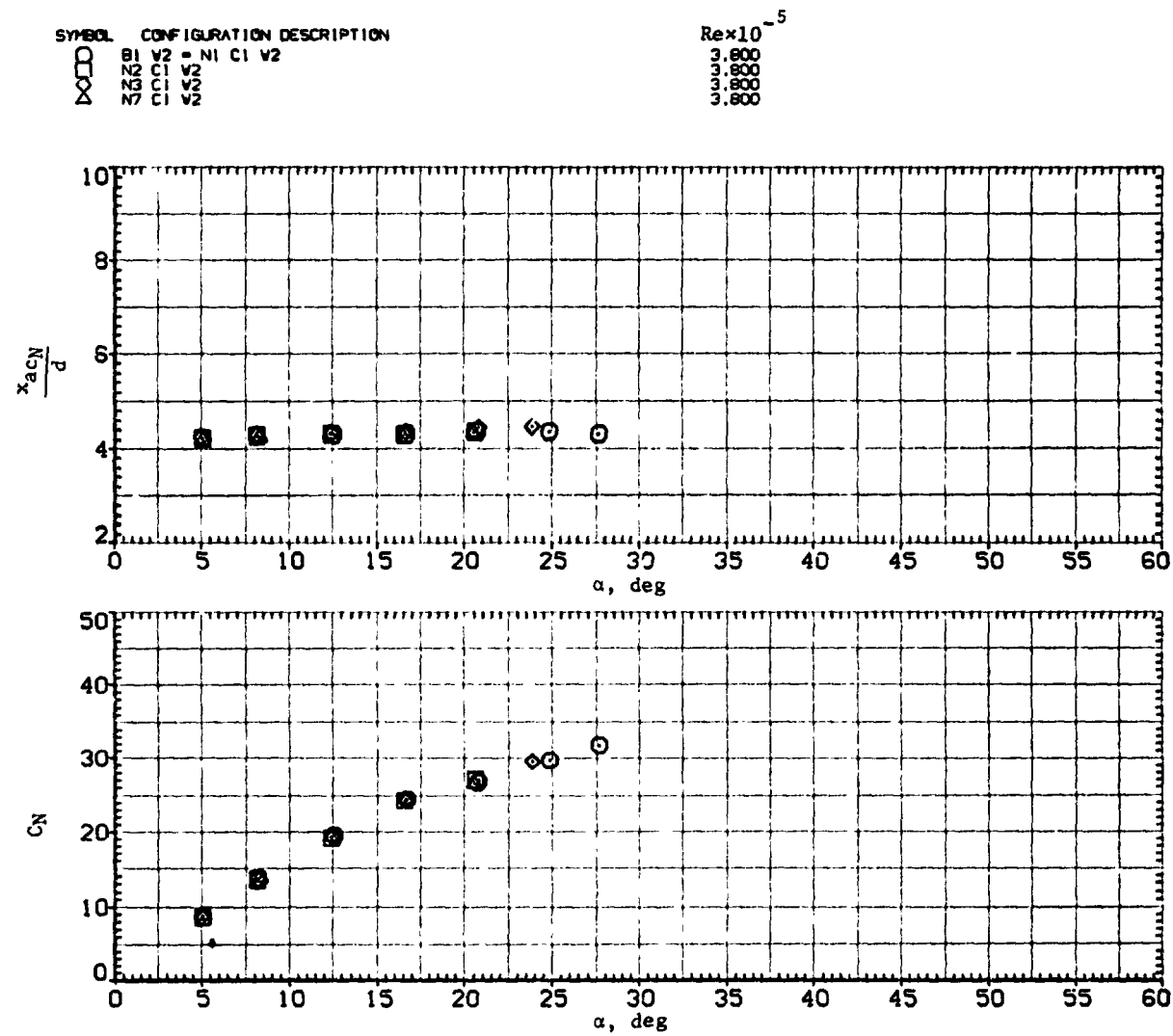
(c)  $C_A$  and  $C_n$  versus  $\alpha$ .

Figure 24.— Continued.

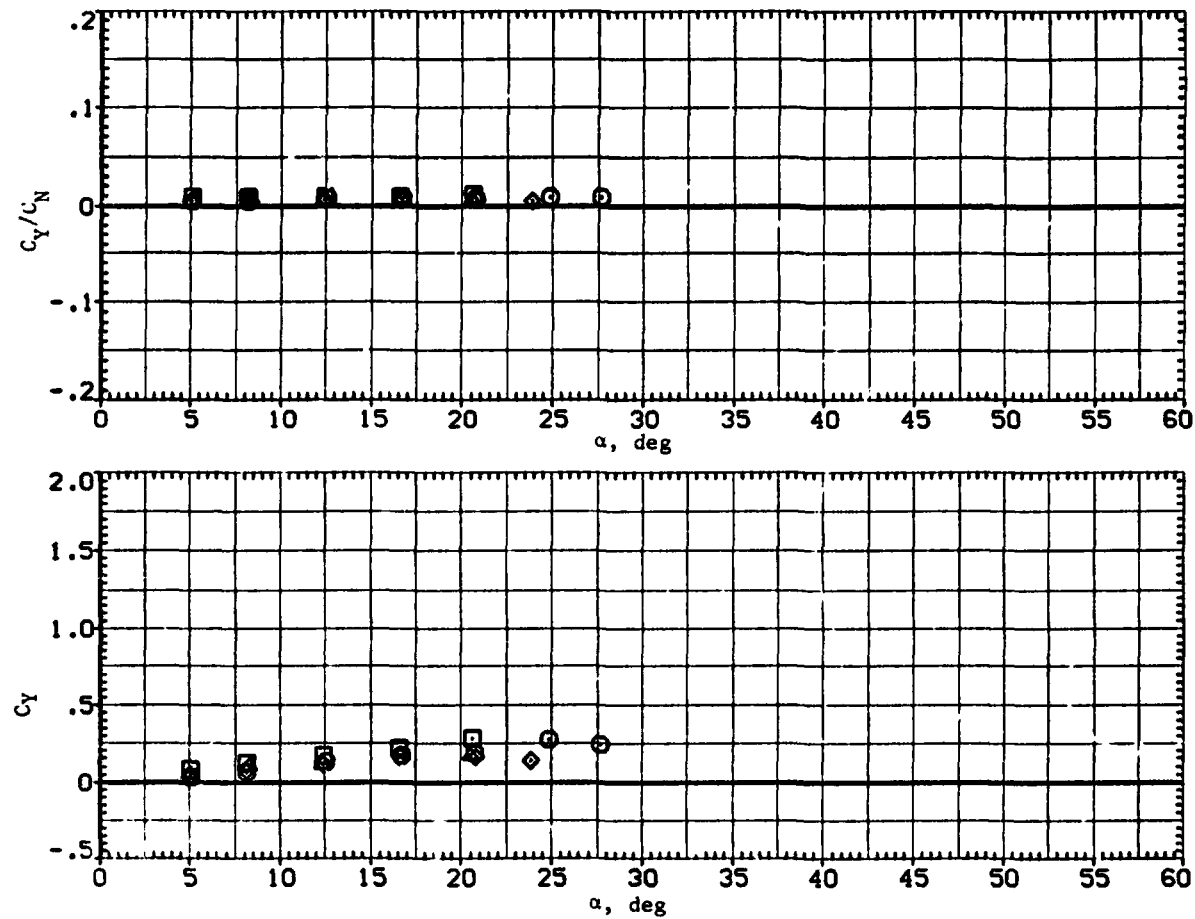


(d)  $C_L$  and  $L/D$  versus  $\alpha$ .

Figure 24. - Concluded.

(a)  $x_{acN}/d$  and  $C_N$  versus  $\alpha$ .Figure 25.— Effect of nose fineness ratio on wing-body characteristics;  $M = 1.2$ .

SYMBOL	CONFIGURATION DESCRIPTION	BETA	Re $\times 10^{-5}$
$\square$	B1 V2 = N1 C1 V2	.000	3.000
$\diamond$	N1 C1 V2	.000	3.000
$\circ$	C1 V2	.000	3.000



(b)  $C_Y/C_N$  and  $C_Y$  versus  $\alpha$ .

Figure 25.-- Continued.



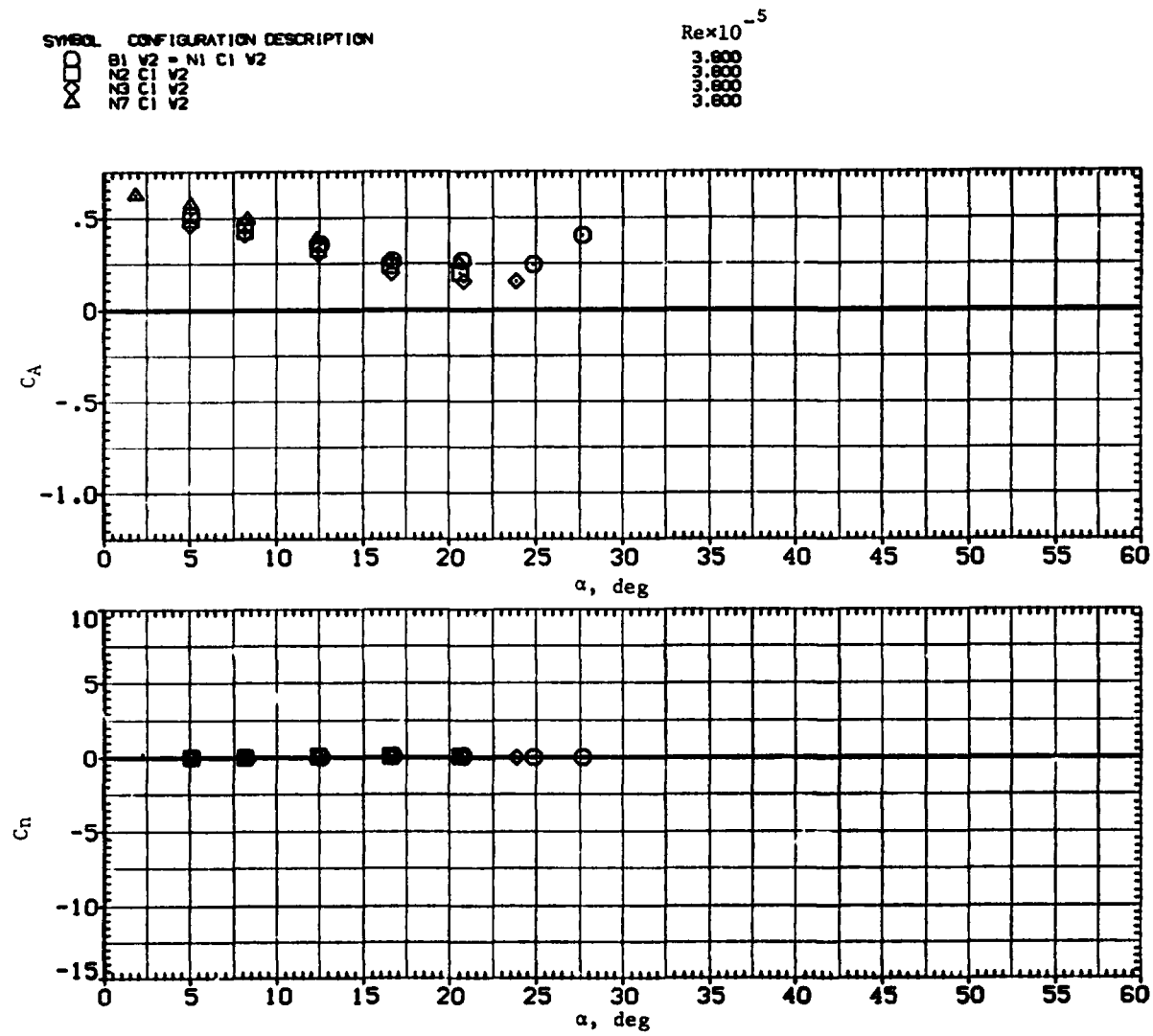
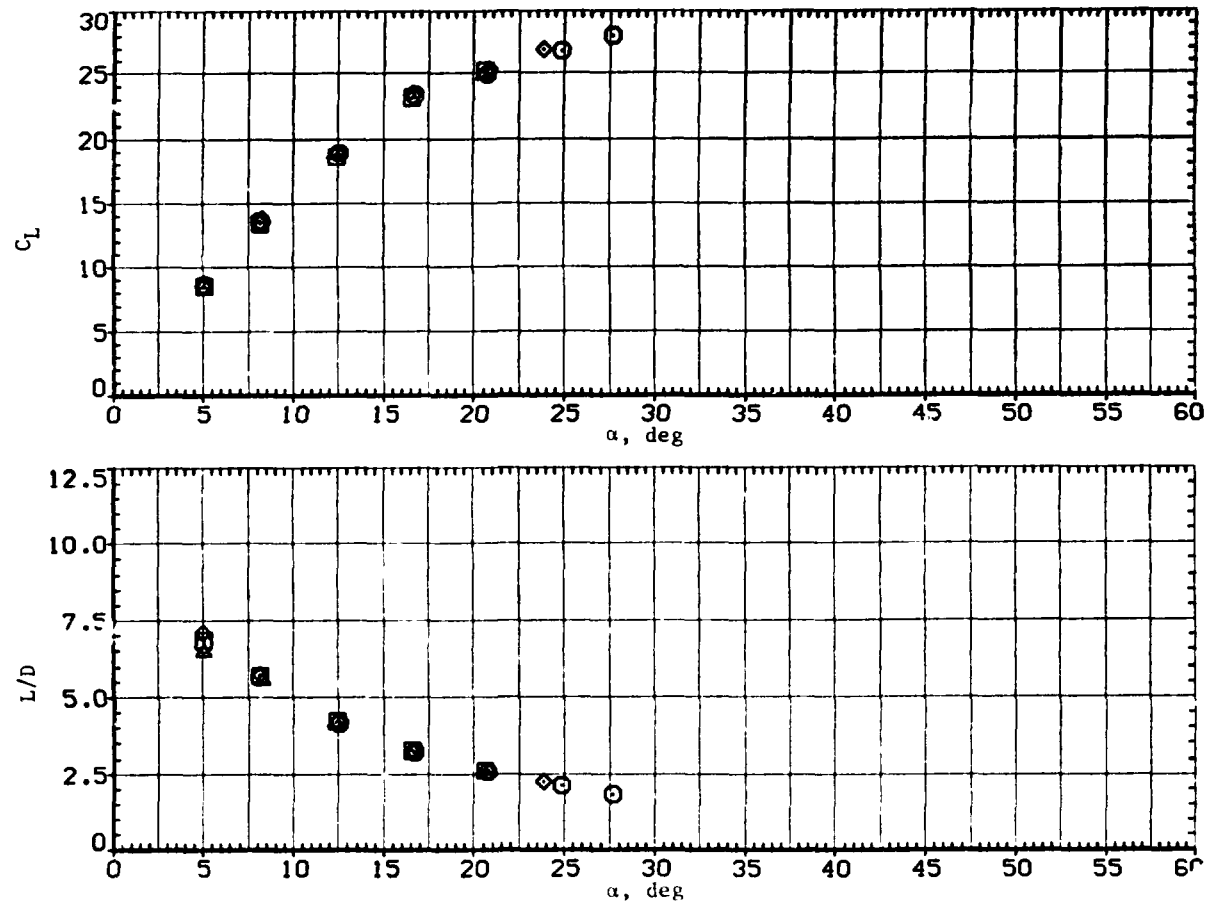
(c)  $C_A$  and  $C_n$  versus  $\alpha$ .

Figure 25.— Continued.

SYMBOL	CONFIGURATION DESCRIPTION	$Re \times 10^{-5}$
$\square$	B1 V2 = NI C1 V2	3.800
$\diamond$	N2 C1 V2	3.800
$\triangle$	N3 C1 V2	3.800
$\nabla$	N7 C1 V2	3.800



(d)  $C_L$  and  $L/D$  versus  $\alpha$ .

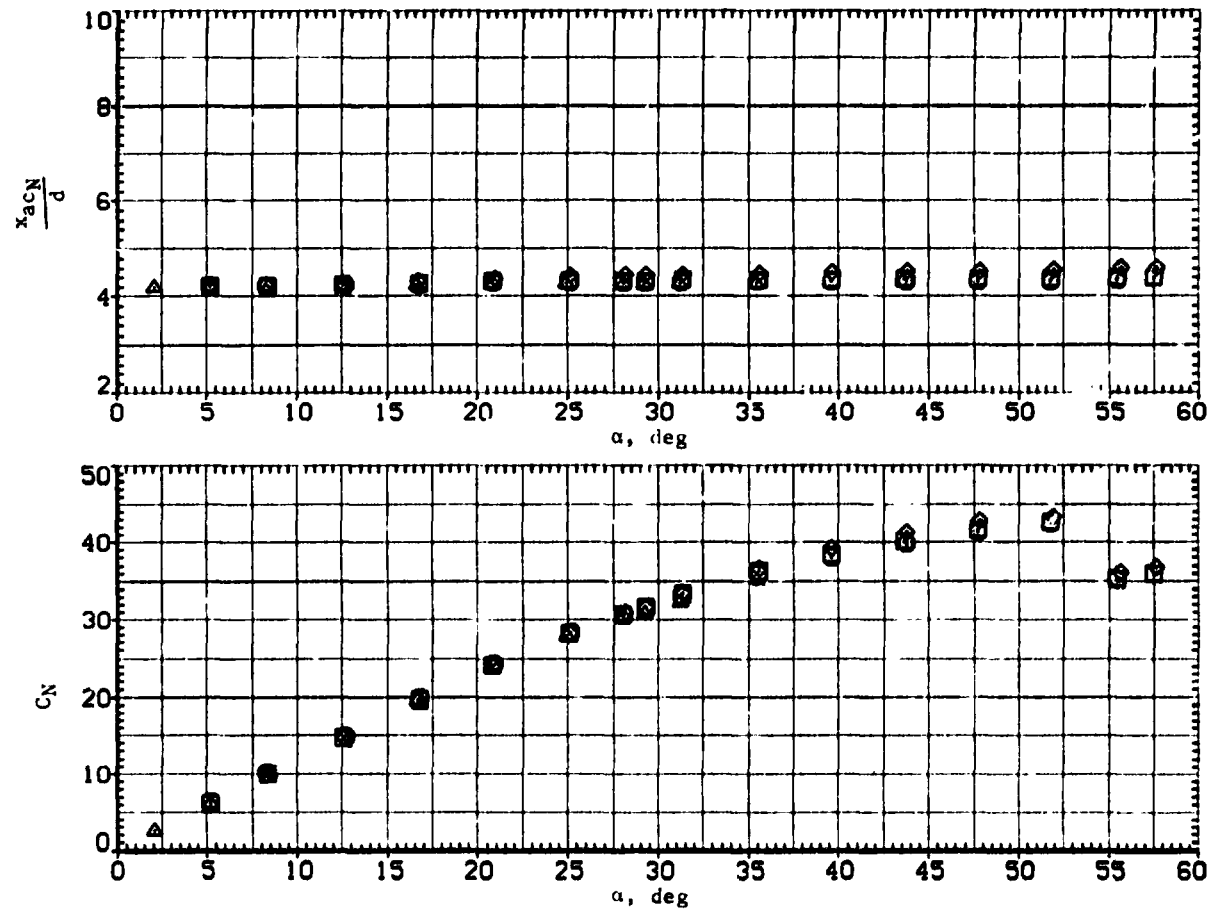
Figure 25.— Concluded.

SYMBOL CONFIGURATION DESCRIPTION

SYMBOL	CONFIGURATION DESCRIPTION
□	NI
△	CI
○	V2

$Re \times 10^{-5}$

□	1000
△	2000
○	3000
×	4000
+	5000
•	6000
×	7000
+	8000
•	9000

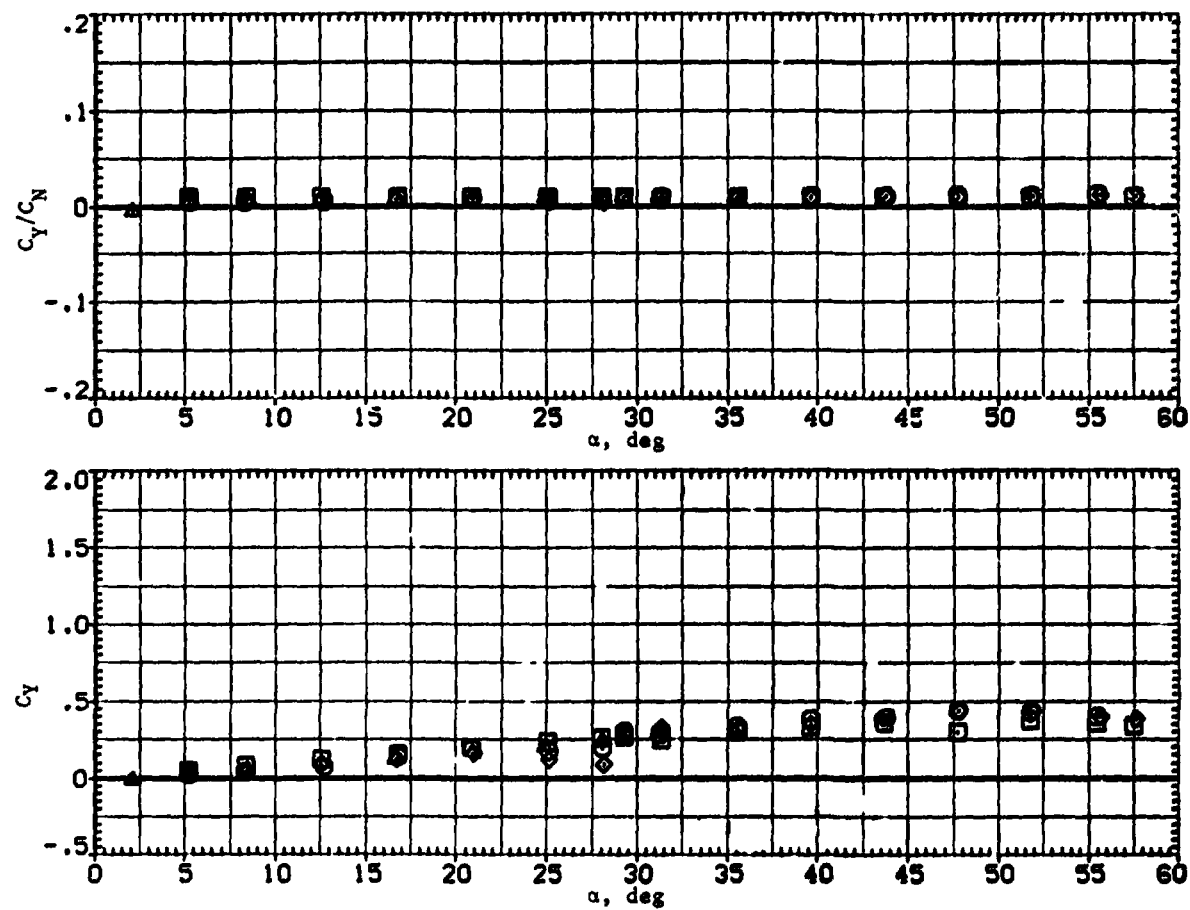


(a)  $x_{acN}/d$  and  $C_N$  versus  $\alpha$ .

Figure 26.— Effect of nose fineness ratio on wing-body characteristics;  $M = 1.5$ .

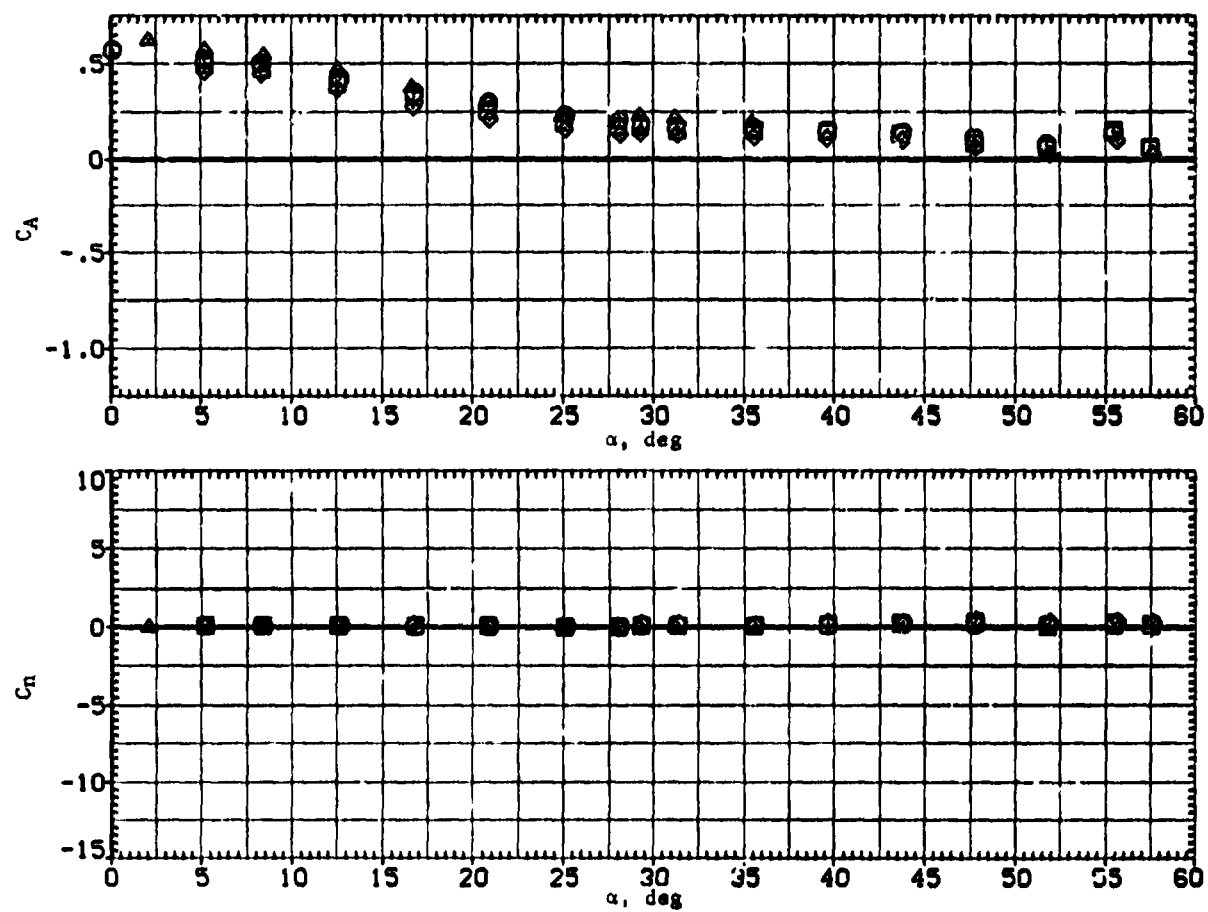
REPRODUCIBILITY OF THE  
ORIGINAL PAGE IS POOR

SYMBOL	CONFIGURATION DESCRIPTION	$Re \times 10^{-5}$
$\square$	B1	3.8888
$\circ$	S1	3.8888
$\triangle$	C1	3.8888
$\times$	V2	3.8888



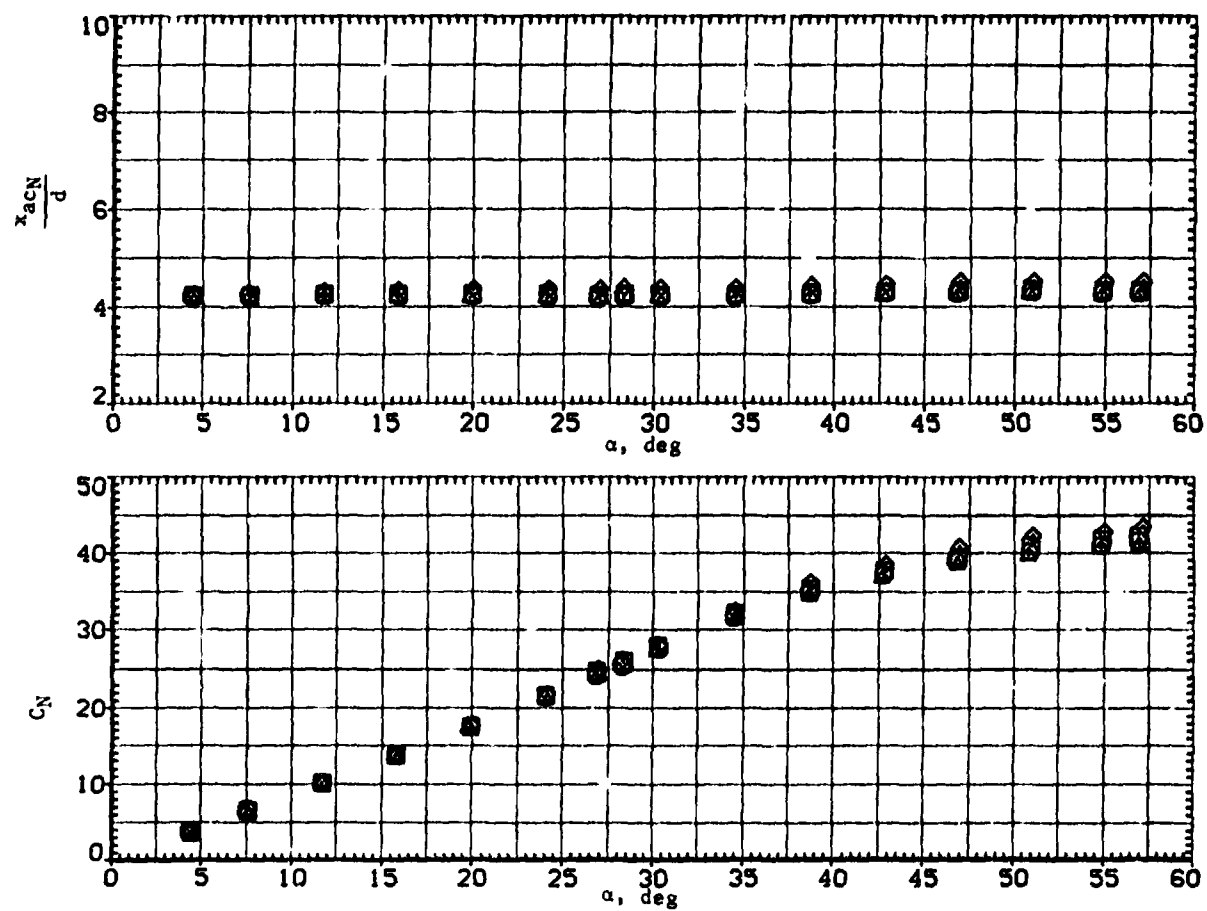
(b)  $C_Y/C_N$  and  $C_Y$  versus  $\alpha$ .

Figure 26.— Continued.







**Figure 26.— Continued.**

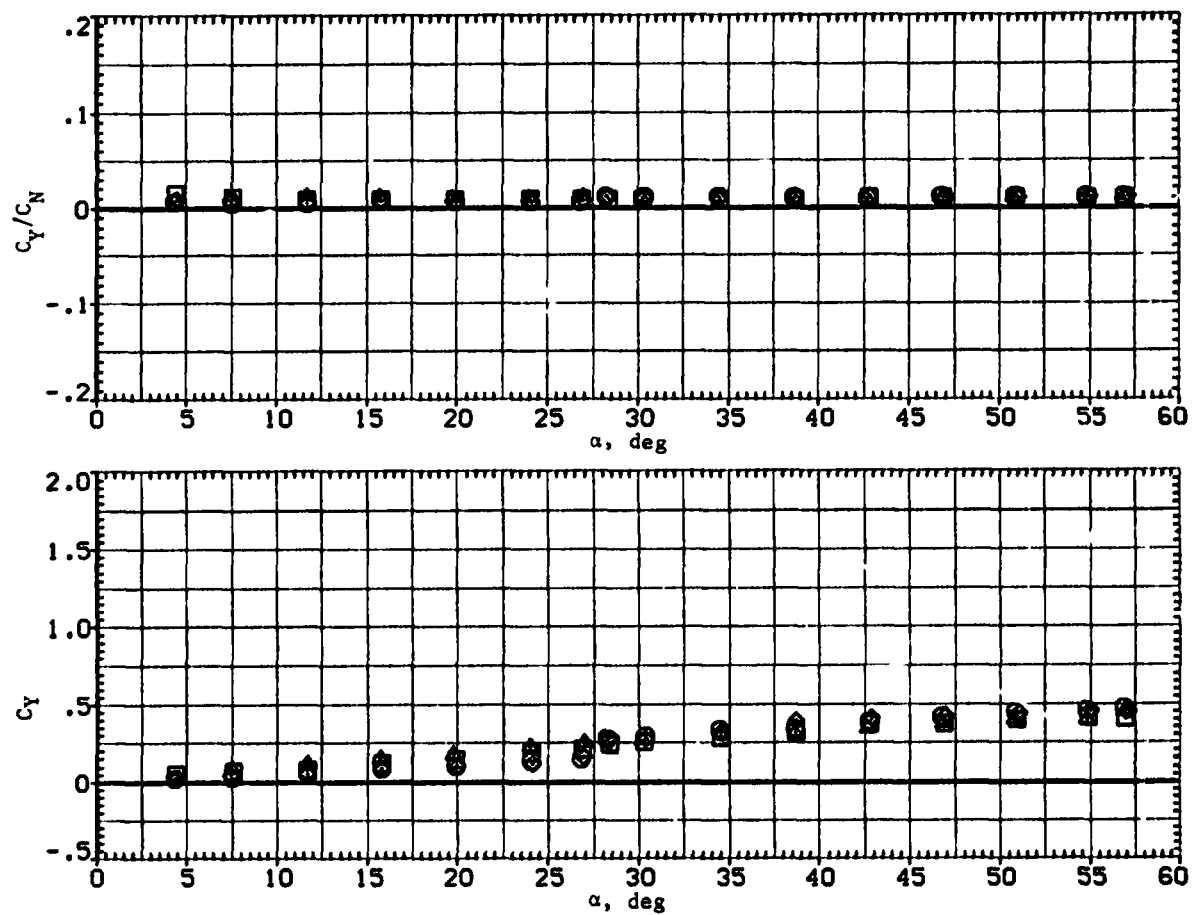


$$R \times 10^{-5}$$


(a)  $x_{acN}/d$  and  $C_N$  versus  $\alpha$ .

**Figure 27.— Effect of nose fineness ratio on wing-body characteristics;  $M = 2.0$ .**

SYMBOL	CONFIGURATION DESCRIPTION	$Re \times 10^{-5}$
	81 Y2 - NI C1 V2	3.800
	83 C1 V2	3.800
	83 C1 V2	3.800
	83 C1 V2	3.800



(b)  $C_Y/C_N$  and  $C_Y$  versus  $\alpha$ .

Figure 27.- Continued.



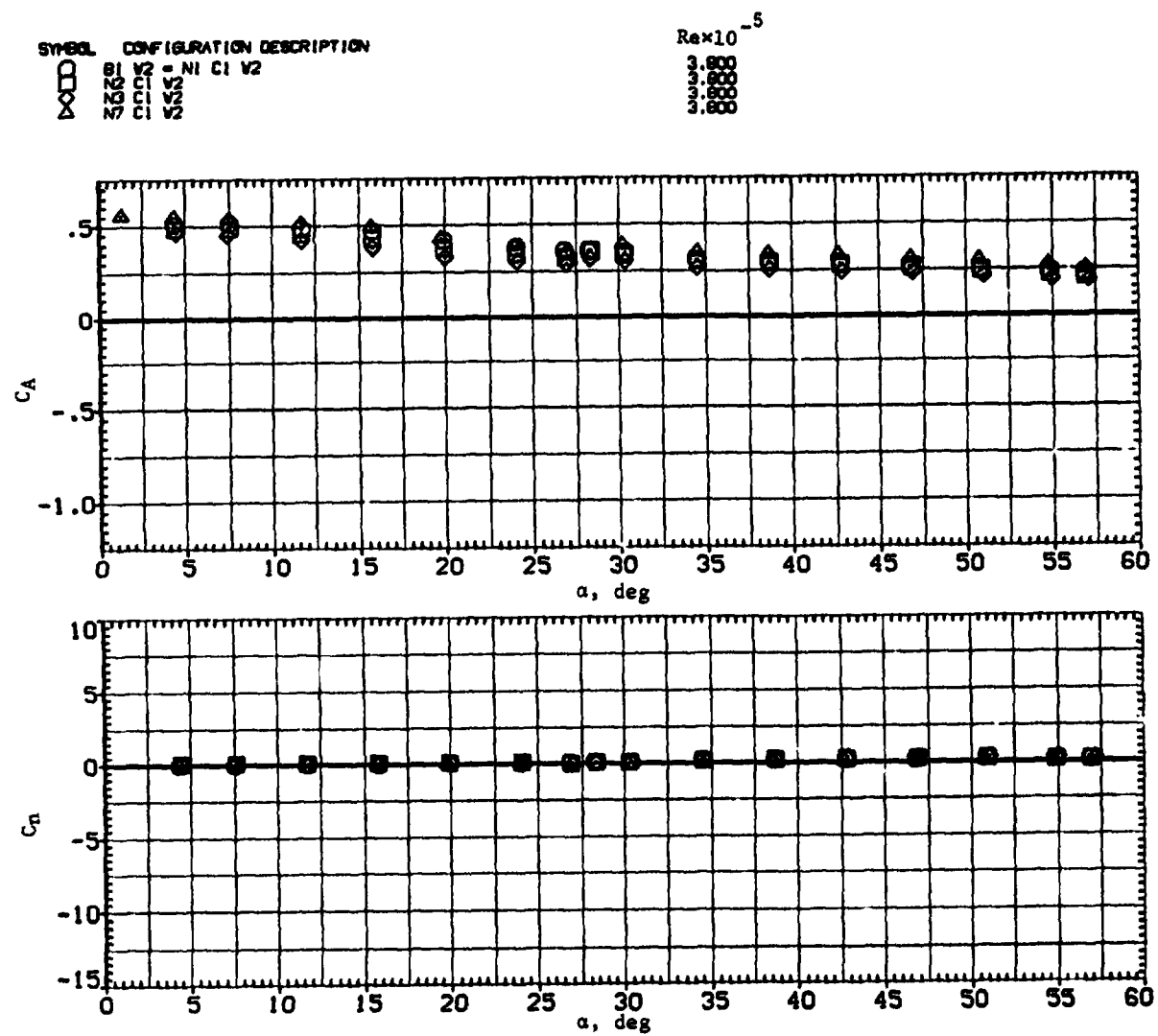
(c)  $C_A$  and  $C_N$  versus  $\alpha$ .

Figure 27.— Continued.

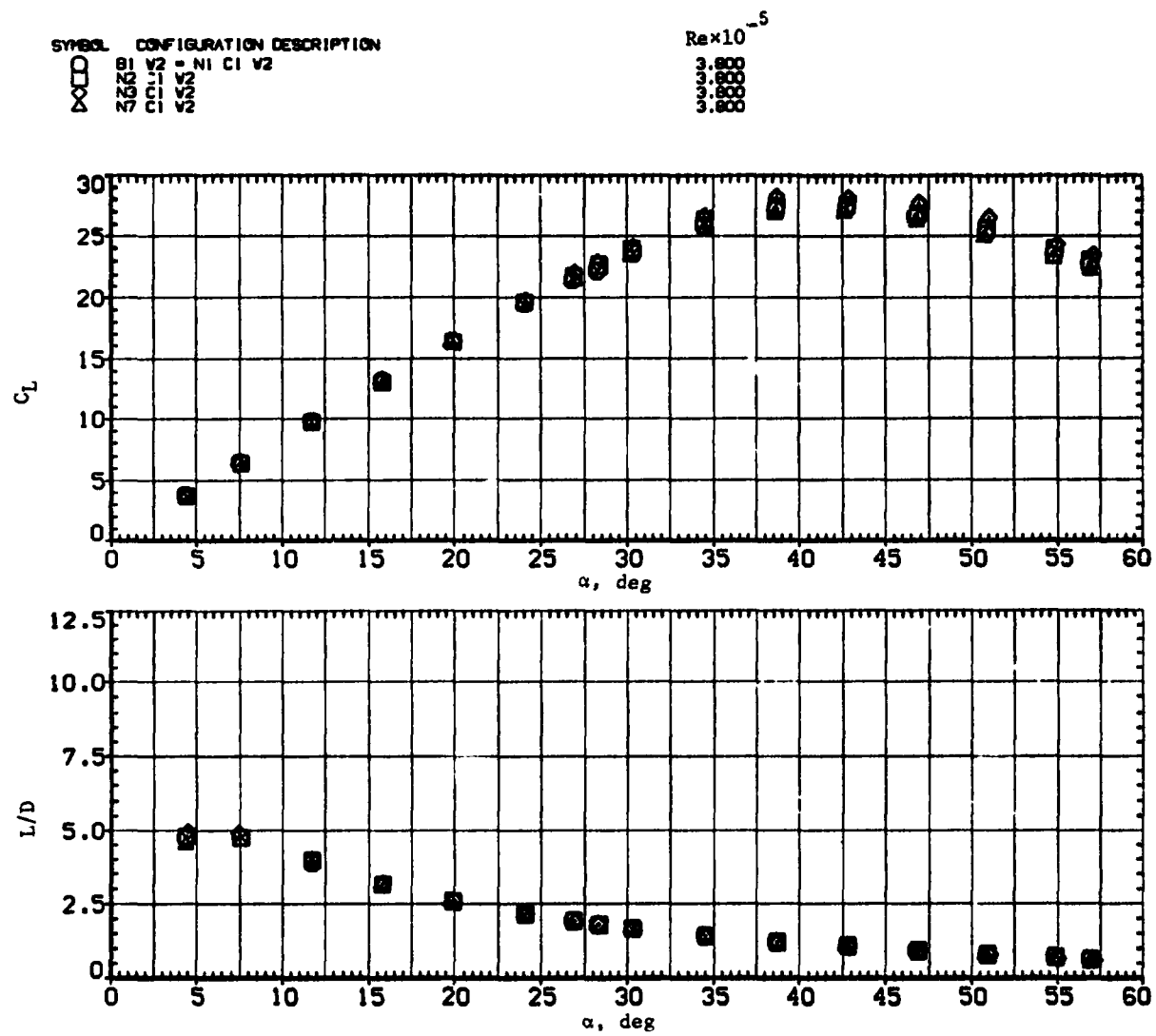
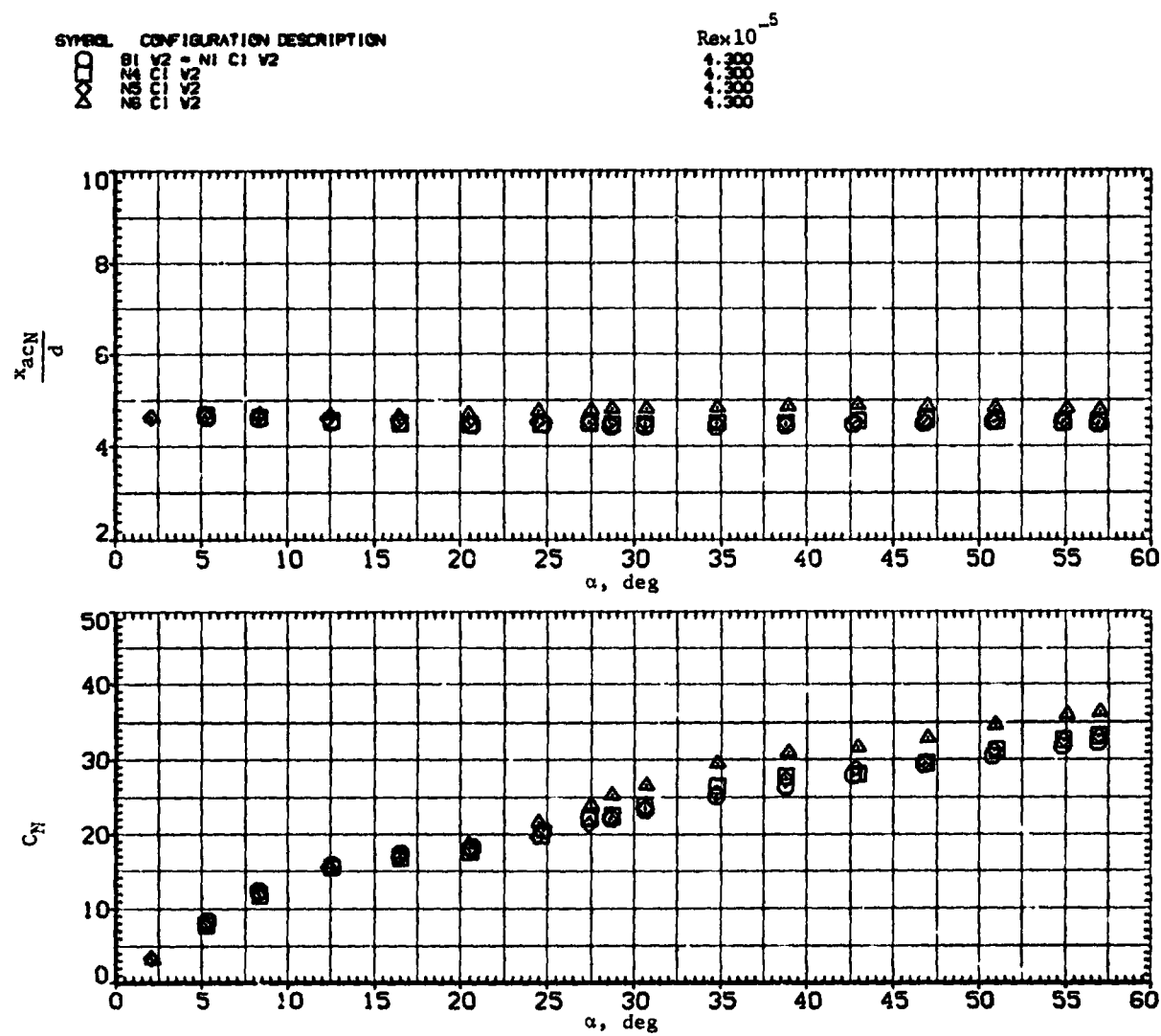
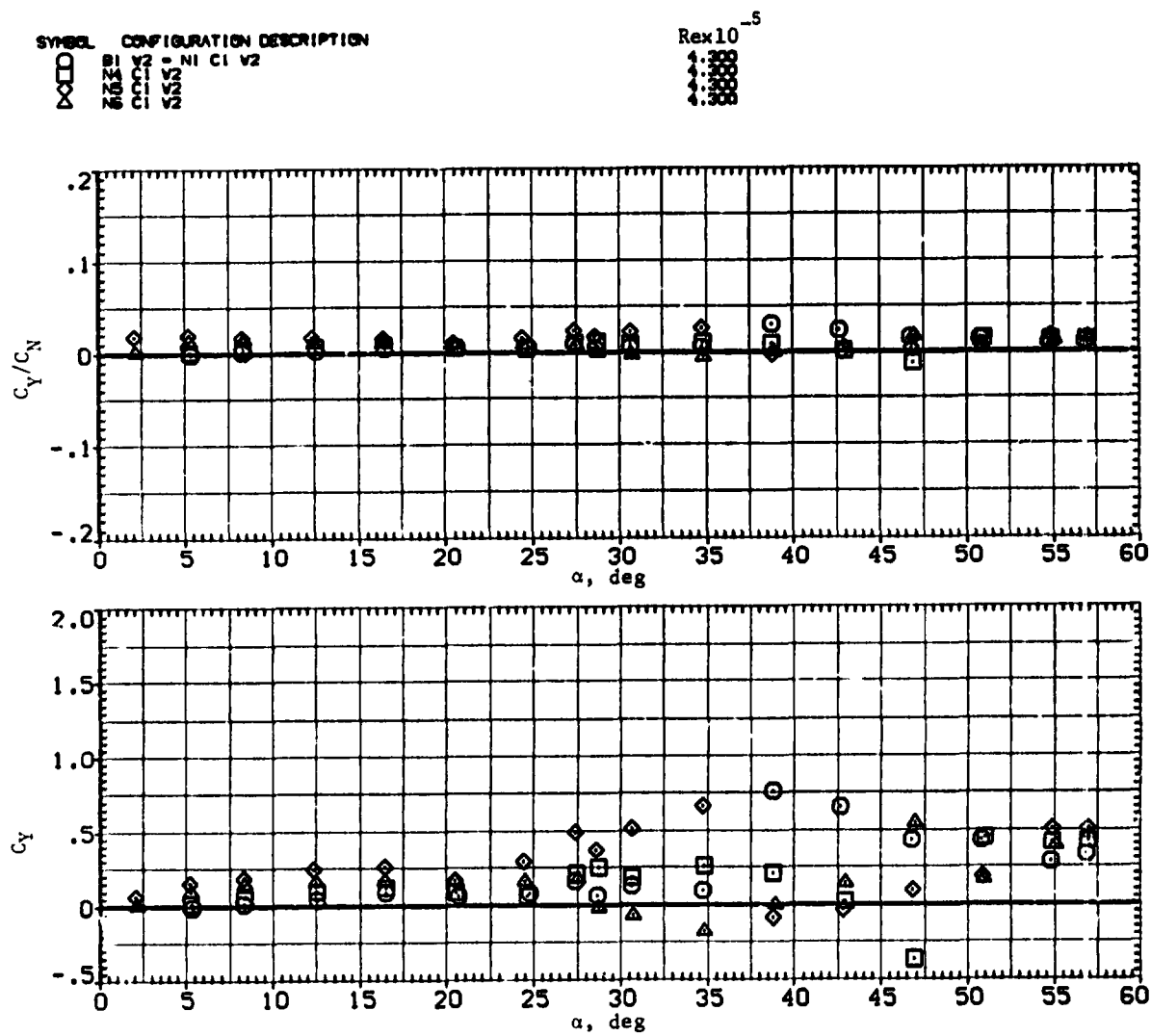


Figure 27.— Concluded.

(a)  $x_{acN}/d$  and  $C_N$  versus  $\alpha$ .Figure 28.— Effects of nose rounding and strakes on wing-body characteristics;  $M = 0.6$ .

REPRODUCIBILITY OF THE  
ORIGINAL PAGE IS POOR



(b)  $C_Y/C_N$  and  $C_Y$  versus  $\alpha$ .

Figure 28.— Continued.

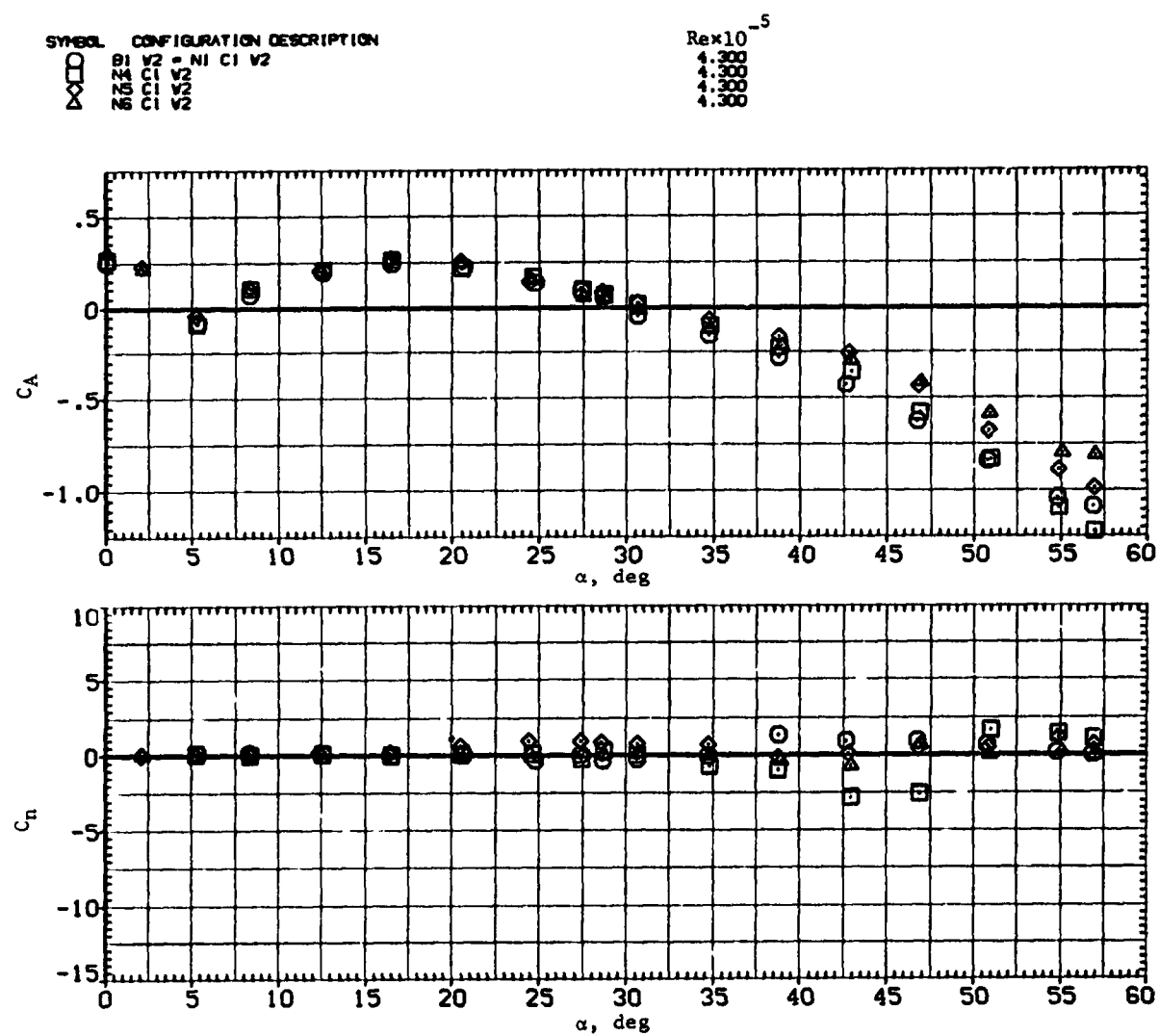
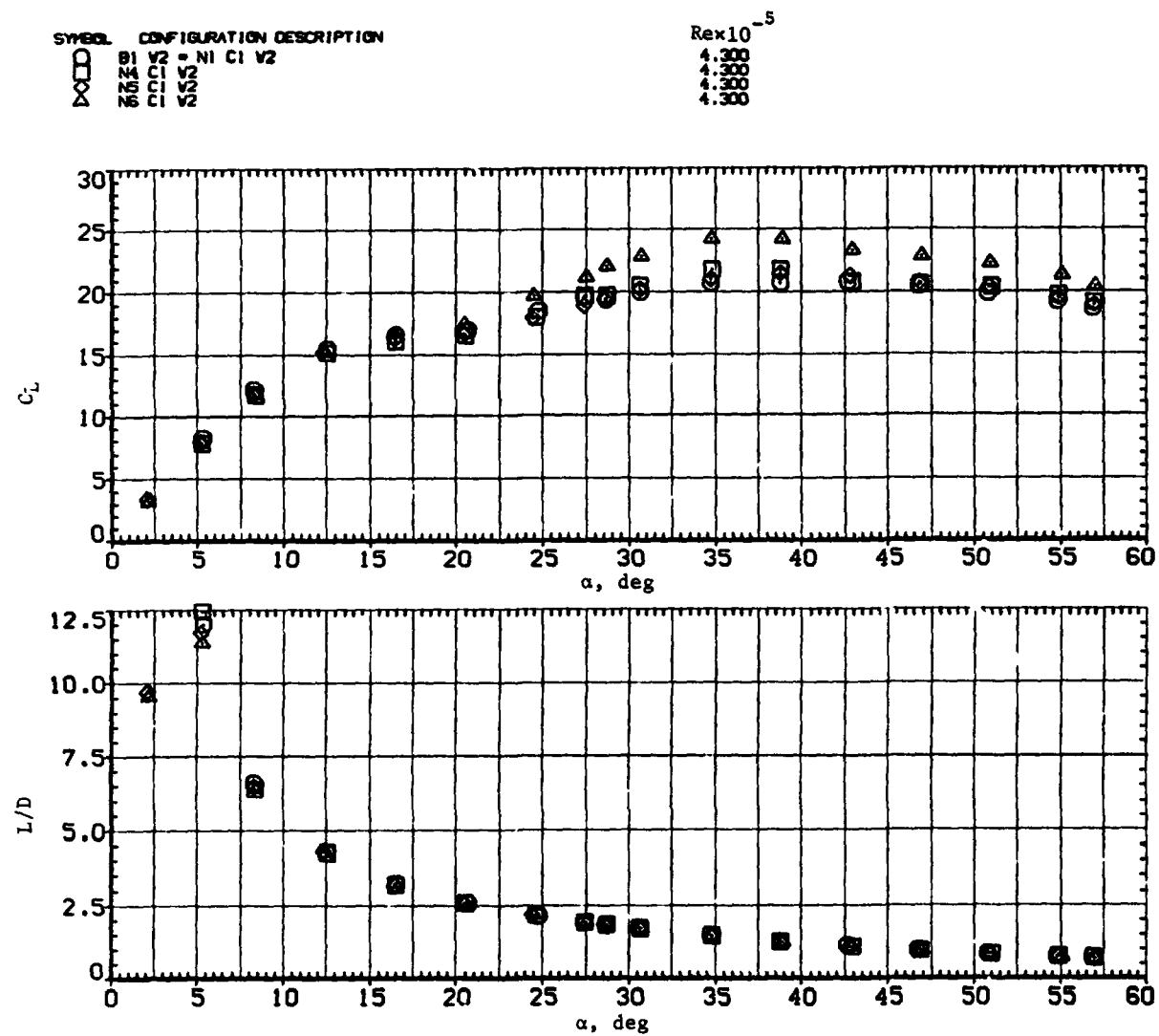
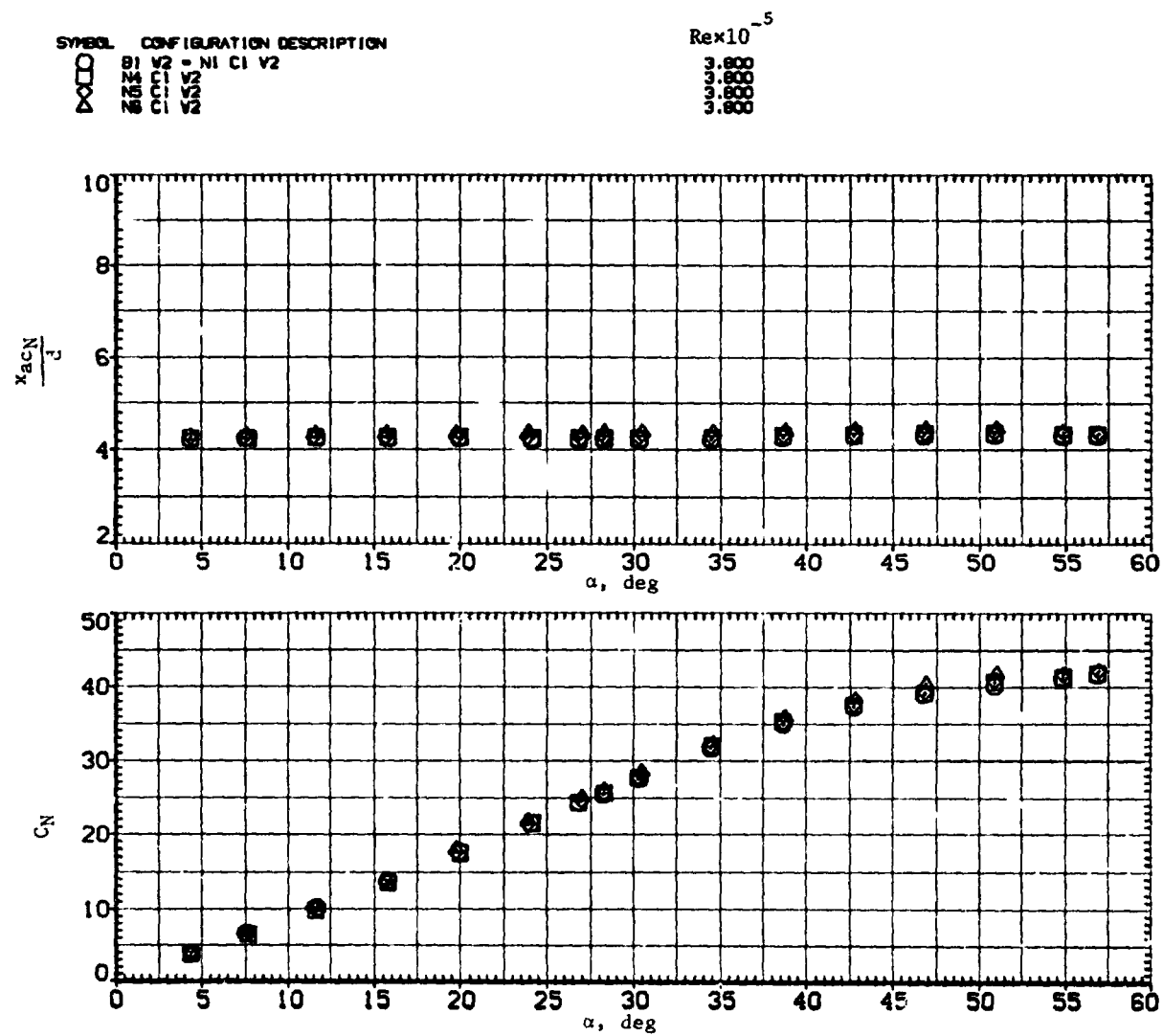
(c)  $C_A$  and  $C_N$  versus  $\alpha$ .

Figure 28.— Continued.

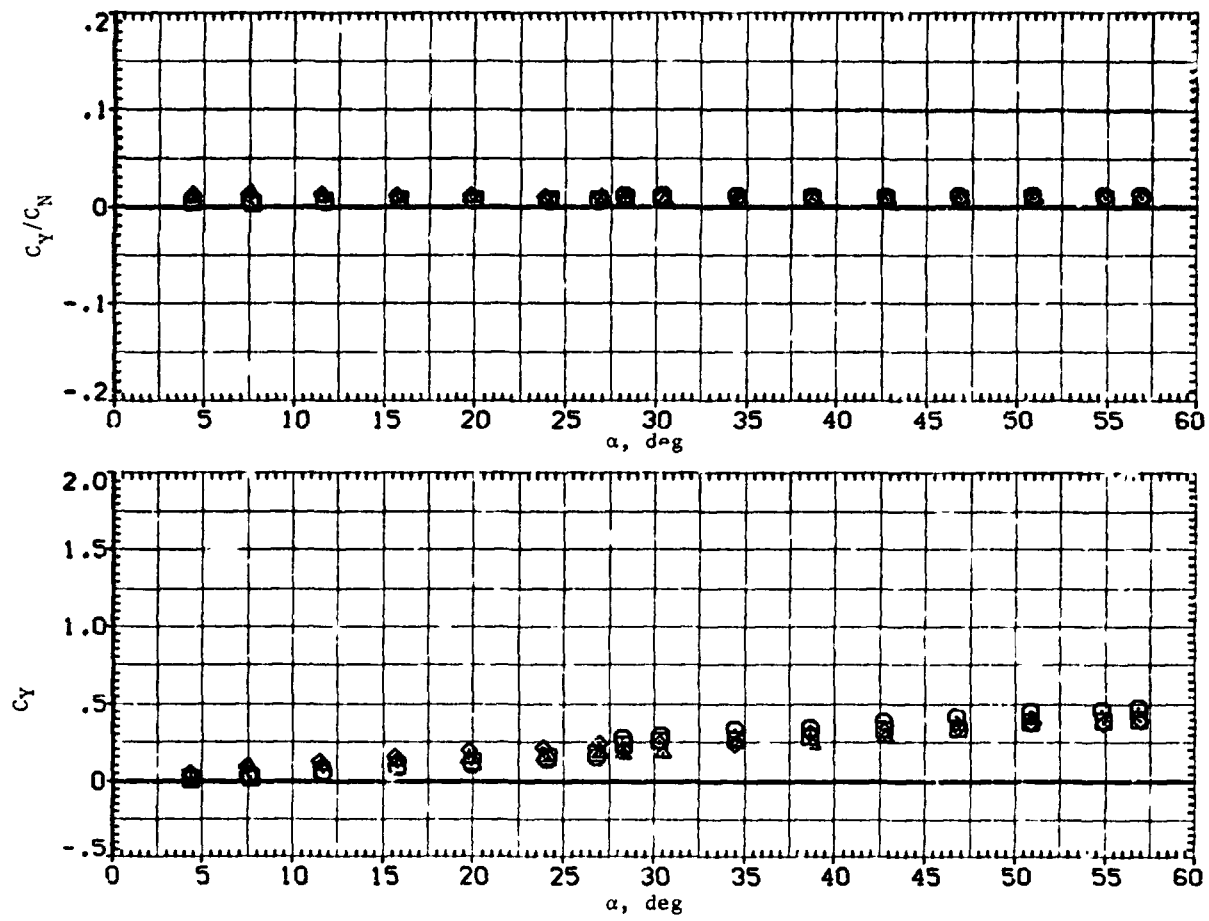


(d)  $C_L$  and  $L/D$  versus  $\alpha$ .

Figure 28.— Concluded.

(a)  $x_{acN}/d$  and  $C_N$  versus  $\alpha$ .Figure 29. -- Effects of nose rounding and strakes on wing-body characteristics;  $M = 2.0$ .

SYMBOL	CONFIGURATION DESCRIPTION	$Re \times 10^{-5}$
$\square$	B1 V2 = NI C1 V2	3.800
$\triangle$	B4 C1 V2	3.800
$\circ$	B5 C1 V2	3.800
$\times$	B6 C1 V2	3.800



(b)  $C_Y/C_N$  and  $C_Y$  versus  $\alpha$ .

Figure 29.-- Continued.



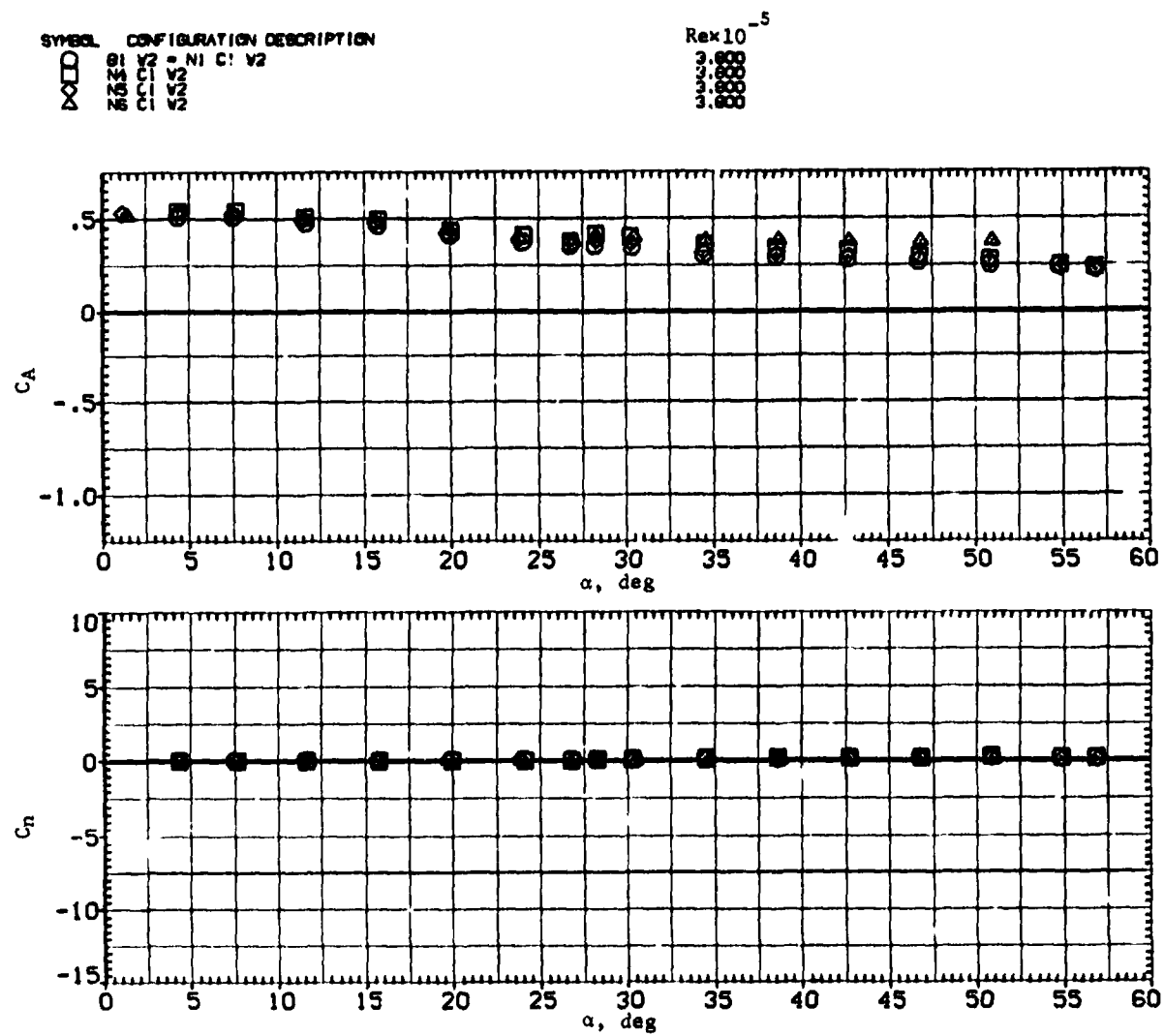
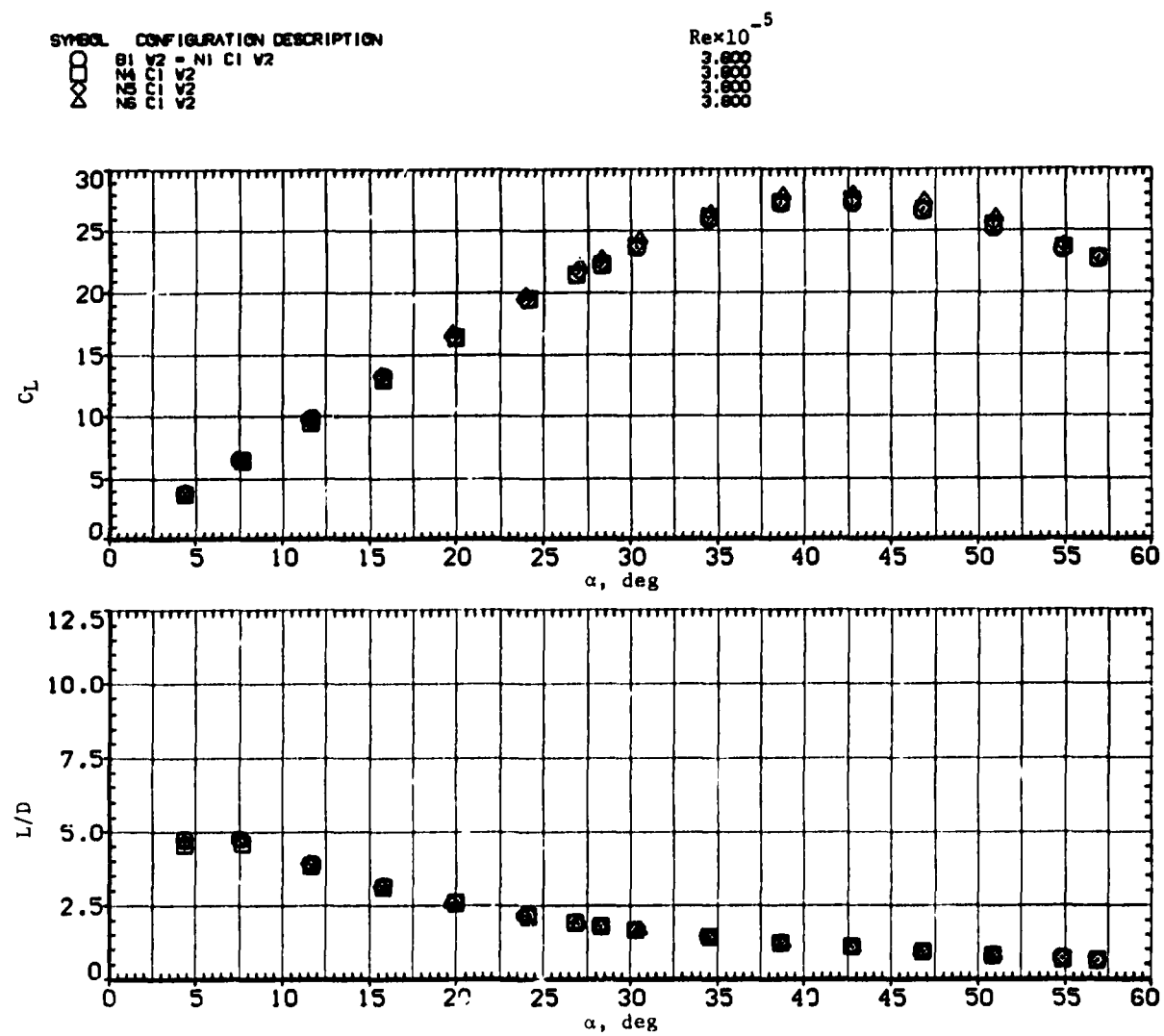
(c)  $C_A$  and  $C_n$  versus  $\alpha$ .

Figure 29.— Continued.



(d)  $C_L$  and  $L/D$  versus  $\alpha$ .

Figure 29. - Concluded.